First-Principles Investigation of Electron-Phonon Interactions in Novel Superconductors



Harry Fisher

Lincoln College

University of Oxford

A thesis submitted for the degree of

Doctor of Philosophy

Trinity 2014

First-Principles Investigation of Electron-Phonon Interactions in Novel Superconductors

Harry Fisher

Lincoln College

University of Oxford

A thesis submitted for the degree of

Doctor of Philosophy

Despite over 100 years of scientific research, a full understanding of superconductivity remains elusive. While it is known that the electron-phonon interaction is responsible for the formation of Cooper pairs in conventional superconductors, many superconductors exhibit behaviour suggestive of more exotic pairing mechanisms.

In this thesis, two novel superconducting materials are considered, monolayer transition metal dichalcogenide, MoS_2, and iron-based superconductor, $LaFeAsO_{1-x}F_x$. The former is ideal for the study of the electron-phonon interaction, as it not only has potential applications as an atomically thin transistor, but also displays a dome-shaped superconductive state as a function of electron doping. In the latter, the superconductive state emerges from a magnetic parent compound upon fluorine doping. Its high critical temperature is thought to be enhanced by magnetic fluctuation rather than being purely phonon-mediated.

By using novel first-principles techniques, the electron-phonon interaction in electron doped single-layer MoS_2 is investigated. The superconducting gap is calculated using the Migdal-Eliashberg theory, and by considering the electronic structure and lattice dynamics in this material, an explanation is provided for the experimentally observed doping-dependent critical temperature in this material.

The origin of the doping-induced transition from a magnetic phase to a nonmagnetic phase in $LaFeAsO_{1-x}F_x$ is determined. A new model to capture the effects of the flourine dopants is developed, which has implications for the electron-phonon interaction in this material.

Contents

Abstract **i**

Contents **iii**

1 Introduction **1**
1.1 Superconductivity 2
1.2 Novel Superconductors 8
1.2.1 MoS_2 8
1.2.2 $LaFeAsO_{1-x}F_x$ 12
1.3 Outline 14

2 First Principles Methods for Electronic Structure Calculations **17**
2.1 The Many-Body Schrödinger Equation 17
2.1.1 Born-Oppenheimer Approximation 19
2.1.2 Independent Electron Approximation 20
2.1.3 Hartree Approximation 21
2.2 Density Functional Theory 22
2.2.1 The Hohenberg-Kohn Theorems 22
2.2.2 The Kohn-Sham Equations 23
2.2.3 Exchange-Correlation Approximations 25
2.3 Solving the Kohn-Sham Equations 27
2.3.1 Plane Wave Basis Set 29
2.3.2 Pseudopotentials 30
2.4 Structural Optimisation 34
2.4.1 Hellmann-Feynman Theorem 35
2.5 Phonons 37
2.5.1 Lattice Dynamics 37
2.5.2 Density Functional Perturbation Theory 41

3 Electron-Phonon Interaction and Eliashberg Theory **45**
3.1 The Electron-Phonon Interaction 45
3.1.1 Beyond the Adiabatic Approximation 46
3.1.2 Electron Self-Energy 48

3.1.3 Phonon Self-Energy . . . 52
3.2 Electron-Phonon Coupling with Wannier Functions . . . 56
3.2.1 Maximally Localised Wannier Functions . . . 57
3.2.2 Wannier Interpolation of the Electron-Phonon Interaction . . . 58
3.3 Superconductivity . . . 60
3.3.1 BCS Theory . . . 60
3.3.2 Eliashberg Theory . . . 65
3.3.3 Practical Calculations . . . 69
3.3.4 Superconducting Gap on the Real Frequency Axis . . . 71

4 The Electron-Phonon Interaction in Doped Monolayer MoS_2 75
4.1 Introduction . . . 75
4.2 Bulk MoS_2 . . . 77
4.2.1 Electronic structure . . . 81
4.2.2 Phonons . . . 81
4.3 Monolayer MoS_2 . . . 83
4.3.1 Electronic Structure . . . 84
4.3.2 Phonons . . . 87
4.4 Rigid band electron doping in MoS_2 . . . 88
4.4.1 Calculation details . . . 89
4.4.2 Total electron-phonon coupling . . . 96
4.5 Jellium model electron doping in MoS_2 . . . 103
4.5.1 Electronic structure . . . 104
4.5.2 Phonons . . . 108
4.5.3 Total electron-phonon coupling . . . 113
4.6 Conclusion . . . 118

5 Superconductivity in Electron Doped Monolayer MoS2 121
5.1 Introduction . . . 121
5.2 Heavily Electron Doped MoS_2 . . . 123
5.3 Calculation Details . . . 127
5.4 Isotropic Eliashberg Equations . . . 130
5.5 Anisotropic Eliashberg Equations . . . 134
5.6 Coulomb Interaction . . . 141
5.7 Comparison to Experiment . . . 141

6 The Magnetic Phase Diagram of $LaFeAsO_{1-x}F_x$ Superconductors 147
6.1 Introduction . . . 147
6.2 Computational Methods . . . 149
6.3 LaFeAsO . . . 150
6.4 $LaFeAsO_{1-x}F_x$ . . . 155

6.5 Fe-As Layer Separation 158
6.6 Minimal Model 160
6.7 Electronic Structure 163
6.8 Phonon Density of States 164
6.9 Conclusions 166

7 Conclusion **169**
7.1 Summary 169
7.2 Future Work 174

Bibliography **177**

Acknowledgements **I**

Chapter 1

Introduction

This thesis is concerned with the study of novel superconducting materials. In particular, the electron-phonon interaction, which is known to be responsible for the pairing mechanism in conventional superconductors, will be investigated in monolayer MoS_2. It is important to understand the phonon scattering mechanisms in this material, as it has potential application in devices for nanoelectronics. The effect of electron doping on the electron-phonon interaction in single-layer MoS_2 is also of interest. By analysing how the electronic structure and lattice dynamics evolve with electron doping, an explanation for the onset of superconductivity in this material is given. The Migdal-Eliashberg theory is used to calculate the critical transition temperature in this superconductor from first-principles. By studying the effect of electron doping on the superconducting gap of monolayer MoS_2, possible explanations of the dome-shaped superconductive region in the carrier concentration vs critical temperature phase diagram are provided.

Another novel superconductor of interest is the iron-based superconductor, $LaFeAsO_{1-x}F_x$. This class of superconductors experience a magnetic-nonmagnetic phase transition upon electron doping leading to the superconductive state. The

atomistic origin of this transition is an outstanding issue. By explicitly inclusion of F atoms in our calculations, the role of the dopant in this transition is clarified.

The purpose of this introductory chapter is to provide some background and motivation for the work undertaken in this thesis. An outline of the structure of the thesis is also provided.

1.1 Superconductivity

The macroscopic quantum phenomenon of superconductivity was discovered in 1911, three years after Kamerlingh Onnes succeeded in liquefying helium [1]. This rendered temperatures as low as 1 K accessible to experimental methods. Studies of the relationship between temperature and electrical resistivity of mercury (chosen because it could be prepared in very high purity) revealed that, as the temperature approaches absolute zero, the resistance completely disappeared below 4.1 K [2]. Such a drop in electrical resistivity is a property of all superconductors, and the temperature at which this occurs is known as the critical temperature T_c (Fig 1.1). At this temperature, a phase transition occurs between the normal and superconducting states.

Superconductors also have unusual magnetic properties. In a weak magnetic field, a superconducting material will act as a perfect diamagnet. This is called the Messiner effect. The maximum strength magnetic field in which the superconducting order is maintained is known as the critical field H_c. The critical field is a function of temperature such that $H_c(T_c) = 0$.

Only two years after the discovery of superconductivity in Hg, lead was found to superconduct at 7.2 K [4]. It was not until 1930 that a material was discovered with a higher transition temperature, when niobium was shown to superconduct

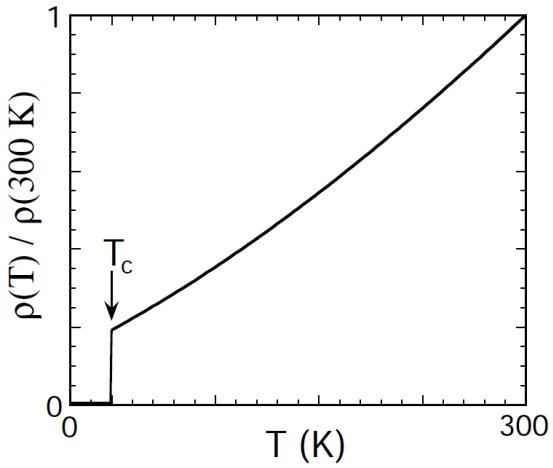


Figure 1.1: The temperature dependence of electrical resistivity of a superconductor. T_c is the critical temperature where the transition to a superconducting state takes place. From [3].

up to 9.2 K [3]. This remains the highest T_c for an elemental metal at ambient pressure. This early search for new superconducting materials demonstrated that superconductivity is not particularly rare, and by 1951, research into superconducting materials had yielded over 20 superconducting elements. Today, through the manipulation of pressure and measurements at yet lower temperature, we know of over 50 elements which can be made superconducting [5]. As the search for new superconducting materials spread to binary intermetallic compounds in the 1930's, there was increasing interest in a unifying explanation as to which materials would have the highest T_c's.

Finally, almost 50 years after the discovery of superconductivity, in 1957, a microscopic theory was proposed by Bardeen, Cooper, and Shrieffer (BCS) [6]. They showed that, given some attractive interaction between two electrons, there is an instability of the Fermi liquid state leading to a new ground state in which correlated pairs of electrons form. These are referred to as Cooper pairs [7]. The work of Fröhlich had previously demonstrated that an effective electron-electron

attraction could be obtained by exchange of virtual phonons [8]. In many superconductors it is precisely this electron-phonon interaction that is responsible for the pairing mechanism.

Fig. 1.2 charts the history of attempts to raise the critical temperature in new superconducting materials. It can be seen that the advent of a microscopic theory in 1957 did not immediately transfer into advances in the maximum T_c. Rather, the BCS expression relating the T_c to the Debye frequency, ω_D, the electronic density of states at the Fermi level, N_F, and the effective pairing potential, V, given as $k_B T_c = 1.14\hbar\omega_D \exp(-1/N_F V)$, moved the focus onto the transition metal materials, because they generally have a larger N_F than simple metals. A maximum T_c of 23 K was found in the transition metal intermetallic Nb_3Ge in 1973 [10]. At this point, superconductivity was considered one of the best-understood problems in many-body physics, and it seemed unlikely that much higher critical temperatures would be discovered [11]. Various different theoretical upper limits to the maximum T_c were proposed, as it was predicted that as the electron-phonon interaction became too strong, the lattice would distort, in turn reducing the coupling [12,13]. The energy scale of the phonon frequencies ultimately limits the T_c in a BCS superconductor, and from this McMillan estimated an upper limit for T_C of 28 K [13].

Interest in superconductivity was renewed in 1979 when a new class of materials, close to magnetic instability, was discovered to superconduct [14]. These "heavy-fermion" superconductors of $CeCu_2Si_2$, UBe_{13}, UPt_3 have f-shell electrons and display other interesting properties, such as very large low-temperature magnetic susceptibility, and unusual temperature dependence of their specific heats below 10 K [15]. Most importantly, these strongly correlated f-shell electrons determine the properties of the quasiparticles at the Fermi level and lead to very large effective masses. Such quasiparticles do not fit with the BCS theory of superconductivity, as

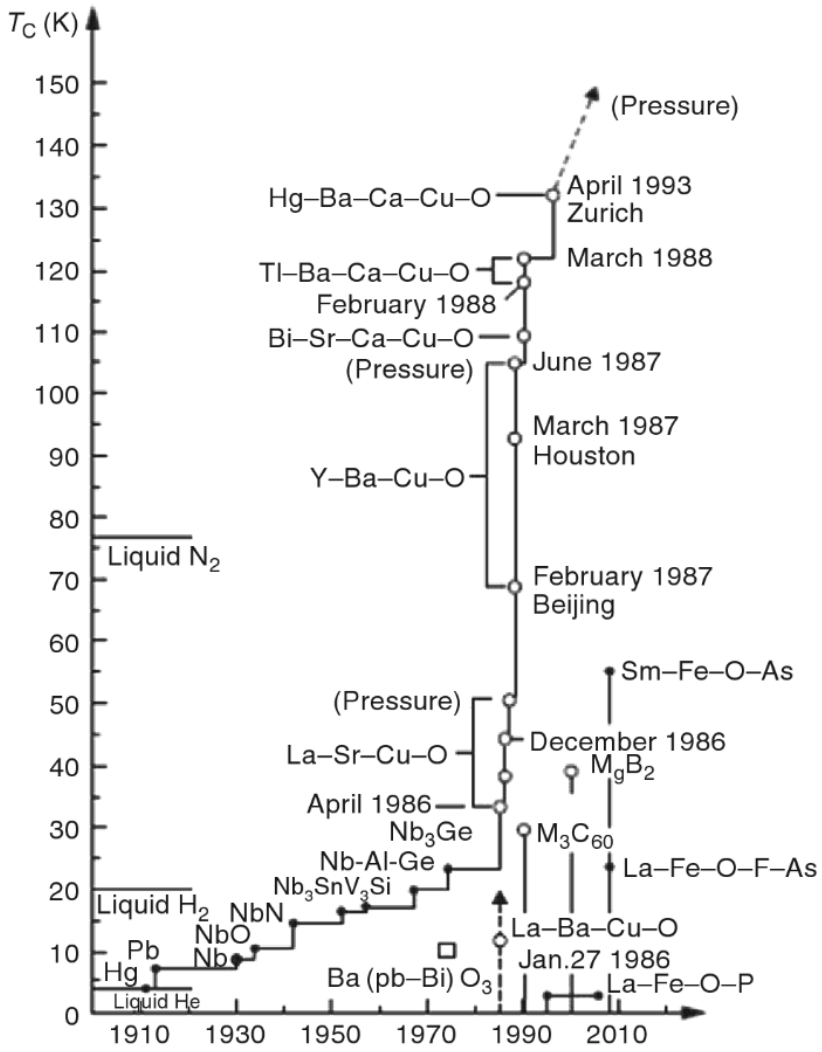


Figure 1.2: The evolution of the superconducting critical temperature as a function of time. From [9].

the strong Coulomb repulsion prevents the formation of ordinary s-wave Cooper pairs with opposite momentum and opposite spin [11]. An anisotropic channel such as p-wave spin triplets or a d-wave spin singlet state is needed to avoid a large overlap in the wavefunctions of the paired particles. Various attempts had been made in the early 1960's to generalise superconductivity to such anisotropic pairings, and these also helped explain the p-wave pairs in superfluid ^{3}He [16–20]. Thus, any materials in which the type of pairing deviates from the isotropic s-wave paring of BCS superconductors is termed an *unconventional* superconductor. In the "heavy-fermion" systems, the first experimental evidence for unconventional superconductivity was discovered. This was the T^3 law in the specific heat of UBe_{13}. A feature of nonzero angular momentum state pairings is the possibility of nodes in the superconducting gap where the order parameter vanishes. This in turn explains the power law behaviour seen in certain physical quantities at low temperature, such as ultrasonic attenuation, NMR relaxation rates, and specific heat. In conventional superconductors where the Fermi surface is fully gapped there is an exponential dependence at low temperature for these quantities.

The existence of the heavy-fermion superconductors questioned the idea that the electron-phonon interaction is the only possible mechanism to obtain an attractive potential needed for superconductivity. Alternative mechanisms may favour anisotropic pairings, and pairings via plasmons, spinons, exictons, and vibrons have all been proposed [21–24].

The most famous class of unconventional superconductor are the copper oxides. The discovery of superconductivity in Ba-doped La_2CuO_4 at almost 40 K caused a massive increase in the research efforts for these materials [25]. This soon led to the first high-temperature superconductor, defined as having a T_c greater than the boiling point of liquid nitrogen at 78 K, in $YBa_2Cu_3O_7$ with a $T_c = 93$ K [26]. A

maximum T_c of 134 K was found in a Hg-based cuprate which, under pressure can sustain the superconductivity state beyond 150 K [27, 28].

All cuprate superconductors, whether tetragonal or orthorhombic, contain square or rectangular CuO_2 planes. Due to the relatively high ratio of the c-axis to a-axis lattice constants, the cuprates have a flattened Brillouin zone and share the basic symmetry properties of the unit cell of a square/rectangle lattice. Band structure calculations show that the energy bands are predominantly derived from the copper oxide planes and display no significant dispersion in the direction of the c-axis [29–33]. It has been shown that the superconductivity originates from these two-dimensional CuO_2 layers, and so the pairing symmetry should reflect the symmetry of these square/rectangular lattices [34]. The pairing is thought to be predominately d-wave; however, the exact mechanism for superconductivity is as yet unknown [35]. What is known is that the superconductivity is primarily due to a non-phonon mechanism [36].

In more recent years, the discoveries of phonon-mediated superconductors with critical temperatures near 40 K, such as MgB_2 and K_3C_{60}, demonstrate that McMillian's upper limit on T_c due to structural instabilities from a very strong electron-phonon interaction is not valid. In fact, it may be possible for phonon-mediated superconductors to obtain even higher T_c's, as has been predicted by first-principles calculations of doped graphane [37].

Even more recently a new class of unconventional superconductors with quasi-2D properties similar to the cuprates have been discovered in the iron based superconductors, also known as the iron pnictides [38]. Systems containing FeP, FeSe or FeAs square-lattice layers with a variety of different spacers become superconducting when either electron- or hole-doped from the magnetic parent compound [39]. Although the highest T_c is this class is much lower than for the cuprates, at just

55 K, this still represents the highest T_c of any non-cuprate material. Like the cuprates, it is assumed that the magnetism plays some part in the origin of the observed superconductivity, but at this stage the exact mechanism is unknown. The two electrons in a singlet Cooper pair have the same charge but opposite spin, and an *s*-wave symmetry with a sign change of the order parameter has been both proposed theoretically and observed experimentally [40, 41]. The situation in the iron pnictides is yet further complicated by the fact that some display nodes in the superconducting gap, while others are fully gapped [42].

1.2 Novel Superconductors

Another class of novel superconductors include the monolayers of transition metal dichalcogenides, such as MoS_2. These compounds are currently being studied for applications in nanoelectronics, and offer a unique opportunity to realise gate-induced superconductivity. Monolayer MoS_2 is an ideal material to study, as it has potential applications as an atomically thin transistor; furthermore, recently, superconductivity has been observed up to ~ 10 K [43, 44].

The other novel superconductor investigated in this thesis is $LaFeAsO_{1-x}F_x$, the first iron-based superconductor to be discovered. As it is known that it is an unconventional superconductor, which cannot be explained by a primarily phonon-mediated pairing interaction, only the effect of doping on the structural and electronic properties will be investigated [45].

1.2.1 MoS_2

The discovery of graphene has sparked interest in two dimensional materials which exist in bulk form as stacks of strongly bonded layers with weak interlayer inter-

actions [46]. In particular, MoS_2, which in its bulk form displays a wide variety of electronic, optical, and mechanical properties which have been extensively studied, is of great scientific interest in its two-dimensional form, due to its complementary properties in comparison to graphene [47, 48]. Monolayers can be prepared via a number of different methods. Using the same techniques developed for graphene, thin flakes can be peeled from the bulk crystals by micromechanical cleavage using Scotch tape [43, 46, 49–51]. These thin flakes can then be applied to substrates and optically identified by light interference [52, 53]. The major disadvantages of this method are the lack of scalability and systematic control of the size and thickness of the thin flakes [54]. A different method of obtaining atomically thin layers of MoS_2 is liquid phase exfoliation [55, 56]. One advantage of this method is the ease with which more complicated composite and hybrid materials can be synthesised. A further alternative to the top-down methods discussed so far is to grow thin films of MoS_2 on insulating substrates via chemical vapour deposition [57–59]. Although still at an early stage of development, it is hoped that large-area, uniform sheets with a controllable number of layers can be obtained via this method.

One particularly interesting aspect of the semiconducting transition metal dichalcogenides is that certain properties, such as the band gap, display a layer-dependence. For example it has been both theoretically predicted and experimentally observed that there is a transition from an indirect band gap in the bulk to a direct gap in the single-layer material [60–62]. While bulk MoS_2 has an indirect gap of 1.2 eV, there is an increase to 1.8 eV in the monolayer, as observed in changes in photoconductivity, absorption spectra, and photoemission [49, 51, 63]. Another layer-dependent property of MoS_2 is the Raman active phonon mode frequencies. These Raman peaks correspond to in-plane E^1_{2g} and E_{1u} modes and out-of-plane A_{1g} modes. As the layer thickness increases, the A_{1g} mode near 406 cm^{-1} increases in frequency,

while the E^1_{2g} mode near 382 cm^{-1} decreases in frequency [64]. This allows for the layer thickness to be identified by the Raman peak shift.

As a semiconductor, one of the most important applications of MoS_2 is as a transistor in digital electronics. Current processors use silicon-based metal-oxide-semiconductor filed-effect transistors (MOSFETs) with feature lengths of 22 nm [65]. As progress in this field is driven by scaling transistors to even smaller dimensions, it is clear that soon they will reach the limit due to quantum effects and difficulties with heat dissipation [65]. Thus, a new device concept or material is needed. Graphene has been proposed due to its high carrier mobility, low-dimensionality, and because an external gate voltage can modulate its current flow [66]. However, the lack of a band gap means it cannot achieve the on-off current ratio needed for transistors [67, 68]. A top-gated transistor based on MoS_2 has already been fabricated [43]. It has an excellent on/off current ratio, which is important for effective switching, and a room temperature mobility of over 200 $cm^{-2}V^{-1}s^{-1}$. This mobility will be affected by phonon scattering, Coulomb scattering from charged impurities and roughness scattering. It is therefore important to understand the electron-phonon coupling in this material.

Interestingly, thin flakes of MoS_2 have been shown to superconduct with a maximum critical temperature of 10.5 K at high carrier concentrations [44, 69]. The electrostatic carrier doping was achieved using ionic liquids to form an electrical double layer of high capacitance [70, 71]. This method has previously been used to examine the superconducting dome as a function of doping in cuprate superconductors [72, 73]. It was discovered that, in a similar manner to some unconventional superconductors, MoS_2 displays a doping-dependent critical temperature, which reaches a maximum as a function of doping, and then decreases with increasing doping, as seen in Fig. 1.3. At this point very little is known of this superconducting

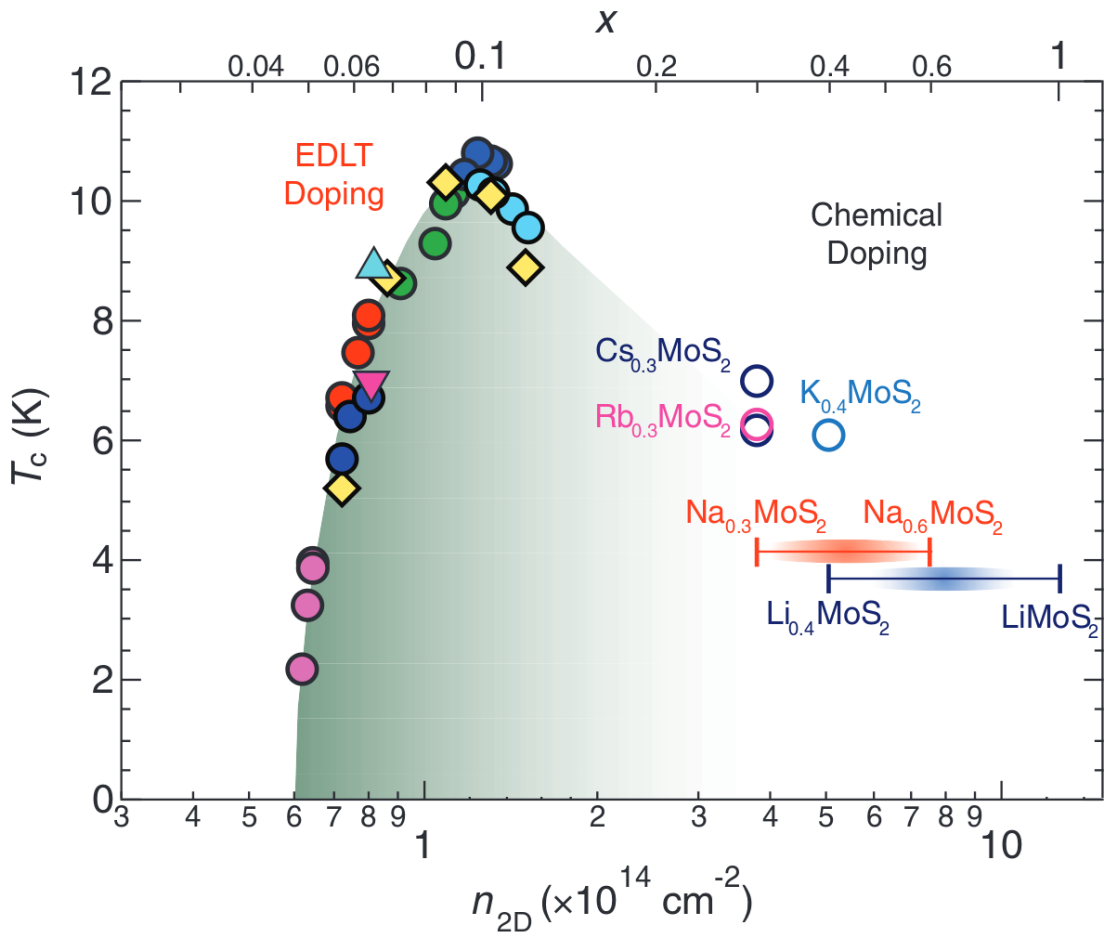


Figure 1.3: A unified phase diagram of both chemically and electrostatically electron doped MoS_2. The different symbols represent different samples. From [44].

state and so this is interesting to investigate.

1.2.2 $LaFeAsO_{1-x}F_x$

In early 2008, $LaFeAsO_{1-x}F_x$, the first iron-based superconductor, was discovered, with a relatively high critical temperature of 26 K [38]. This T_c can be increased to 43 K under a high pressure of ∼4 GPa [74]. The crystal structure of this material is of the same type as ZrCuSiAs, with a space group of P4/nmm. LaO and FeAs layers are stacked along the *c*-axis. The parent compound, LaFeAsO, is non-superconducting and shows an antiferromagnetic transition around 150 K [75]. Like all iron-based superconductors, superconductivity only emerges when the magnetic order in the parent compound is destroyed [76]. This can be via pressure or doping. When approximately 4% oxygen is replaced by fluorine, a superconducting state develops [77]. Although T_c reaches a maximum in $LaFeAsO_{1-x}F_x$ when $x = 0.11$, from the onset of the superconductive state until $x = 0.14$ T_c is nearly unchanged [78]. It has been noted that T_c is maximised when the $FeAs_4$ lattice forms a regular tetrahedron [77].

Density functional theory (DFT) calculations of the underlying electronic structure have been performed. These show that the Fermi surface is comprised of five bands mainly originating from the Fe 3*d* orbitals [79, 80]. Pristine LaFeAsO is a semimetal with both electron and hole bands. It can be seen in Fig. 1.4 that there are two high-velocity electron cylinders around the M point, two lower-velocity hole cylinders around the Γ point, and a heavy three-dimensional hole pocket at the Z point which intersects the other hole bands. This 3D pocket is derived from Fe d_z states which hybridise with La and As p states. Angle resolved photoemission spectroscopy (ARPES) experiments have shown that these theoretical band calculations produce Fermi surfaces which agree well in both the location and overall

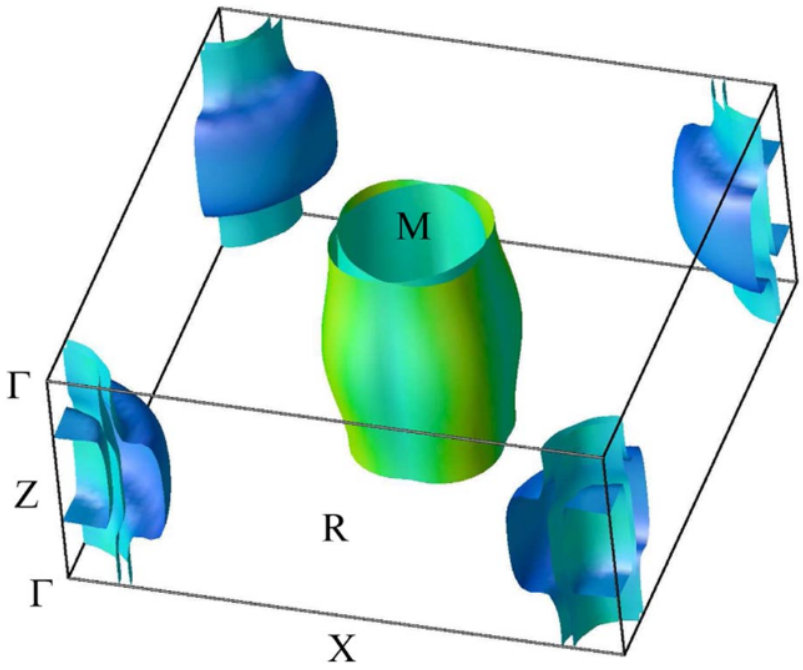


Figure 1.4: DFT calculated Fermi surface of LaFeAsO. The high velocity bands are shaded in a lighter colour. From [79].

shape of the Fermi sheets, with the exception of the size of the electron cylinder at the zone centre [81]. However, it is thought that this agreement is due to surface effects in the ARPES measurements. In fact, the DFT calculations which suggest similar-sized Fermi sheets at both the M and Γ points are backed up by quantum oscillation measurements [82].

The cylinders at M and Γ are nearly nested, and this can lead to enhanced spin fluctuations in this nesting vector [83]. If these spin fluctuations are strong enough, they can cause stripe-type spin-density-wave ordering, which is the ordering predicted as the magnetic ground state for the undoped parent compound [84]. The main effect of the doping is to reduce the degree of nesting of the Fermi surfaces. This explains why the phase diagram is roughly symmetric with respect to both hole doping and electron doping. Inelastic neutron-scattering spectra show a peak that corresponds to magnetic excitations at a particular wavevector [85]. This

wavevector is roughly the separation of the two sets of Fermi surfaces at M and Γ. This has lead to the theory that in iron-based superconductors the superconductivity is unconventional and mediated by antiferromagnetic spin fluctuations. The most likely pairing state is an extended s-wave pairing with a sign reversal of the order parameter between different Fermi sheets [86]. This is termed $s_{\pm}$-wave pairing. Nuclear magnetic resonance spectroscopy data shows that the Cooper pairs in iron-based superconductors are spin singlet; that is, they have the same charge but opposite spin. This further supports the $s_{\pm}$-wave pairing theory, although other pairings such as $d_{x^2-y^2}$-wave cannot be ruled out [87].

A large isotope effect is found in the FeAs layers but not in the LaO layers [88]. This suggests that it is the FeAs layers responsible for the superconductivity, and also that there is a possibility of an unconventional electron-phonon pairing mechanism. Theoretical studies of the electron-phonon interaction in $LaFeAsO_{1-x}F_x$ have shown that conventional electron-lattice pairing is not sufficient to explain the relatively high T_c's [45]. For this reason, in this thesis, the doping-induced transition from stripe-antiferromagnetic to a nonmagnetic phase will be studied. It is known that there is a dependence of the Fe magnetic moment on the structure, and I wanted to clarify the origin of the observed phase change in fluorine doped LaFeAsO [89].

1.3 Outline

This thesis is organised as follows. In Chapter 2, the background theory for the first-principles calculations undertaken in this thesis is discussed. Particular attention is paid to standard density functional theory techniques for the calculation of electronic states and phonon frequencies needed to understand the electron-phonon

interaction. In Chapter 3, the methods for calculating the electron-phonon interactions are discussed. The novel techniques used to calculate properties related to the electron-phonon coupling are described, including superconductivity within the Migdal-Eliashberg theory. In Chapter 4, the electronic structure and lattice dynamics of both bulk and monolayer MoS_2 are presented. The effect of electron doping on the electron-phonon interaction in the monolayer are investigated. The goal of Chapter 5 is to calculate from first-principles the T_c of single-layer MoS_2, and understand the superconductivity in this material. The effects of electron doping and lattice parameters are also studied. The role of the fluorine dopant in the magnetic phase diagram of $LaFeAsO_{1-x}F_x$ superconductors is investigated in Chapter 6. Finally, Chapter 7 provides a summary of the thesis and suggestions for further work that could be carried out in the future.

Chapter 2

First Principles Methods for Calculating the Electronic Structure of Materials

The purpose of this chapter is to outline the underlying theory needed to describe the electronic structure of materials from first principles. All calculations undertaken in this thesis are based on Density Functional Theory (DFT) and so the origins of this theory are discussed. The various approximation which are necessary for a practical calculation are explained. A plane wave, pseudopotential approach with periodic boundary conditions has been applied in this work and so these aspects are described here.

2.1 The Many-Body Schrödinger Equation

At the atomic level materials are comprised of a collection of electrons and nuclei. If we can understand how these quantum particles interact with each other then

in principle we can understand the many electrical, optical, and magnetic properties of the material. Since the 1920's it has been known that such a collection of quantum particles can be fully described by solving the Schrödinger equation [90]. Equation 2.1 shows the time-independent many-body Schrödinger equation ignoring relativistic effects:

$$E\Psi = \hat{H}\Psi, \tag{2.1}$$

where Ψ is the many-body wavefunction. It is dependent on the positions of all the electrons and nuclei in the system so that

$$\Psi = \Psi(\mathbf{r}_1, \mathbf{r}_2, ..., \mathbf{r}_N; \mathbf{R}_1, \mathbf{R}_2, ..., \mathbf{R}_M), \tag{2.2}$$

for N electrons and M nuclei. The Hamiltonian can be written as

$$\begin{aligned}\hat{H} = &-\sum_i \frac{\hbar^2}{2m_e}\nabla_i^2 - \sum_I \frac{\hbar^2}{2M_I}\nabla_I^2 + \frac{1}{2}\sum_{i\neq j}\frac{e^2}{4\pi\epsilon_0}\frac{1}{|\mathbf{r}_i - \mathbf{r}_j|} \\ &+ \frac{1}{2}\sum_{I\neq J}\frac{e^2}{4\pi\epsilon_0}\frac{Z_I Z_J}{|\mathbf{R}_I - \mathbf{R}_J|} - \sum_{i,I}\frac{e^2}{4\pi\epsilon_0}\frac{Z_I}{|\mathbf{r}_i - \mathbf{R}_I|},\end{aligned} \tag{2.3}$$

i and j are the indexes on the electrons, I and J the nuclei, r_i and m_e are the positions and masses of the electrons, $\mathbf{R}_I$ and M_I are the positions and masses of the nuclei, and Z_I is the atomic number of the nucleus I. It can be seen that the first two terms are the kinetic energy of the electrons and nuclei respectively. The final three terms all arise from the Coulomb interaction between charged particles. The third term is the potential energy due to the Coulomb interaction between two electrons. The fourth term is the potential energy of the nucleus-nucleus Coulomb interaction, and the last term is the potential energy of the electron-nucleus Coulomb interaction. It is convenient here to introduce Hartree atomic

units ($\hbar = m_e = e = \frac{1}{4\pi\epsilon_0} = 1$) which will be used for the rest of this thesis and simplify this Hamiltonian to

$$\begin{aligned}\hat{H} = &-\sum_i \frac{\nabla_i^2}{2} - \sum_I \frac{\nabla_I^2}{2M_I} + \frac{1}{2}\sum_{i\neq j} \frac{1}{|\mathbf{r}_i - \mathbf{r}_j|} \\ &+ \frac{1}{2}\sum_{I\neq J} \frac{Z_I Z_J}{|\mathbf{R}_I - \mathbf{R}_J|} - \sum_{i,I} \frac{Z_I}{|\mathbf{r}_i - \mathbf{R}_I|}.\end{aligned} \tag{2.4}$$

If we now solve equation (2.4) to find the lowest energy eigenstate, that is the ground state of the system, then we can calculate any equilibrium properties of the system. Unfortunately solving this equation is not possible except for very small systems due to the electron-electron potential which couples each electron to all of the other electrons in the system. The complexity of the solution to equation (2.4) increases exponentially with system size and so for this reason appropriate approximations must be made [91].

2.1.1 Born-Oppenheimer Approximation

The nuclei are far more massive than electrons and so move much slower. It is therefore possible to separate the movement of the nuclei and electrons. This is known as the Born-Oppenheimer or adiabatic approximation [92]. We can now consider that the nuclei are fixed in space and with an effectively infinite mass, $M_I{=}\infty$. This has a dramatic effect on the Hamiltonian as the kinetic energy of the nuclei can be omitted and the Coulomb interaction between nuclei becomes a constant. By regarding the nuclear positions as external parameters and the many-body wavefunction as dependent only on electron coordinates, an electronic Schrödinger equation can be written so that the nuclear coordinates no longer

appear:

$$\left[-\sum_i \frac{\nabla_i^2}{2} + \sum_i V_n(\mathbf{r}_i) + \frac{1}{2}\sum_{i\neq j}\frac{1}{|\mathbf{r}_i - \mathbf{r}_j|}\right]\Psi = E_e\Psi, \tag{2.5}$$

where

$$E_e = E - \frac{1}{2}\sum_{I\neq J}\frac{Z_I Z_J}{|\mathbf{R}_I - \mathbf{R}_J|}, \tag{2.6}$$

and the Coulomb potential of the nuclei experienced by the electrons is

$$V_n(\mathbf{r}) = -\sum_I \frac{Z_I}{|\mathbf{r} - \mathbf{R}_I|}. \tag{2.7}$$

2.1.2 Independent Electron Approximation

The independent electron approximation states that by ignoring the interaction between electrons we can reformulate the many-body Schrödinger equation as a set of one electron equations

$$\hat{H}_0\phi_i(\mathbf{r}_i) = \epsilon_i\phi_i(\mathbf{r}_i), \tag{2.8}$$

where the independent electron Hamiltonian is

$$\hat{H}_0 = -\frac{\nabla_i^2}{2} + V_n(\mathbf{r}), \tag{2.9}$$

and the many-electron wavefunction can be decomposed into single-electron wavefunctions as

$$\Psi(\mathbf{r}_1, \mathbf{r}_2, ..., \mathbf{r}_N) = \phi_1(\mathbf{r}_1)\phi_2(\mathbf{r}_2)...\phi_N(\mathbf{r}_N). \tag{2.10}$$

These "non-interacting" single-electron equations are far simpler to solve for than equation (2.5). Another benefit of the independent electron approximation is that the electronic charge density, n($\mathbf{r}$), is the sum of the probabilities of finding

the electron in each state

$$n(\mathbf{r}) = \sum_i |\phi_i(\mathbf{r})|^2. \tag{2.11}$$

However, the approximation is not really justified as the missing electron-electron interaction is of the same energy scale as the other terms and so shouldn't be neglected in any meaningful calculation.

2.1.3 Hartree Approximation

In 1928 Hartree improved upon the independent-electron approximation by introducing an average potential acting on each electron known as the Hartree potential, V_H [93]. This potential satisfies Poisson's equation

$$\nabla^2 V_H(\mathbf{r}) = -4\pi n(\mathbf{r}), \tag{2.12}$$

with the solution

$$V_H(\mathbf{r}) = \int d\mathbf{r}' \frac{n(\mathbf{r}')}{|\mathbf{r} - \mathbf{r}'|} d\mathbf{r}'. \tag{2.13}$$

The single-electron Schrödinger equations now become

$$\left[-\frac{\nabla^2}{2} + V_n(\mathbf{r}) + V_H(\mathbf{r}) \right] \phi_i(\mathbf{r}) = \epsilon_i \phi_i(\mathbf{r}). \tag{2.14}$$

The problem of solving the $3N$ dimensional many-body Schrödinger equation of equation (2.4) has now become the much simpler problem of solving the three coupled N-dimensional equations (2.11), (2.12), and (2.14). This can be approached using a self-consistent field method.

2.2 Density Functional Theory

Density functional theory (DFT) has become one of the most widely used and successful methods for calculating the electronic structure of materials [94]. It is an independent-particle approach which, at least in principle, provides an exact theory of many-body systems.

2.2.1 The Hohenberg-Kohn Theorems

The basis of density functional theory lies in two theorems first proven by Hohenberg and Kohn in 1964 [95]. These state that:

Theorem I: For any system of interacting fermions in an external potential $V_{\text{ext}}(\mathbf{r})$, the potential $V_{\text{ext}}(\mathbf{r})$ is uniquely determined by the ground state particle density $n_0(\mathbf{r})$, except for a constant.

Theorem II: There exists a universal functional for the energy $E[n]$ in terms of the density $n(\mathbf{r})$ which is independent of the external potential $V_{\text{ext}}(\mathbf{r})$. For any particular $V_{\text{ext}}(\mathbf{r})$, the exact ground state energy of the system is the global minimum value of this functional, and the density $n(\mathbf{r})$ that minimises the functional is the exact ground state density $n_0(\mathbf{r})$.

From the first theorem it can be seen that since the Hamiltonian must be fully determined except for a constant shift in energy, the many-body wavefunctions for all states must also be determined. Therefore the ground state density $n_0(\mathbf{r})$ is all that is needed to calculate all properties of the system. The second theorem tells us that the functional $E[n]$ is sufficient to determine the exact ground state energy and

density. Unfortunately the universal functional which relates energy and density is not known. The Hohenberg-Kohn theorems therefore do not provide a method to calculate the properties of a system; for that, the Kohn-Sham equations are needed.

2.2.2 The Kohn-Sham Equations

The great success of DFT relies on the approach proposed by Kohn and Sham in 1965 [96]. The original many-body system is replaced by a fictitious auxiliary system and it is assumed that the ground state particle density is the same for both systems. This assumption is generally thought to be valid and is called "non-interacting-V-representability".

From the work of Hohenberg and Kohn it can be shown that the total energy of many electrons in the ground state is a functional of the electron density. This can be written as:

$$E_{\text{tot}} = F[n] = \int d\mathbf{r} n(\mathbf{r}) V_n(\mathbf{r}) + T_s[n(\mathbf{r})] + \langle \Psi[n] | \hat{T} + \hat{W} | \Psi[n] \rangle . \tag{2.15}$$

Where the kinetic energy, $\hat{T}$, is

$$\hat{T} = -\sum_i \frac{\nabla_i^2}{2}, \tag{2.16}$$

and the Coulomb energy, $\hat{W}$, is

$$\hat{W} = \frac{1}{2} \sum_{i \neq j} \frac{1}{|\mathbf{r}_i - \mathbf{r}_j|}. \tag{2.17}$$

The potential felt by the electrons due to the nuclei is already dependent on

the particle density but the other terms only depend on particle density implicitly. Kohn and Sham split these terms into the kinetic energy and Coulomb energy of independent electrons plus an extra term which accounts for any difference, E_{xc}:

$$F[n] = \int d\mathbf{r} n(\mathbf{r}) V_n(\mathbf{r}) + \hat{T}[n(\mathbf{r})] + E_H[n(\mathbf{r})] + E_{xc}[n(\mathbf{r})], \tag{2.18}$$

where E_{xc} is known as the exchange and correlation energy. This term contains all the contributions to the unknown functional $F[n]$ which are not covered by the independent electron approximation.

By requiring the one-particle Kohn-Sham wavefunctions to be orthogonal, ie. $\langle \phi_i | \phi_j \rangle = \delta_{ij}$ where δ_{ij} is the Kronecker delta, and minimising the functional $\left(\frac{\delta F[n]}{\delta n} = 0\right)$ using Lagrange multipliers, the Shrödinger-like Kohn-Sham equations can be derived:

$$\hat{H}_{KS}\phi_i(\mathbf{r}) = \epsilon_i \phi_i(\mathbf{r}). \tag{2.19}$$

For each of the N one-electron Shrödinger-like equations the Hamiltonian is defined as

$$\hat{H}_{KS} = -\frac{1}{2}\nabla^2 + V_{KS}(\mathbf{r}), \tag{2.20}$$

where the Kohn-Sham potential is:

$$\begin{aligned} V_{KS}(\mathbf{r}) &= V_n(\mathbf{r}) + \frac{\delta E_H}{\delta n(\mathbf{r})} + \frac{\delta E_{xc}}{\delta n(\mathbf{r})} \\ &= V_n(\mathbf{r}) + V_H(\mathbf{r}) + V_{xc}(\mathbf{r}). \end{aligned} \tag{2.21}$$

Equations (2.19), (2.20) and (2.21) are known as the Kohn-Sham equations. They take on the form of independent-particle equations with a potential that must be calculated self-consistently with the particle-density. The total energy

E_{KS} can be found using equation (2.15) and the density using equation (2.11). In the case of the exact functional E_{xc}, the solution to these equations yields the exact ground state density and energy of the fully interacting system. In practice the exact exchange-correlation functional is unknown and so appropriate approximations must be made. It is of the utmost importance that any DFT calculations hoping to produce satisfactory properties of realistic systems must use an accurate exchange-correlation functional. The two most common approximations for E_{xc} are the local density approximation (LDA) and the generalised gradient approximation (GGA) [97–100].

2.2.3 Exchange-Correlation Approximations

By using the Kohn-Sham ansatz of mapping the original interacting many-body system onto a set of N independent single-particle equations, the complexity of the problem is greatly reduced. As the exact form of the exchange-correlation energy is unknown, the Kohn-Sham equations are unsolvable and so appropriate approximations for E_{xc} are needed.

Another useful feature of the Kohn-Sham ansatz is that by explicitly separating the independent-particle kinetic energy and the long-range Hartree terms, the remaining exchange-correlation functional can be reasonably approximated as a local or near-local function of the particle density. Solids can often be considered as close to the limit of the homogeneous electron gas, and so as a first approximation Kohn and Sham proposed the local density approximation (LDA). In LDA, the exchange-correlation energy is an integral over all space in which the exchange-correlation energy density at each point is considered to be identical to

the homogeneous electron gas with that density:

$$E_{xc}[n(\mathbf{r})] = \int d\mathbf{r} n(\mathbf{r}) \epsilon_{xc}[n(\mathbf{r})], \tag{2.22}$$

where ϵ_{xc} is the exchange-correlation energy per electron of a homogeneous electron gas of density $n(\mathbf{r})$. This term can be split into exchange and correlation components, $\epsilon_{xc} = \epsilon_x + \epsilon_c$. The exchange energy per electron of the homogeneous gas is given by a simple analytic form:

$$\epsilon_x = -\frac{3}{4}\left(\frac{3}{\pi}\right)^{\frac{1}{3}} n^{\frac{1}{3}}. \tag{2.23}$$

The LDA exchange energy is therefore

$$E_x^{LDA}[n(\mathbf{r})] = -\frac{3}{4}\left(\frac{3}{\pi}\right)^{\frac{1}{3}} \int d\mathbf{r} n(\mathbf{r})^{\frac{4}{3}}. \tag{2.24}$$

The correlation energy has been calculated to a very high accuracy using quantum Monte Carlo methods by Ceperley and Alder [97]. It has subsequently been parameterised by various groups, perhaps most famously by Perdew and Zunger [98]. This allows for practical DFT to be carried out using the LDA.

The LDA is only exact for studying the homogeneous electron gas and can be justified for use with systems where the density varies slowly. In systems where this is not the case, attempts to improve upon the LDA have been made. These are known as generalised-gradient approximations (GGAs). By incorporating density gradient corrections $\nabla n(\mathbf{r})$ and higher spatial derivatives of the density, inhomogeneities of the real density can be more accurately described:

$$E_{xc}^{GGA}[n(\mathbf{r})] = \int \epsilon_{xc}^{GGA}\left[n(\mathbf{r}), |\nabla n(\mathbf{r})|\right] n(\mathbf{r}) d\mathbf{r}. \tag{2.25}$$

A number of widely used GGA functionals such as PBE and PW91 have been developed from different parameterisations of this expansion. While GGA is known to better predict bond lengths and binding energies in systems with rapidly varying charge density, it is by no means a universal improvement over the LDA [99, 100].

2.3 Solving the Kohn-Sham Equations

By using the Kohn-Sham equations with a suitable approximation for the exchange-correlation term, the particle-density and ground state energy of the system can be calculated. The N independent-particle equations must be solved self-consistently as the Kohn-Sham potential is itself dependent on the particle density that is to be calculated. This truly is a first principles approach as the only inputs needed are the atomic numbers and the position of the ions. These are used to construct the potential felt by the electrons from the ions, $V_n(\mathbf{r})$.

In a typical calculation an initial guess is necessary for the particle-density, and this is made using the sum of the atomic densities:

$$n_0(\mathbf{r}) = \sum_I n_I(\mathbf{r} - \mathbf{R}_I), \tag{2.26}$$

where the density n_I is usually chosen as the pseudo-valence density.

The next step is to generate the Kohn-Sham potential V_{KS} and solve the Schrödinger-like Kohn-Sham equations so as to obtain the single-particle wave-functions ϕ_{KS}. From these wavefunctions the new density of the system can be calculated as:

$$n(\mathbf{r}) = \sum_i |\phi_i(\mathbf{r})|^2, \tag{2.27}$$

as in equation (2.11).

This new density is compared to the input density, and if they are equal or within a small threshold value of each other, then the self-consistent loop is complete. If not, then the Kohn-Sham potential is recalculated and the cycle continues. This recalculated density is generally some form of linear mixing of the new calculated density (n') with the density of the previous iteration (n_{m}). A simple linear mixing scheme would be

$$n_{m+1} = \beta n' + (1 - \beta) n_m, \tag{2.28}$$

for each iteration m. The mixing parameter β is typically of the order 0.4-0.8, where a large value provides a quicker convergence but can also lead to numerical instabilities. More complex mixing schemes such as Broyden mixing have been developed which increase convergence speed [101]. The work in this thesis has used such a mixing scheme.

It should be noted that although conceptually it makes sense to compare densities to check for self-consistency, in practice it is the total energy which is usually compared. In terms of calculation time, the largest part of the problem is the solving of the Kohn-Sham equations with a certain potential, V_{KS}. There are several methods by which this can be achieved, such as the atomic sphere method or localised atomic-like orbitals. This work uses only the plane wave approach to DFT and so that is what will be described here. A schematic of a complete plane waves DFT calculation is shown in Fig 2.1.

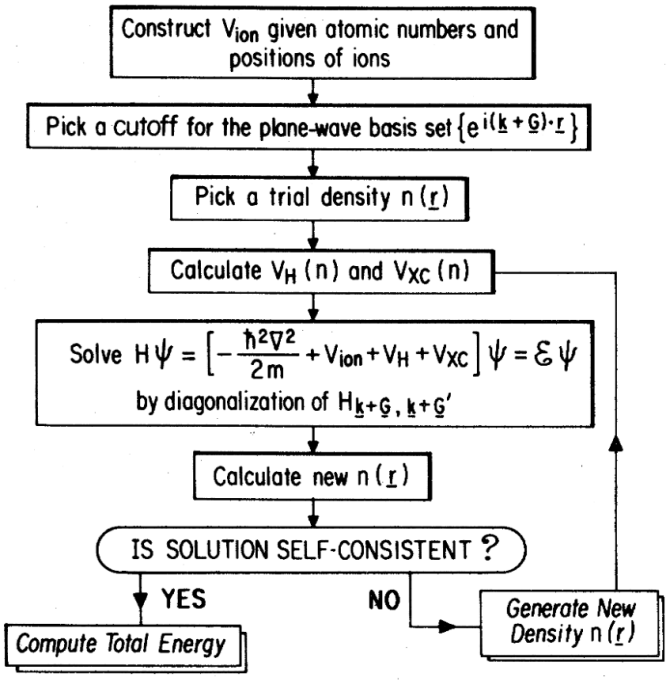


Figure 2.1: A flowchart of a DFT calculation. From [102].

2.3.1 Plane Wave Basis Set

The Kohn-Sham wavefunctions can be expanded in a complete set of plane waves

$$\phi_{i\mathbf{k}}(\mathbf{r}) = \frac{1}{\sqrt{\Omega}} \sum_{\mathbf{G}} c_{i,\mathbf{k}}(\mathbf{G}) e^{i(\mathbf{k}+\mathbf{G})\cdot\mathbf{r}}, \tag{2.29}$$

where G is the reciprocal lattice vector, Ω is the unit cell volume and $c_{i,\mathbf{k}}(\mathbf{G})$ is a complex coefficient.

The number of reciprocal lattice vectors is in principle infinite, making a sum over them not computationally possible. However, the wavefunctions in realistic systems become smoothly varying at small scales and so for the largest **G**-vectors the plane wave components become negligible. The sum can therefore be truncated and only **G**-vectors within a certain cutoff radius are included. This radius can be

defined in terms of the corresponding energy cutoff, E_{cut}:

$$G_{cut} = \sqrt{2E_{\mathrm{cut}}}. \tag{2.30}$$

It is important to establish an appropriate cutoff energy for any plane wave calculation and this will be system-dependent. Usually a convergence test is performed whereby the total energy of the system is calculated with increasing cutoff energy until the result stops changing. Typical cutoff energies are 20-100 Ry depending on the system and the type of pseudopotential used.

The density is also expanded in plane waves and this too has a cutoff energy. For norm-conserving pseudopotential the density cutoff is four times the plane wave energy cutoff, while the presence of the augmentation charge in ultrasoft calculations requires a density cutoff of up to ten times that of the plane wave energy cutoff.

In order to accurately sample the Brillouin zone a finite number of **k**-points must be used. So long as the wavefunctions vary smoothly with respect to **k** this can be justified. Again the number of **k**-points is system-dependent and so must be determined via a convergence test. Unbiased grids of **k**-points for sampling the Brillouin zone have been produced by Monkhorst and Pack [103].

2.3.2 Pseudopotentials

Very near the nucleus the electronic wavefunctions oscillate rapidly due to the interaction with the positively charged nucleus. In order to describe such rapid oscillations plane waves with very short wavelengths are required. This results in a very large plane wave energy cutoff and hence is very computationally demanding. As most of the calculation cell is occupied by wavefunctions which do not oscillate

rapidly, the majority of the computational demand is wasted. For this reason it is very common when using a plane wave approach to DFT to use pseudopotentials rather than all-electron calculations.

In the pseudopotential method the electronic wavefunctions are expanded using a much smaller set of plane waves. The core electrons, which are usually defined as electrons in "closed shells", are thought of as frozen and combined with their nucleus to construct a new ionic pseudopotential. This acts on a set of pseudo-wavefunctions of the valence electrons rather then the true wavefunction. It has been known since the early 20^{th} century that valence electrons are more sensitive to their chemical bonding environment while core electrons are relatively inert, so this approximation is justified for most elements [104]. In cases where the valance contains only a very small number of electrons, such as Li or Na, it is necessary to include the semi-core electrons in the valence or use a non-linear core correction.

The pseudopotential is designed so that outside of some core radius, r_c, the pseudo wavefunctions are identical to the wavefunctions of single-particle all-electron calculations. Inside of this radius, the pseudo wavefunction is smoother than the all-electron wavefunctions, with no nodes, making it computationally cheaper to process as fewer plane waves are needed to accurately describe it. Figure 2.2 shows a schematic of the comparison between the computationally demanding all-electron wavefunctions and potential and the pseudo wavefunctions and pseudopotential. It is of key importance that the core radius is small enough so that it does not overlap with the region of the wavefunctions involved in chemical bonding.

In order to retain the properties of the all-electron wavefunctions, pseudopotentials must be made as accurate and transferable as possible. One method to reach that goal is to enforce that the integrals of the squared all-electron wavefunctions

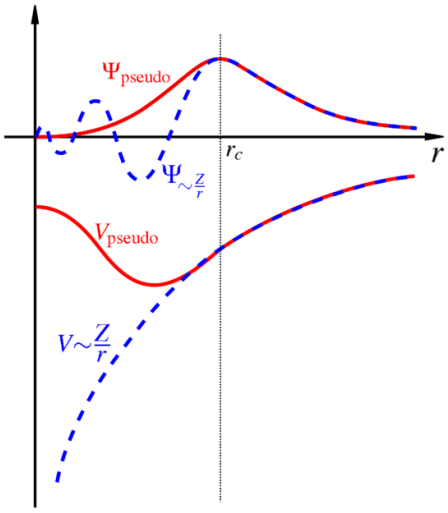


Figure 2.2: Schematic of all-electron (dotted lines) and pseudo (solid lines) potentials and their corresponding wavefunctions. From [102].

match the integral of the squared pseudo wavefunction within the core region:

$$\int_0^{r_c} d\mathbf{r}|\phi_i^{AE}(\mathbf{r})|^2 = \int_0^{r_c} d\mathbf{r}|\phi_i^{PS}(\mathbf{r})|^2, \tag{2.31}$$

which ensures that the total charge within the core region is correct. Pseudopotentials generated using this construction are called "norm-conserving" pseudopotentials.

The norm-conserving condition can lead to sharply peaked orbitals especially in elements with a small core region. This can result in "hard" pseudopotentials, that is ones which require a very large number of plane waves to properly converge a DFT calculation. To address this concern, ultrasoft pseudopotentials were developed by Vanderbilt [105]. Ultrasoft pseudopotentials are of course identical outside of the core region to the all-electron potential, however inside of the core region the norm-conserving condition is relaxed. This allows great flexibility in the construction of the pseudo wavefunction but also leaves a deficit of charge. This is dealt with by the addition of an augmentation term localised in the region which

is added to the density:

$$n(\mathbf{r}) = \sum_n \left[|\phi_n|^2 + \sum_{ij} Q_{ij}(\mathbf{r}) \langle \phi_n | \beta_j \rangle \langle \beta_i | \phi_n \rangle \right], \tag{2.32}$$

where Q_{ij} are the core-localised augmentation functions and β_i are projector functions, localised in the core.

By using ultrasoft pseudopotentials rather than norm-conserving ones the energy cutoff to reach convergence can often be reduced. The main disadvantage to ultrasoft pseudopotentials is that due to the augmentation term their implementation is more invasive and so some codes, such as the `EPW` codes which will be described later, do not yet allow their use.

The Projector Augmented Wave (PAW) method was developed by Blöchl in 1994 [106]. The main idea is to reconstruct the all-electron wavefunctions close to the nucleus. Again, in the region outside of the core radius the pseudo wavefunction is correct and within the core region the potential is essentially atomic, except for a constant shift. The wavefunction therefore needs to be corrected within r_c and so can be expanded in terms of the all-electron partial waves up to r_c. In the region in which the all-electron partial waves are added, the corresponding pseudo partial waves have to be subtracted. The weights for the superposition are determined by projectors localised within r_c. The full all-electron wavefunctions are expressed as a combination of integrals of smooth functions extending through space plus localised contributions:

$$|\phi^{AE}\rangle = |\phi^{PS}\rangle + \sum_i (|\psi_i^{AE}\rangle - |\psi_i^{PS}\rangle) \langle 0_i | \phi_i^{PS} \rangle, \tag{2.33}$$

where $|\psi_i^{AE}\rangle$ and $|\psi_i^{PS}\rangle$ are the all-electron partial waves and the pseudo partial

waves respectively. $|0_i\rangle$ is a projector for each pseudo partial wave localised within r_c.

2.4 Structural Optimisation

The adiabatic approximation of Born and Oppenheimer allows us to decouple the dynamics of electrons and nuclei. The many-body Schrödinger equation for the nuclei can be written as:

$$\left[-\sum_I \frac{\nabla_I^2}{2M_I} + \frac{1}{2}\sum_{I\neq J}\frac{Z_I Z_J}{|\mathbf{R}_I - \mathbf{R}_J|} + E_e(\mathbf{R}_1, ..., \mathbf{R_M})\right]\chi = E\chi, \tag{2.34}$$

where $\chi(\mathbf{R}_1, ..., \mathbf{R}_M)$ is a nuclei-only wavefunction which depends parametrically on the nucleus coordinates $\mathbf{R}_1$, ..., $\mathbf{R}_M$. $\mathrm{E}_e(\mathbf{R}_1$, ..., $\mathbf{R}_M)$ is the total electronic energy which acts as an effective potential on the nuclei and contains all of the effects of the electrons in the system. Together with the Coulomb repulsion between nuclei, $E_N(\mathbf{R})$, this forms the total potential energy of the nuclei which is known as the Born-Oppenheimer energy surface, $U(\mathbf{R}_1, ..., \mathbf{R}_M)$:

$$\begin{aligned} U(\mathbf{R}_1, ..., \mathbf{R}_M) &= E_N(\mathbf{R}) + E_e(\mathbf{R}_1, ..., \mathbf{R}_M) \\ &= \frac{1}{2}\sum_{I\neq J}\frac{Z_I Z_J}{|\mathbf{R}_I - \mathbf{R}_J|} + \int n(\mathbf{r})V_n(\mathbf{r})d\mathbf{r} \\ &\quad + \langle\psi|\,\hat{T} + \hat{W}\,|\psi\rangle\,. \end{aligned} \tag{2.35}$$

By treating the nuclei as classical particles, the forces on the nuclei can be expressed as:

$$F_I = -\frac{\partial U(\mathbf{R})}{\partial R_I}. \tag{2.36}$$

The equilibrium geometry of a system can therefore be found by minimising the Born-Oppenheimer energy surface with respect to all of the $3M$ nuclear degrees of freedom, so that the forces acting on the individual nuclei vanish. One approach to determining the equilibrium geometry of the material is to calculate each derivative $\partial U/\partial \mathbf{R}$ using a finite difference method. This is achieved by slightly displacing an atom along any Cartesian direction and comparing the potential energy, U, to the potential energy of the undisplaced structure. It therefore requires $3M + 1$ evaluations of U to determine the forces on the nuclei in one structural geometry. This is very time consuming as each calculation of U requires a DFT calculation to find the total energy of the system with those exact nuclear coordinates, and a much less computationally intensive evaluation of the nucleus-nucleus repulsion. A much more computationally efficient approach exploits the Hellmann-Feynman theorem [107, 108].

2.4.1 Hellmann-Feynman Theorem

The Hellmann-Feynman theorem states that the first derivative of the eigenvalues of a Hamiltonian, H_λ, that depend on a parameter, λ, is given by the expectation value of the derivative of the eigenvalues of the Hamiltonian:

$$\frac{\partial E_\lambda}{\partial \lambda} = \langle \Psi_\lambda | \frac{\partial H_\lambda}{\partial \lambda} | \Psi_\lambda \rangle , \tag{2.37}$$

where Ψ_λ is the eigenfunction corresponding to the E_λ eigenvalue: $H_\lambda\Psi_\lambda = E_\lambda\Psi_\lambda$. The proof of this result is as follows:

$$\begin{aligned}
\frac{\partial E_\lambda}{\partial\lambda} &= \frac{\partial(\langle\Psi_\lambda|\, H_\lambda\, |\Psi_\lambda\rangle)}{\partial\lambda} \\
&= \langle\frac{\partial\Psi_\lambda}{\partial\lambda}|\, H_\lambda\, |\Psi_\lambda\rangle + \langle\Psi_\lambda|\, \frac{\partial H_\lambda}{\partial\lambda}\, |\Psi_\lambda\rangle + \langle\Psi_\lambda|\, H_\lambda\, |\frac{\partial\Psi_\lambda}{\partial\lambda}\rangle \qquad (2.38) \\
&= \langle\Psi_\lambda|\, \frac{\partial H_\lambda}{\partial\lambda}\, |\Psi_\lambda\rangle + E_\lambda\frac{\partial}{\partial\lambda}\, \langle\Psi_\lambda|\Psi_\lambda\rangle \qquad (2.39) \\
&= \langle\Psi_\lambda|\, \frac{\partial H_\lambda}{\partial\lambda}\, |\Psi_\lambda\rangle\,. \qquad (2.40)
\end{aligned}$$

By applying this to calculate the forces on the nuclei it can be shown that

$$\begin{aligned}
F_I = -\frac{\partial U(\mathbf{R})}{\partial\mathbf{R}_I} &= -\langle\Psi|\, \frac{\partial H}{\partial\mathbf{R}_I}\, |\Psi\rangle \\
&= -\int d\mathbf{r} n_{\mathbf{R}}(\mathbf{r})\frac{\partial V_n(\mathbf{r})}{\partial\mathbf{R}_I}d\mathbf{r} - \frac{\partial E_N(\mathbf{R})}{\partial\mathbf{R}_I} \\
&= Z_I\left[\int d\mathbf{r} n_{\mathbf{R}}(\mathbf{r})\frac{\mathbf{r}-\mathbf{R}_I}{|\mathbf{r}-\mathbf{R}_I|^3} - \sum_{J\neq I} Z_J\frac{\mathbf{R}_J-\mathbf{R}_I}{|\mathbf{R}_J-\mathbf{R}_I|^3}\right], \qquad (2.41)
\end{aligned}$$

where $V_n(\mathbf{r})$ is the electron-nuclei interaction defined in equation (2.7) and $n_{\mathbf{R}}(\mathbf{r})$ is the electron charge density corresponding to the nuclear coordinates $\mathbf{R}$.

From equation (2.41) it can be seen that the forces for all M atoms of the system can be determined using only the particle-density for that set of nuclear coordinates. The number of DFT calculations to obtain the forces is therefore one rather than the $3M + 1$ needed by a finite difference method.

In practice, to find the optimal geometry of a material, an initial guess is made for the atomic positions, and the density and total energy of the system are calculated as usual by self-consistently solving equations (2.19), (2.20) and (2.21). The Hellmann-Feynman forces for this particular configuration can be calculated

and the ionic positions are updated to minimise these forces. Algorithms based on Newton's equations of motion such as the Broyden-Fletcher-Goldfarb-Shanno (BFGS) method have been developed to most effectively find the minimum of the potential energy surface [109]. The system is therefore structurally relaxed until the forces acting on the ions are below a specified threshold, usually of the order of 10 meV per atom.

2.5 Phonons

A collective oscillation of a sub-lattice of atoms at the same frequency in a crystalline solid is known as a phonon. They are the quantum mechanical equivalent of normal modes of vibration and can be considered well-defined excitations with momentum $\hbar\mathbf{q}$ and energy $\hbar\omega$. At each phonon wavevector $\mathbf{q}$ there are $3M$ phonon modes. The three lowest energy modes, that is those with zero frequency at $\mathbf{q} = 0$, are known as acoustic modes. These are responsible for carrying sound waves. All phonon modes at $\mathbf{q} = 0$ which have non-zero frequencies are known as optical phonons because they can be excited by infrared radiation.

2.5.1 Lattice Dynamics

In order to calculate phonon frequencies the dynamics of the lattice must be understood. In a periodic crystal the position of any nucleus can be written as the sum of the unit cell lattice vector ($\mathbf{R}_l$) and a vector describing the position of the nucleus within the unit cell (τ_s):

$$\mathbf{R}_I = \mathbf{R}_l + \tau_s, \tag{2.42}$$

where l is the unit cell label and s the label of the atom such that $I = (l, s)$. If the approximation that the nuclei are fixed in position is relaxed and it is instead assumed that they vibrate with a very small displacement from their equilibrium positions, we can express the time-dependent position of each nucleus as:

$$\mathbf{R}_I(t) = \mathbf{R}_I^0 + \mathbf{u}_I(t), \tag{2.43}$$

where $\mathbf{R}_I^0$ is the time-independent equilibrium position of the nucleus I and $\mathbf{u}_I(t)$ is the instantaneous displacement of that atom. Again approximating the nuclei as classical particles and using Newton's equations, the motion of each nuclei displacement is:

$$M_I \ddot{\mathbf{u}}_I = -\frac{\partial U}{\partial \mathbf{u}_I}, \tag{2.44}$$

where the partial derivatives are calculated at the equilibrium positions, $\mathbf{R}_I^0$. A Taylor expansion of the Born-Oppenheimer energy surface up to second order in the atomic displacement gives:

$$U(\mathbf{R}_I) = U(\mathbf{R}_I^0) + \sum_{I\alpha} u_{I\alpha} \frac{\partial U}{\partial R_{I\alpha}} + \frac{1}{2} \sum_{I\alpha, J\beta} u_{I\alpha} u_{J\beta} \frac{\partial^2 U}{\partial R_{I\alpha} \partial R_{J\beta}}, \tag{2.45}$$

where α and β denote Cartesian directions. The second partial derivatives of the Born-Oppenheimer energy surface with respect to the nuclear positions, evaluated at the equilibrium positions, are known as the interatomic or Born-von-Karman force constants [110]:

$$C_{ls\alpha, l's'\beta} = \frac{\partial^2 U}{\partial(R_{l\alpha} + \tau_{s\alpha})\partial(R_{l'\beta} + \tau_{s'\beta})} = C_{s\alpha, s'\beta}(\mathbf{R}_l - \mathbf{R}_{l'}). \tag{2.46}$$

Thus, by defining the total energy corresponding to the nuclei at their equilibrium positions as U_0, and remembering that the forces on the nuclei are $F_I = -\partial U/\partial R_{I\alpha}$, equation (2.45) can be rewritten as:

$$U(\mathbf{R}) = U_0 - \sum_{I\alpha} F_{I\alpha} u_{I\alpha} + \frac{1}{2} \sum_{ls\alpha, l's'\beta} u_{ls\alpha} u_{l's'\beta} C_{ls\alpha, l's'\beta}. \tag{2.47}$$

At equilibrium the forces on the nuclei vanish and so

$$U(\mathbf{R}) = U_0 + \frac{1}{2} \sum_{ls\alpha, l's'\beta} u_{ls\alpha} u_{l's'\beta} C_{ls\alpha, l's'\beta}. \tag{2.48}$$

Equation (2.48) defines the *harmonic approximation*, in which terms greater than second order in the Taylor expansion are very small and so neglected. Higher order terms are referred to as anharmonic contributions and become far more important at higher temperatures [111]. By combining this equation with (2.44), Newton's equation for the nuclei in the harmonic approximation can be derived:

$$M_s \ddot{u}_{ls\alpha} = -\sum_{l's'\beta} C_{ls\alpha, l's'\beta} u_{l's'\beta}. \tag{2.49}$$

Looking for a solution in the form of a propagating wave, the instantaneous displacement of atom s in unit cell l along Cartesian direction α is defined as

$$u_{ls\alpha}(t) = u^0_{s\alpha} e^{i[\mathbf{q}\cdot(\mathbf{R}_l + \tau_s) - \omega t]}, \tag{2.50}$$

where $u^0_{s\alpha}$ is a constant. Substituting this expression into the Newton equation for the nuclei in the harmonic approximation we obtain the eigenvalue problem:

$$\sum_{s'\beta} D_{s\alpha, s'\beta}(\mathbf{q}) \upsilon_{s'\beta} = \omega^2 \upsilon_{s\alpha}, \tag{2.51}$$

with the mass-scaled vibrational modes

$$\upsilon_{s\alpha} = M_s^{\frac{1}{2}} u^0_{s\alpha}, \tag{2.52}$$

and the dynamical matrix

$$D_{s\alpha,s'\beta}(\mathbf{q}) = \frac{1}{\sqrt{M_s M_{s'}}} \sum_l e^{i\mathbf{q}\cdot\mathbf{R}_l} e^{i\mathbf{q}\cdot(\tau_{s'}-\tau_s)} C_{ls\alpha,l's'\beta}. \tag{2.53}$$

In a practical calculation the dynamical matrix is calculated first. This can be achieved either via a "frozen phonon" approach or using density functional perturbation theory (DFPT). The latter is outlined in the following section and an extensive review has been published by Baroni *et al.* [112]. In the former, the forces acting on the nuclei are calculated using the Hellmann-Feynman theorem. The first derivatives of the forces with respect to nuclear coordinates are then obtained via a finite difference method. The force on a nucleus I is calculated when the nuclei J is displaced from its equilibrium position by a small amount $\pm u$ and from this the derivative is calculated. This derivative is exactly the Born-von-Karman force constants, from which the dynamical matrix at each wavevector, $\mathbf{q}$, can be obtained using a Fourier transform of equation (2.53). In total $2 \times 3M$ DFT calculations for all the nuclear configurations are needed to calculate the full dynamical matrix. This is less efficient than linear response methods. Another disadvantage to this approach is that supercells of several unit cells are often needed as the wavevector of the phonon must be commensurate with the unit cell. This adds significantly to the size of the system under study and therefore to the computational demand.

2.5.2 Density Functional Perturbation Theory

It is known that the phonon frequencies of a system are solutions of the secular equation

$$\det \left| \frac{1}{\sqrt{M_s M_{s'}}} D_{s\alpha,s'\beta}(\mathbf{q}) - \omega^2(\mathbf{q}) \right| = 0. \tag{2.54}$$

From equation (2.53) it can be seen that the dynamical matrix is dependent on the interatomic force constants, which are the second partial derivatives of the ground state energy with respect to displacement. The Hellmann-Feynman theorem allows us to calculate the first and second derivatives of the Born-Oppenheimer energy surface as:

$$\frac{\partial U}{\partial u_{ls\alpha}} = -F_{ls\alpha} = \int \frac{\partial V_n(\mathbf{r})}{\partial u_{ls\alpha}} n_{\mathbf{R}}(\mathbf{r}) d\mathbf{r} - \frac{\partial E_N}{\partial u_{ls\alpha}} \tag{2.55}$$

$$\begin{aligned} \frac{\partial U}{\partial u_{ls\alpha} \partial u_{l's'\beta}} &= -\frac{\partial F_{ls\alpha}}{\partial u_{ls\alpha}} = \int \frac{\partial^2 V_n(\mathbf{r})}{\partial u_{ls\alpha} \partial u_{l's'\beta}} n_{\mathbf{R}}(\mathbf{r}) d\mathbf{r} \\ &+ \int \frac{\partial n_{\mathbf{R}}(\mathbf{r})}{\partial u_{l's'\beta}} \frac{\partial V_n(\mathbf{r})}{\partial u_{ls\alpha}} d\mathbf{r} + \frac{\partial^2 E_N}{\partial u_{ls\alpha} \partial u_{l's'\beta}}. \end{aligned} \tag{2.56}$$

Calculation of the Hessian of the Born-Oppenheimer energy surface therefore requires not only the ground state electron charge density of that exact set of nuclear coordinates, $n_{\mathbf{R}}(\mathbf{r})$, but also its linear response to a perturbation, $\partial n_{\mathbf{R}}(\mathbf{r})/\partial u_{l's'\beta}$. Linerisation of equation (2.11) results in:

$$\frac{\partial n(\mathbf{r})}{\partial u_{l's'\beta}} = \sum_i^N \left[\frac{\partial \phi_i^*(\mathbf{r})}{\partial u_{l's'\beta}} \phi_i(\mathbf{r}) + \phi_i^*(\mathbf{r}) \frac{\phi_i(\mathbf{r})}{\partial u_{l's'\beta}} \right]. \tag{2.57}$$

By applying the Taylor expansion in $u_{l's'\beta}$ to the Kohn-Sham potential, the Kohn-Sham orbitals and the Kohn-Sham eigenvalues, and substituting the terms into the Kohn-Sham equation (2.19), keeping only the terms in first order u, the

Sternheimer equation can be derived:

$$\left(-\frac{\nabla^2}{2}+V_{KS}-\epsilon_i\right)\frac{\partial\phi_i(\mathbf{r})}{\partial u_{l's'\beta}}=-\left(\frac{\partial V_{KS}}{\partial u_{l's'\beta}}-\frac{\partial\epsilon_i}{\partial u_{l's'\beta}}\right)\phi_i(\mathbf{r}), \tag{2.58}$$

where the response of the effective potential is given by

$$\frac{\partial V_{KS}}{\partial u_{l's'\beta}} = \frac{\partial V_n}{\partial u_{l's'\beta}}+\frac{\partial V_H}{\partial u_{l's'\beta}}+\frac{\partial V_{xc}}{\partial u_{l's'\beta}} \tag{2.59}$$

$$= \frac{\partial V_n}{\partial u_{l's'\beta}}+\int\frac{1}{|\mathbf{r}-\mathbf{r}'|}\frac{\partial n(\mathbf{r})}{\partial u_{l's'\beta}}+\frac{\partial V_{xc}}{\partial n}\frac{\partial n}{\partial u_{l's'\beta}}. \tag{2.60}$$

These equation are more usually written in a more compact form with the finite-difference operator Δ^u:

$$\Delta n(\mathbf{r}) = 2\mathrm{Re}\sum_i^N\phi_i^*(\mathbf{r})\Delta\phi_i(\mathbf{r}), \tag{2.61}$$

$$\Delta V_{KS}(\mathbf{r}) = \Delta V_n(\mathbf{r})+\int\frac{\Delta n(\mathbf{r}')}{|\mathbf{r}-\mathbf{r}'|}d\mathbf{r}'+\frac{\partial V_{xc}(n)}{\partial n}\Delta n(\mathbf{r}), \tag{2.62}$$

$$\Delta\epsilon_i = \langle\phi_i|\,\Delta V_{KS}\,|\phi_i\rangle\,. \tag{2.63}$$

where

$$\Delta^u F=\sum_i\frac{\partial F_u}{\partial u_i}\Delta u_i. \tag{2.64}$$

The response of the system to an external perturbation depends only on the component of the perturbation which couples the occupied-state manifold with the empty one. This allows the Sternheimer equation to be expressed in the nonsingular form [113]:

$$(H_{KS}-\epsilon_i)\,|\phi_i\rangle=-P_c\Delta V_{KS}\,|\phi_i\rangle\,, \tag{2.65}$$

with the projector onto the empty-state manifold defined as:

$$P_c = 1 - P_v; P_v = \sum_i^N |\phi_i\rangle \langle\phi_i| . \tag{2.66}$$

It can be seen that the equations (2.61), (2.62), (2.63), and (2.65) are interdependent and can be thought of as analogous to the Kohn-Sham equations (2.11), (2.19), (2.20) and (2.21), but for a perturbed system. The algorithm for DFPT is therefore to self-consistently solve this set of linear equations for the $3M$ perturbations at a fixed phonon wavevector $\mathbf{q}$. This allows the dynamical matrix for that phonon wavevector to be evaluated and the calculation of its eigenmodes and eigenfrequencies by diagonalisation. As the dynamical matrix is a $3M \times 3M$ matrix it yields for each wavevector $3M$ eigenfrequencies, $\omega_{\mathbf{q}\nu}$, and eigenmodes $E_{s\alpha,\nu}(\mathbf{q})$, where $\nu = 1, ..., 3M$ is referred to as the "phonon branch" or mode.

If the complete phonon dispersion, $\omega(\mathbf{q})$, is needed then this iterative process of self-consistently solving equations (2.61), (2.62), (2.63), and (2.65) should be repeated for different wavevectors of interest. This can be made more efficient by the use of Fourier interpolation of the force constants [114]. The smoother the matrix elements of the dynamical matrix as a function of $\mathbf{q}$, the smoother the phonon dispersions and the shorter the range of real-space interatomic force constants. By Fourier analysing a set of force constant matrices calculated over a uniform grid in reciprocal space, the real-space interatomic force constants can be obtained. With these real-space interatomic force constants, the dynamical matrices in reciprocal space can be obtained via another Fourier transform for any arbitrary wavevector $\mathbf{q}$ which does not have to belong to the original uniform grid. Hence the phonon frequencies for any wave vector can be found. The Fourier transforms are most efficiently calculated using fast Fourier Transform techniques

(FFT) [115]. The accuracy of the interpolated results will depend on the size of the uniform grid and can be checked by comparing the result of the interpolation against the full calculation of a wavevector not included in the grid. The smoother the phonon dispersions the fewer uniform grid points are need for the FFT.

In some metals the phonon dispersions are not smoothly varying with $\mathbf{q}$ due to the presence of Kohn anomalies. These are anomalous features of the phonon dispersion where there is a sudden change in the electronic screening of the lattice vibrations causing a dramatic reduction in the phonon frequencies. The occurrence of a Kohn anomaly is determined by the Fermi surface geometry. Only phonons with a wavevector $\mathbf{q}$ connecting two electronic states which both lie on the Fermi surface and are such that the tangents to the Fermi surface at these electronic states are parallel will lead to a Kohn anomaly [116]. As a result special care is needed when interpolating the dynmaical matrix near these points.

Chapter 3

Methods for Calculation of the Electron-Phonon Interaction and Anisotropic Eliashberg Theory

3.1 The Electron-Phonon Interaction

In the previous chapter I considered how to calculate properties related to electrons and the motion of the ions in a system. The coupling between these two is known as the electron-phonon (e-ph) interaction. It strongly influences a wide variety of physical phenomena in solids, such as the electron mass enhancement near the Fermi energy which is reflected in the specific heat [117]. Other examples of the physical manifestation of the e-ph interaction include electrical resistivity and superconductivity [118]. The latter will be discussed later in this chapter.

3.1.1 Beyond the Adiabatic Approximation

The time-independent Schrödinger equation for the coupled system of electrons and nuclei can be written as:

$$\hat{H}\Psi_s(\mathbf{r},\mathbf{R}) = E_s\Psi_s(\mathbf{r},\mathbf{R}), \tag{3.1}$$

where s is the state of the coupled system. The solutions to such an equation can be expressed as:

$$\Psi_s(\mathbf{r},\mathbf{R}) = \sum_i \chi_{si}(\mathbf{R})\Psi_i(\mathbf{r}:\mathbf{R}), \tag{3.2}$$

since $\Psi_i(\mathbf{r};\mathbf{R})$ defines a complete set of states for the electron at each set of nuclear coordinates. An eigenvalue problem for the ionic part can be found by inserting equation (3.2) into equation (3.1), multiplying the expression on the left by $\Psi^*_{i'}(\mathbf{r};\mathbf{R})$ and integrating over the electron variable $\mathbf{r}$:

$$\left[-\sum_I \frac{\nabla_I^2}{2M_I} + \frac{1}{2}\sum_{I\neq J}\frac{Z_I Z_J}{|\mathbf{R}_I-\mathbf{R}_J|} + E_i(\mathbf{R})\right]\chi_{si}(\mathbf{R}) + \sum_{i'} C_{ii'}\chi_{si'}(\mathbf{R}) = E_s\chi_{si}(\mathbf{R}), \tag{3.3}$$

where the matrix elements $C_{ii'} = A_{ii'} + B_{ii'}$, with

$$A_{ii'}(\mathbf{R}) = -\sum_I \frac{1}{M_I}\left\langle\Psi_i(\mathbf{r};\mathbf{R})\right|\nabla_I\left|\Psi_{i'}(\mathbf{r}:\mathbf{R})\right\rangle\nabla_I, \tag{3.4}$$

$$B_{ii'}(\mathbf{R}) = -\sum_I \frac{1}{2M_I}\left\langle\Psi_i(\mathbf{r};\mathbf{R})\right|\nabla_I^2\left|\Psi_{i'}(\mathbf{r}:\mathbf{R})\right\rangle. \tag{3.5}$$

For any operator $\hat{X}$ the notation $\left\langle\Psi_i(\mathbf{r};\mathbf{R})\right|\hat{X}\left|\Psi_{i'}(\mathbf{r};\mathbf{R})\right\rangle$ means integration over only the electronic variables $\mathbf{r}$.

In order to apply the adiabatic approximation, the off-diagonal elements of $C_{ii'}$ are ignored. This ensures that the electrons stay in their given states even as the

nuclei move. It can be shown that the diagonal terms $A_{ii} = 0$ when Ψ is normalised, and B_{ii} can be grouped with $E_i(\mathbf{R})$ to form $E_e(\mathbf{R})$. Thus equation (2.34) is recovered.

The non-diagonal matrix elements $C_{ii'}$ describe transitions from one electronic state to another due to the nuclei displacements, and are the origin of the electron-phonon interaction. It can be shown that $A_{ii'}$ is the dominant term and involves the gradient of the electronic wavefunctions with respect to nuclear positions and the gradient of the nuclear wavefunction χ [119]. A thorough derivation of the electron-phonon matrix elements can be found in the book by Grimvall [118]. Very briefly, the derivation described by Grimvall involves expanding the matrix elements using perturbation theory, after expressing the nuclear kinetic operator ∇ in terms of phonon creation and annihilation operators. The result is that the matrix element which scatters an electron from state $n\mathbf{k}$ to $m\mathbf{k}+\mathbf{q}$ while absorbing or emitting a phonon with phonon mode ν, momentum $\mathbf{q}$ and frequency ω can be written as:

$$g^{\nu}_{n\mathbf{k};m\mathbf{k}+\mathbf{q}} = \frac{1}{\sqrt{2m_0\omega_{\nu\mathbf{q}}}} \langle m\mathbf{k}+\mathbf{q}| \, \Delta V_{\nu\mathbf{q}} \, |n\mathbf{k}\rangle \,, \tag{3.6}$$

where m_0 is the mode-dependent reduced mass, and $\Delta V_{\nu\mathbf{q}}$ is the derivative of the self-consistent Kohn-Sham potential with respect to a collective ionic displacement corresponding to a phonon of momentum $\mathbf{q}$ and mode ν. Thus, detailed microscopic information about the e-ph coupling can be calculated with only the inputs of the unperturbed Kohn-Sham states and the screened potential $\Delta V_{\nu\mathbf{q}}$. $\Delta V_{\nu\mathbf{q}}$ can be described using DFPT as shown in equation (2.62). Therefore once a DFPT calculation has been carried out, all the information needed to calculate the e-ph matrix elements is available. The calculation of the matrix elements can then be achieved at little computational expense.

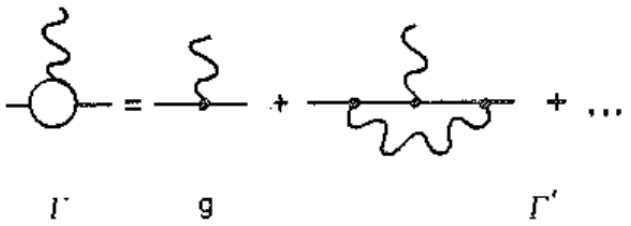


Figure 3.1: Contributions to the electron-phonon vertex function Γ. From [118].

Although the electron-phonon matrix elements are not directly measurable by experimental techniques, they are essential to the calculation of a variety of physical properties which arise from the coupling. These properties include the lifetimes of the phonons, which can be measured using inelastic neutron or x-ray scattering experiments [120–122], and the renormalisation of electronic quasiparticles due to e-ph coupling, which can be measured using angle-resolved photoemission spectroscopy (ARPES) [123]. It should be noted that these properties are calculated only in relation to the electron-phonon contribution, while in experiment there may be other effects such as lattice-defect scattering, electron-electron scattering etc.

3.1.2 Electron Self-Energy

In the many-body picture, the motion of the electrons is affected by the other electrons and by the phonons of the system. The electronic self-energy is thus defined by these interactions. Using a Green's function approach the electronic self-energy arising from the electron-phonon interaction can be expressed in terms of an infinite series of Feynman diagrams [118]. Fortunately, Migdal found that in many important cases only the lowest order of these diagrams need be taken into account [124]. This can be demonstrated by separating the electron-phonon vertex into the sum of the bare electron-phonon matrix elements g, and a vertex

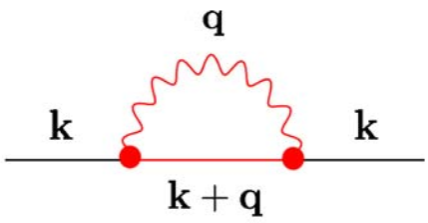


Figure 3.2: The electron self energy arising from the e-ph interaction in Migdal's approximation is given by this Feynman diagram. The black line represents an electron with momentum **k** and the wiggly red line represents a phonon which forms a loop connected by the bare e-ph vertices. From [125].

correction term Γ':

$$\Gamma = g + \Gamma'. \tag{3.7}$$

By applying the rules for Feynman diagrams to the lowest order contribution to the correction vertex term Γ' of Fig. (3.1) it can be demonstrated that:

$$\Gamma' \sim g\frac{\omega_D}{E_\mathrm{F}} \sim g\left(\frac{m}{M}\right)^{\frac{1}{2}} \sim 10^{-2}g, \tag{3.8}$$

where ω_D is the Debye frequency, E_F is the Fermi energy, and m the mass of a free electron. This justifies replacing the dressed e-ph vertex Γ by its bare counterpart g. The electron self-energy due to the e-ph interaction is therefore the Feynman diagram of Fig (3.2) and can be written as:

$$\Sigma = i\int \frac{d2}{(2\pi)^4}|g\,(1,2)\,|^2 D\,(1-2)\,G_0\,(2)\,, \tag{3.9}$$

where the dressed electron Green's function G has been replaced by the bare electron Green's function G_0 so that it is no longer dependent on Σ. This can be justified on the ground that the electronic self-energy due to the e-ph coupling is small on the scale of the Fermi energy [118]. The dressed phonon Green's function, D, does not cause any problems as the fully renormalised phonon frequencies

are easily obtained from DFPT. The quadrimomentum has the compressed notation $1 = (\mathbf{k}, \omega)$ where $\mathbf{k}$ is the wavevector and ω the energy. The expression for the electron self-energy can be integrated analytically and by considering the free propagators in terms of the non-interacting electronic energy $\epsilon_{n\mathbf{k}}$ (where n is the band index) and vibrational frequencies $\omega_{\mathbf{q}\nu}$. As a result, Σ can be expressed as:

$$\Sigma_{n\mathbf{k}} = \sum_{m\nu} \int_{\mathrm{BZ}} \frac{d\mathbf{q}}{\Omega_{\mathrm{BZ}}} |g^{\nu}_{mn}(\mathbf{k}, \mathbf{q})|^2 \left[\frac{\left[1 - f\left(\epsilon_{m\mathbf{k}+\mathbf{q}}\right)\right]\left[1 + n\left(\omega_{\mathbf{q}\nu}\right)\right] + f\left(\epsilon_{m\mathbf{k}+\mathbf{q}}\right) n\left(\omega_{\mathbf{q}\nu}\right)}{\epsilon_{n\mathbf{k}} - \epsilon_{m\mathbf{k}+\mathbf{q}} - \omega_{\mathbf{q}\nu} - i\eta} \right.$$
$$\left. + \frac{\left[1 - f\left(\epsilon_{m\mathbf{k}+\mathbf{q}}\right)\right] n\left(\omega_{\mathbf{q}\nu}\right) + f\left(\epsilon_{m\mathbf{k}+\mathbf{q}}\right)\left[1 + n\left(\omega_{\mathbf{q}\nu}\right)\right]}{\epsilon_{n\mathbf{k}} - \epsilon_{m\mathbf{k}+\mathbf{q}} + \omega_{\mathbf{q}\nu} - i\eta} \right]. \tag{3.10}$$

Here η is a smearing parameter, Ω_{BZ} is the volume of the Brillouin zone; the integration extends over the zone. The temperature dependence is contained within the occupation factors: $f(\epsilon_{n\mathbf{k}})$ is the Fermi-Dirac distribution, which provides the average number of fermions in a single state $n\mathbf{k}$ such that:

$$f(\epsilon_{n\mathbf{k}}) = \frac{1}{e^{(\epsilon_{n\mathbf{k}} - E_F)/K_{\mathrm{B}}T} + 1} \tag{3.11}$$

where E_F is the Fermi level, K_{B} the Boltzmann constant (which is set to 1 in atomic units) and T is the absolute temperature. $n(\omega_{\mathbf{q}\nu})$ is the Bose-Einstein occupation which gives the expected number of bosons for a particular state:

$$n(\omega_{\mathbf{q}\nu}) = \frac{1}{e^{\omega_{\mathbf{q}\nu}/K_{\mathrm{B}}T} - 1}. \tag{3.12}$$

The two terms in equation (3.10) represent two different scattering processes which arise from the e-ph interaction and contribute to the electronic self-energy. The first fraction in the equation for the electronic self-energy refers to the emission

of a phonon from an initial state with higher energy $\epsilon_{n\mathbf{k}}$ to one of lower energy $\epsilon_{m\mathbf{k+q}}$. The probability of the state $m\mathbf{k}+\mathbf{q}$ not being occupied is given by the first part of the first fraction, $1-f(\epsilon_{m\mathbf{k+q}})$, and $1+n(\omega_{\mathbf{q}\nu})$ is the temperature factor for stimulated emission of a phonon. The additional part of the emission term is many-body in character, and results from the fact that, if there is an electron in state $n\mathbf{k}$, the possibility of an electron in state $m\mathbf{k}+\mathbf{q}$ being scattered to the state $n\mathbf{k}$ must be excluded. The second fraction refers to the absorption of a phonon from an electron in state $\epsilon_{n\mathbf{k}}$ so that it increases its energy at $\epsilon_{m\mathbf{k+q}}$.

The real part of Σ defines the peak shift of the renormalised electronic quasi-particles when compared to the non-interacting electronic energies. These quasi-particles have a finite lifetime, which lead to a linewidth, $\Gamma_{n\mathbf{k}}$, and can be related to the imaginary part as:

$$\Gamma_{n\mathbf{k}} = -2\mathrm{Im}\Sigma_{\mathrm{n}\mathbf{k}}. \tag{3.13}$$

The imaginary part of the self-energy in equation (3.10) has the following simpler form:

$$\begin{aligned}\mathrm{Im}\Sigma_{n\mathbf{k}} = \sum_{m\nu}\int_{\mathrm{BZ}}\frac{d\mathbf{q}}{\Omega_{\mathrm{BZ}}}|g^{\nu}_{mn}(\mathbf{k},\mathbf{q})|^2\,[(1-f\left(\epsilon_{m\mathbf{k+q}}\right)+n\left(\omega_{\mathbf{q}\nu}\right))\,\delta\left(\epsilon_{n\mathbf{k}}-\epsilon_{m\mathbf{k+q}}-\omega_{\mathbf{q}\nu}\right)\\ +\left(f\left(\epsilon_{m\mathbf{k+q}}\right)+n\left(\omega_{\mathbf{q}\nu}\right)\right)\delta\left(\epsilon_{n\mathbf{k}}-\epsilon_{m\mathbf{k+q}}+\omega_{\mathbf{q}\nu}\right)].\end{aligned} \tag{3.14}$$

Direct comparison between theory and experiment can be made as these linewidths can be measured by ARPES experiments [126]. The direct information about renormalisation given by ARPES has been used to make theoretical predictions of the contribution to the photoemission kink made by phonon in high temperature superconductors [36]. Another link with experiments is that the electron-phonon

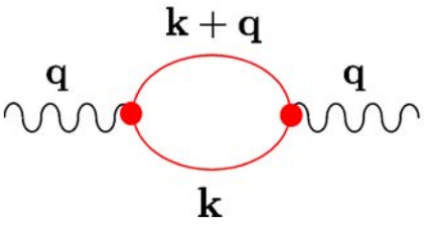


Figure 3.3: The lowest order Feynman diagram for the phonon self-energy arising from the e-ph interaction. The phonon with momentum **q** is represented by the black wiggly line and the red electron lines form a Fermion loop which is connected by the bare e-ph vertices. From [125].

coupling parameter, λ, also known as the mass enhancement factor, which measures how strong the e-ph interaction is in a material, is related to the gradient of the real part of Σ at the Fermi energy. Therefore, this parameter can be extracted from the renormalised band structures produced by ARPES measurements:

$$\lambda_{n\mathbf{k}} = -\frac{\partial \mathrm{Re}\Sigma(\mathrm{n}, \mathbf{k}, \epsilon)}{\partial \epsilon}. \tag{3.15}$$

3.1.3 Phonon Self-Energy

The phonons studied via DFPT do not interact with any other particles and therefore have infinite lifetimes. This is not the case in reality, as interactions with electrons result in renormalised quasiparticle properties: in a very similar manner to the electron self-energy, the phonon self-energy Π can be examined. The renormalisation of the phonons leads to a broadening of the linewidths. As for the electrons [eq. (3.13)], the linewidths of phonon peaks is inversely proportional to the lifetime of the excitation, and hence can be related to the imaginary part of Π. The peak shift due to the real part of Π is already included at the DFPT level and so doesn't need to be considered further.

As in Section 3.1.2 the Migdal approximation justifies considering only the

lowest order Feynman diagram for the electron-phonon contribution to the phonon self-energy. This is shown in Fig. (3.3) and can be expressed as an equation as [118]:

$$\Pi = -2i \int \frac{d1}{(2\pi)^4} |g\,(1,2)\,|^2 G_0\,(1)\,G_0\,(2)\,. \tag{3.16}$$

This equation can be integrated analytically, and by considering only the imaginary part it is found that:

$$\mathrm{Im}\Pi_{\mathbf{q}\nu} = -2\pi \sum_{mn} \int_{\mathrm{BZ}} \frac{d\mathbf{k}}{\Omega_{\mathrm{BZ}}} |g^{\nu}_{mn}(\mathbf{k},\mathbf{q})|^2 \frac{f_{n\mathbf{k}} - f_{m\mathbf{k}+\mathbf{q}}}{\epsilon_{n\mathbf{k}} - \epsilon_{m\mathbf{k}+\mathbf{q}} + \omega_{\mathbf{q}\nu} + i\delta \mathrm{sgn}(\omega)}. \tag{3.17}$$

The linewidths $\gamma_{\mathbf{q}\nu}$, which are accessible by experiments such as inelastic neutron or x-ray scattering, provide a measure of the coupling strength of a particular phonon mode and are just the negative of the imaginary part of the phonon self-energy, so that [127]:

$$\gamma_{\mathbf{q}\nu} = 2\pi \sum_{mn} \int_{\mathrm{BZ}} \frac{d\mathbf{k}}{\Omega_{\mathrm{BZ}}} |g^{\nu}_{mn}(\mathbf{k},\mathbf{q})|^2 (f_{n\mathbf{k}} - f_{m\mathbf{k}+\mathbf{q}}) \delta(\epsilon_{n\mathbf{k}} - \epsilon_{m\mathbf{k}+\mathbf{q}} + \omega_{\mathbf{q}\nu}). \tag{3.18}$$

A very common approximation to this expression for the phonon linewidth is to assume that the electronic structure of interest is smoothly varying on the scale of phonon energies. As the δ-function forces the difference in the energies $\epsilon_{n\mathbf{k}} - \epsilon_{m\mathbf{k}+\mathbf{q}}$ to be very small, the difference in the Fermi-Dirac occupations can be approximated as

$$f_{n\mathbf{k}} - f_{m\mathbf{k}+\mathbf{q}} \approx f'(\epsilon_{n\mathbf{k}})(\epsilon_{n\mathbf{k}} - \epsilon_{m\mathbf{k}+\mathbf{q}}) = -f'(\epsilon_{n\mathbf{k}})\omega_{\mathbf{q}\nu}, \tag{3.19}$$

where $f' = \partial f/\partial\epsilon$. For low temperatures the energy derivative of the Fermi-Dirac distributions has a strong peak near E_F. This means that it can be replaced by a

delta function $f'(\epsilon_{n\mathbf{k}}) \rightarrow -\delta(\epsilon_{n\mathbf{k}})$. The phonon frequencies are ignored in the delta functions, to leave:

$$\gamma_{\mathbf{q}\nu} = 2\pi\omega_{\mathbf{q}\nu} \sum_{mn,\mathbf{k}} w_{\mathbf{k}} |g^{\nu}_{mn}(\mathbf{k},\mathbf{q})|^2 \delta(\epsilon_{n\mathbf{k}}) \delta(\epsilon_{m\mathbf{k}+\mathbf{q}}), \tag{3.20}$$

where $w_{\mathbf{k}}$ are the weights of the $\mathbf{k}$-points in the Brillouin zone. This expression is positive definite and is commonly used for first-principles calculations. It is referred to as the "double-delta function" approximation and is only valid when $T \rightarrow 0$. It will also break down in the long wavelength limit $\mathbf{q} \rightarrow 0$, because intraband scattering events involve very small energy differences and so it is no longer appropriate to neglect the phonon frequency in the delta functions.

The electron-phonon coupling strength associated with a specific phonon mode and wavevector $\lambda_{\mathbf{q}\nu}$ can be calculated as:

$$\lambda_{\mathbf{q}\nu} = \frac{1}{N_F \omega_{\mathbf{q}\nu}} \sum_{mn,\mathbf{k}} w_{\mathbf{k}} |g^{\nu}_{mn}(\mathbf{k},\mathbf{q})|^2 \delta(\epsilon_{n\mathbf{k}}) \delta(\epsilon_{m\mathbf{k}+\mathbf{q}}), \tag{3.21}$$

where N_F is the density of states at the Fermi level. The coupling strength of a particular phonon mode and wavevector can therefore be related to the phonon linewidth in the double-delta approximation by:

$$\lambda_{\mathbf{q}\nu} = \frac{1}{\pi N_F} \frac{\gamma_{\mathbf{q}\nu}}{\omega^2_{\mathbf{q}\nu}}. \tag{3.22}$$

This is typically how first-principles calculations of the electron-phonon coupling strength based on DFPT are done, by calculating first the phonon linewidths, $\gamma_{\mathbf{q}\nu}$, and then summing over the whole phonon spectrum to produce a total electron-

phonon coupling λ:

$$\lambda = \sum_{\mathbf{q}\nu} w_{\mathbf{q}} \lambda_{\mathbf{q}\nu}, \tag{3.23}$$

where the $w_{\mathbf{q}}$ are the Brillouin zone weights associated with the phonon wavevector $\mathbf{q}$ and are normalised to 1. Values of λ are typically in the range $0-2$, where a total e-ph coupling strength larger than 1 characterises strong coupling [128].

For many applications, rather than being interested in scattering from a point in momentum space, $\mathbf{k}$, to another, $\mathbf{k}+\mathbf{q}$, it is instead of interest to calculate the scattering from a state $\mathbf{k}$ with energy $\epsilon_{n\mathbf{k}}$ to all possible final states with energy $\epsilon_{n\mathbf{k}} \pm \omega$ irrespective of their momentum. This is the purpose of the Eliashberg spectral function $\alpha^2F(\omega, \mathbf{k})$. It can be considered as a product of an effective electron-phonon coupling α^2 and the phonon density of states $F(\omega)$, hence the notation. The function gives the coupling between an initial state on the Fermi surface and all other states on the Fermi surface which differ energetically from the initial state by a phonon energy:

$$\alpha^2F(\mathbf{k}, \mathbf{k}', \omega) = N_{\mathrm{F}} \sum_{\nu} |g_{\mathbf{k}\mathbf{k}'\nu}|^2 \delta(\omega - \omega_{\mathbf{k}-\mathbf{k}',\nu}). \tag{3.24}$$

It is dimensionless, and can be constructed from the phonon linewidths of individual modes at each phonon wavevector, to give, in its isotropic form,

$$\alpha^2F(\omega) = -\frac{1}{\pi N_F} \sum_{\nu} \int_{\mathrm{BZ}} \frac{d\mathbf{q}}{\Omega_{\mathrm{BZ}}} \frac{\gamma_{\mathbf{q}\nu}}{\omega_{\mathbf{q}\nu}} \delta(\omega - \omega_{\mathbf{q}\nu}). \tag{3.25}$$

Finally the mass enhancement parameter is related to the isotropic Eliashberg spectral function as follows:

$$\lambda = 2 \int_0^{\infty} d\omega \omega^{-1} \alpha^2F(\omega). \tag{3.26}$$

3.2 Electron-Phonon Coupling with Wannier Functions

It can be seen that calculation of the phonon self-energy which arises due to the electron-phonon interaction requires a summation over electronic transitions where both the initial and final state must be very close to the Fermi level, such that $\epsilon_{m\mathbf{k_q}} = \epsilon_{n\mathbf{k}} + \omega_{\mathbf{q}\nu}$. As a result, in order to calculate the phonon linewidth one must determine the initial and final electronic states, the phonon frequencies of interest, and the associated e-ph matrix elements with fine energy and momentum resolution. The required momentum grids are much finer than the ones used in a DFPT cycle, and while additional Kohn-Sham states can be calculated relatively cheaply on dense **k**-grids, the calculation of $\Delta V_{\mathbf{q}\nu}$ on a suitably fine **q**-grid is incredibly time consuming. The challenging Brillouin zone integrals also apply to the calculations of the electronic self-energy, the Eliashberg spectral function and the mass enhancement parameter. In order to overcome this challenge, Wannier interpolation techniques have been developed, so that e-ph matrix elements can be calculated to very high accuracy for very fine momentum grids at affordable computational cost [125, 129–132]. This allows the possibility of numerical convergence of the Brillouin zone integrals by considering a large number of wavevectors, which may be of the order of thousands to millions. These techniques have been implemented in the Electron-Phonon with Wannier functions (`EPW`) code, allowing previously unpractical calculation of properties related to the electron-phonon interaction [130].

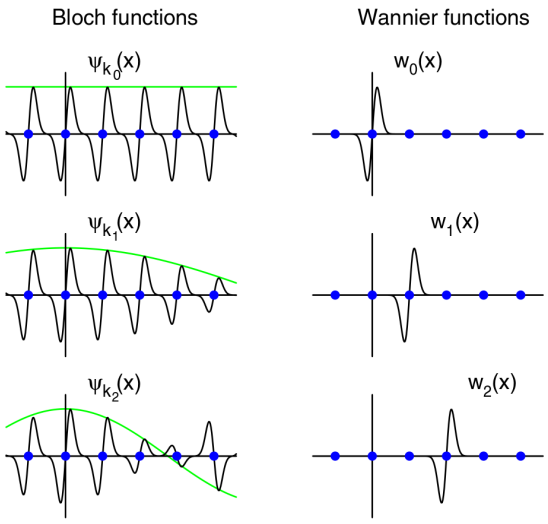


Figure 3.4: A comparison of Bloch functions and Wannier functions in 1D for a single band for three different wavevectors. The blue circles represent lattice vectors and the green lines indicate the e^{ikx} envelopes of each Bloch function. From [132].

3.2.1 Maximally Localised Wannier Functions

In density functional theory calculations using periodic boundary conditions, it is common for the Kohn-Sham orbitals to be represented as Bloch functions, $|\phi_{n\mathbf{k}}\rangle$:

$$\phi_{n\mathbf{k}}(\mathbf{r}) = u_{n\mathbf{k}}(\mathbf{r})e^{i\mathbf{k}\cdot\mathbf{r}}, \tag{3.27}$$

where $u_{n\mathbf{k}}(\mathbf{r})$ displays the periodicity of the lattice. However, alternative representations exist, such as Wannier functions [133]. Rather than being localised in energy, these functions are localised in space at a lattice vector $\mathbf{R}$, Fig. 3.4. A unitary transformation between Bloch and Wannier functions can be expressed as [134]:

$$w_{n\mathbf{R_e}}(\mathbf{r}) = \frac{\Omega}{(2\pi)^3}\int_{\mathrm{BZ}} d\mathbf{k}e^{-i\mathbf{k}\cdot\mathbf{R_e}}\sum_m U^{\mathbf{k}}_{mn}\phi_{n\mathbf{k}}(\mathbf{r}), \tag{3.28}$$

where $w_{n\mathbf{R_e}}(\mathbf{r})$ is the Wannier function associated with the lattice vector $\mathbf{R_e}$, Ω is the volume of the unit cell, and $U^{\mathbf{k}}_{mn}$ is a unitary matrix which defines the gauge.

As Bloch states are only uniquely defined up to a phase factor, all Wannier functions are nonunique. Thus, there are many possibilities for the choice of the unitary rotation $U_{mn}^{\mathbf{k}}$. The most widely used method for choosing $U_{mn}^{\mathbf{k}}$ is to find the unitary transformation which corresponds to the maximally localised Wannier functions (MLWFs). This is achieved by defining a localisation functional which measures the quadratic spreads of the Wannier functions around their centres [134]. By expressing this functional in terms of the Bloch functions and minimising with respect to $U_{mn}^{\mathbf{k}}$, the maximally localised Wannier functions can be found. In practice, for sensible initial guesses, the `wannier90` code produces the matrix $U_{mn}^{\mathbf{k}}$ which yields maximally localised Wannier functions from Bloch eigenstates [131].

3.2.2 Wannier Interpolation of the Electron-Phonon Interaction

Fig. 3.5 depicts schematically a general Wannier interpolation technique as used in the `EPW` code [132]. The quantity of interest $f(\mathbf{q})$, for example the electron-phonon matrix elements, are first calculated by first-principles for a coarse uniform grid. They are then Fourier transformed from the Bloch representation into the Wannier representation, $F(\mathbf{R})$. Due to the spatial localisation of these maximally localised Wannier functions, $F(\mathbf{R})$ decays rapidly with $|\mathbf{R}|$, and can be truncated outside of a real space supercell containing $N_{\mathbf{q}}$ unit cells, where $N_{\mathbf{q}}$ corresponds to the number of grid points in the coarse Brillouin zone mesh. By performing an inverse transformation the quantity f can be accurately interpolated back to the Bloch representation for an arbitrary point $\mathbf{k}$ in reciprocal space. This allows for the calculation of the quantity $f(k)$ on a fine grid in the Brillouin zone. As the Fourier transformations are very fast, the computational cost is comparable to that of the

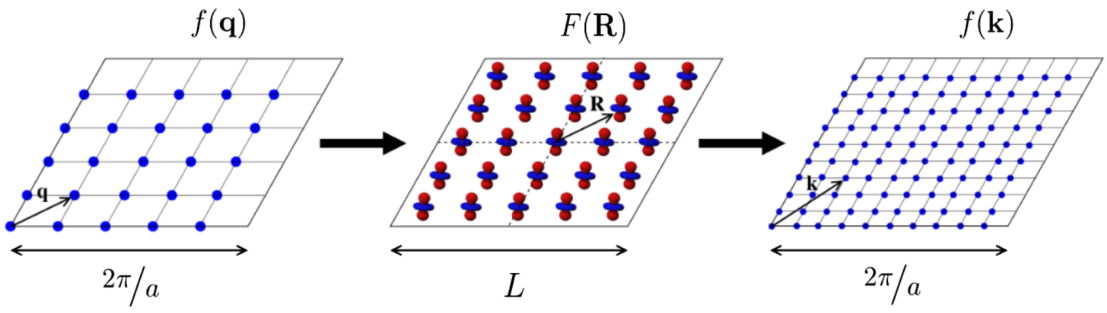


Figure 3.5: The Wannier interpolation technique represented schematically. Initially the quantity of interest f is calculated for a coarse mesh $\mathbf{q}$ via first-principles methods (left panel). Upon transformation to the Wannier representation, the quantity $F(\mathbf{R})$ is strongly localised near the origin of the equivalent supercell (middle panel). The inverse transformation allows for the quantity of interest to be evaluated on a very fine grid at low computational cost (right panel). From [132].

initial coarse grid first-principles calculation.

In the case of the `EPW` code, the quantities that need to undergo Wannier interpolation are the electronic Hamiltonian, the phonon dynamical matrix and the electron-phonon matrix elements. The electronic Hamiltonian can be obtained in the MLWF representation as [125]:

$$H^{\mathrm{el}}_{\mathbf{R_e},\mathbf{R'_e}} = \sum_{\mathbf{k}} w_{\mathbf{k}} e^{-i\mathbf{k}\cdot(\mathbf{R'_e}-\mathbf{R_e})} U^{\dagger}_{\mathbf{k}} H^{\mathrm{el}}_{\mathbf{k}} U_{\mathbf{k}}, \tag{3.29}$$

where the weights $w_{\mathbf{k}}$ are normalised to 1 and the electron band indices have been omitted for clarity. The dynamical matrix can likewise be transformed into a localised real-space representation by [125]:

$$D^{\mathrm{ph}}_{\mathbf{R_p},\mathbf{R'_p}} = \sum_{\mathbf{q}} w_{\mathbf{q}} e^{-i\mathbf{q}\cdot(\mathbf{R'_p}-\mathbf{R_p})} e_{\mathbf{q}} D^{\mathrm{ph}}_{\mathbf{q}} e^{\dagger}_{\mathbf{q}}, \tag{3.30}$$

where $e_{\mathbf{q}}$ are the orthonormal eigenvectors of the dynamical matrix; the phonon mode indices have been omitted for clarity. The electron-phonon vertex in the

joint electron-phonon Wannier representation is given by [125]:

$$g(\mathbf{R_e}, \mathbf{R_p}) = \frac{1}{N_p} \sum_{\mathbf{k},\mathbf{q}} w_{\mathbf{k}} w_{\mathbf{q}} e^{-i(\mathbf{k}\cdot\mathbf{R_e}+\mathbf{q}\cdot\mathbf{R_p})} U^{\dagger}_{\mathbf{k}+\mathbf{q}} g(\mathbf{k}, \mathbf{q}) U_{\mathbf{k}} u^{-1}_{\mathbf{q}}, \tag{3.31}$$

where $u_{\mathbf{q}}$ are the phonon eigenvectors scaled by the atomic masses. A detailed derivation of Eqs. (3.29), (3.30), and (3.31) and a discussion of their validity can be found in Ref. [125].

The electronic Hamiltonian, phonon dynamical matrix and electron-phonon matrix elements can then be Fourier transformed back to the Bloch representation for a dense mesh of electron and phonon wavevectors by inverting Eqs. (3.29), (3.30), and (3.31). These quantities on the fine grid can then be used to accurately calculate the physical quantities, such as the the phonon self-energy due to the e-ph coupling, described in Section 3.1.3.

3.3 Superconductivity

3.3.1 BCS Theory

The most important feature of the BCS theory is Cooper-pair condensation: pairs of electrons with opposite momentum and opposite spins $(k\uparrow, -k\downarrow)$ are occupied in a coherent manner. The number of Cooper-pairs becomes non-zero only when the temperature is below T_c. A simple Hamiltonian which allows this behaviour is known as the BCS reduced Hamiltonian:

$$H = \sum_{k\sigma} \epsilon_k c^{\dagger}_{k\sigma} c_{k\sigma} - \sum_{kk'} V_{k'k} (c^{\dagger}_{-k'\downarrow} c^{\dagger}_{k'\uparrow})(c_{k\uparrow} c_{-k\downarrow}), \tag{3.32}$$

where the operator $c_{k\sigma}$ ($c^{\dagger}_{k\sigma}$) destroys (creates) an electron in a Bloch state $k\sigma$, with k a combined band and momentum index (short for $n\mathbf{k}$), and σ the spin of the electron ($\uparrow$ denotes spin up and $\downarrow$ spin down). $V_{k'k}$ is a pairing interaction where a positive $V_{k'k}$ corresponds to an attractive interaction. The BCS equations can be derived with the help of Gor'kov's Green's functions [135]. In this method the operators $c_{k\sigma}$ can be written in the Heisenberg picture with time t replaced by an imaginary time $-i\tau$:

$$c_{k\sigma}(\tau) = e^{H\tau} c_{k\sigma} e^{-H\tau}. \tag{3.33}$$

The Green's function can then be written in concise notation:

$$G(k,\tau) = -\langle T_\tau c_{k\sigma}(\tau) c^{\dagger}_{k\sigma}(0)\rangle, \tag{3.34}$$

where the braces indicate that this is a grand canonical average and T_τ is the Wick operator. This reorders the operators to ensure that τ increases from right to left. The Green's function is periodic in imaginary time and so can be expressed in the Fourier representation as [136]:

$$G(k,\tau) = T\sum_{i\omega_n} e^{-i\omega_n\tau} G(k, i\omega_n), \tag{3.35}$$

where the fermion Matsubara frequencies are given by $i\omega_n = (2n+1)\pi T$. In order to study the superconducting state the Green's function $G(k, i\omega_n)$ must be determined. This can be obtained by inverting the previous equation so that

$$G(k, i\omega_n) = \frac{1}{2}\int_{-\beta}^{\beta} d\tau e^{i\omega_n\tau} G(k,\tau), \tag{3.36}$$

where $\beta = 1/T$. To evaluate $G(k, i\omega_n)$ the τ derivative of $G(k,\tau)$ is taken after combining equations (3.32), (3.33), and (3.34) [137]:

$$\left(-\frac{d}{d\tau} - \epsilon_k\right) G(k,\tau) = \delta(\tau) - \sum_{k'} V_{kk'} \langle T_\tau c^\dagger_{-k\downarrow}(\tau) c_{k'\uparrow}(\tau) c_{-k'\downarrow}(\tau) c^\dagger_{k\uparrow}(0)\rangle. \quad (3.37)$$

The right hand side of this equation contains a complicated thermal average of four operators, and can be simplified using a mean-field argument. If fluctuations $\langle AB\rangle - \langle A\rangle\langle B\rangle$ are unimportant, then averages like $\langle c^\dagger_1 c^\dagger_2 c_3 c_4\rangle$ can be approximated by $\langle c^\dagger_1 c_4\rangle\langle c^\dagger_2 c_3\rangle - \langle c^\dagger_1 c_3\rangle\langle c^\dagger_2 c_4\rangle$ [138]. In order to include non-zero Cooper-pair amplitudes $\langle c_{k\uparrow} c_{-k\downarrow}\rangle$, the following replacement is made:

$$\langle T_\tau c^\dagger_{-k\downarrow}(\tau) c_{k'\uparrow}(\tau) c_{-k'\downarrow}(\tau) c^\dagger_{k\uparrow}(0)\rangle \to \langle T_\tau c_{k'\uparrow}(\tau) c_{-k'\downarrow}(\tau)\rangle \langle T_\tau c^\dagger_{-k\downarrow}(\tau) c^\dagger_{k\uparrow}(\tau)\rangle. \quad (3.38)$$

Equation (3.37) then becomes

$$\left(-\frac{d}{d\tau} - \epsilon_k\right) G(k,\tau) = \delta(\tau) - \sum_{k'} V_{kk'} F(k',0) \bar{F}(k,\tau), \quad (3.39)$$

where the Gor'kov anomalous Green's functions have been introduced:

$$F(k,\tau) = -\langle T_\tau c_{k\uparrow}(\tau) c_{-k\downarrow}(0)\rangle, \quad (3.40)$$

$$\bar{F}(k,\tau) = -\langle T_\tau c^\dagger_{-k\downarrow}(\tau) c^\dagger_{k\uparrow}(0)\rangle. \quad (3.41)$$

$\bar{F}$ and F are complex conjugates of each other $\bar{F}(k,\tau) = F(k,\tau)^*$. Similarly to the Green's function, an equation of motion for $\bar{F}(k,\tau)$ can be established:

$$\left(-\frac{d}{d\tau} + \epsilon_k\right) \bar{F}(k,\tau) = -\sum_{k'} V_{kk'} \bar{F}(k',0) G(k,\tau). \quad (3.42)$$

Equations (3.39) and (3.42) form a pair of coupled nonlinear differential equations, the solutions of which yield the BCS theory. This can be achieved by defining the BCS energy gap as:

$$\Delta_k = \sum_{k'} V_{kk'} F(k', 0), \tag{3.43}$$

and using the Fourier transform of equations (3.39) and (3.42) as defined in equation (3.36). This gives the following matrix equation:

$$\begin{pmatrix} i\omega_n - \epsilon_k & \Delta_k \\ \Delta_k^* & i\omega_n + \epsilon_k \end{pmatrix} \begin{pmatrix} G(k, i\omega_n) \\ \bar{F}(k, i\omega_n) \end{pmatrix} = \begin{pmatrix} 1 \\ 0 \end{pmatrix} \tag{3.44}$$

By inverting equation (3.44), an expression for the Gor'kov Green's function can be found:

$$G = (-i\omega_n - \epsilon_k)/(\omega_n^2 + E_k^2), \tag{3.45}$$

$$\bar{F} = \Delta_k^*/(\omega_n^2 + E_k^2). \tag{3.46}$$

where the quasiparticle energy E_k in the superconducting state is given by:

$$E_k^2 = \epsilon_k^2 + |\Delta_k|^2. \tag{3.47}$$

In the normal state the energy gap Δ_k disappears, and the normal state Green's functions are found. Finally, a self-consistent formula for the energy gap can be calculated using the Fourier representation of equation (3.36):

$$\Delta_k = T \sum_{k'} \sum_{i\omega_n} \frac{V_{kk'} \Delta_{k'}}{\omega^2 + E_k^2}. \tag{3.48}$$

This BCS gap equation is more usually written in the equivalent form:

$$\Delta_k = \sum_{k'} \frac{V_{kk'}\Delta_{k'}}{2E_{k'}} \tanh\left(\frac{E_{k'}}{2T}\right). \tag{3.49}$$

In the BCS model the attractive potential $V_{kk'}$ vanishes unless both initial and final states lie within the Debye energy ω_D of the Fermi energy:

$$V_{kk'} \approx V\delta(\omega_D - |\epsilon_k|)\delta(\omega_D - |\epsilon_{k'}|). \tag{3.50}$$

It is assumed that the density of states is constant within a Debye energy of the Fermi level, and so by using this potential in the BCS gap equation it is found that:

$$\frac{1}{\lambda} = \int_0^{\omega_D} \frac{\tanh(E/2T)}{E} dE, \tag{3.51}$$

where $\lambda = VN_F$. When $T = 0$ K this integral can be performed analytically to give:

$$\Delta = 2\omega_D \frac{e^{(-1/\lambda)}}{1 - e^{(-1/\lambda)}}. \tag{3.52}$$

With these approximations, the famous BCS formula for the critical transition temperature can be expressed as:

$$T_c = 1.13\omega_D \exp(-1/\lambda). \tag{3.53}$$

This suggests that the critical temperature depends on a materials properties such as the phonon spectrum, the electronic structure near the Fermi level, and the pairing potential, which arises from the net balance between the attractive e-ph coupling and the repulsive electron-electron interaction. It is therefore perhaps surprising that in the limit of weak coupling, the BCS equations leads to universal

material-independent relations such as

$$\frac{2\Delta}{T_c} = 3.53. \tag{3.54}$$

Deviations from similar universal relations contributed to the need to improve upon BCS theory and its underlying approximations, which do not take into account the details of the electron-phonon physics. For example, in deriving equation (3.37) the term describing the self-energy of the electron has been ignored. This is perfectly valid in the case of weak superconductors. However for cases where λ is large, the superconducting state significantly alters the electronic properties near the Fermi surface, and causes a change to the self-energy term which cannot be neglected. The extension of the BCS model to strong coupling is provided by the Eliashberg theory [139].

3.3.2 Eliashberg Theory

Very accurate descriptions of the superconducting state in conventional superconductors can be achieved using the Migdal-Eliashberg theory [124, 139]. This is a Green's function approach which extends the remit of BCS to describe strong-coupling materials. Unlike the BCS theory which models a non-local, instantaneous interaction, the Eliashberg theory is local in space and retarded in time to more properly reflect the time-delay in the lattice overscreening. A key strength of the Eliashberg theory is that only normal state properties enter, and these can be obtained via the first principles approaches to electron-phonon coupling already discussed in this chapter.

In 1960 Nambu developed a condensed notation which allows for treatment of both the normal state and superconducting state on an equal footing [140]. In

Nambu's notation a two-component field operator is introduced:

$$\mathbf{\Psi_k} = \begin{pmatrix} c_{\mathbf{k}\uparrow} \\ c^{\dagger}_{-\mathbf{k}\downarrow} \end{pmatrix}, \tag{3.55}$$

together with a generalised 2×2 matrix Green's function:

$$\hat{G}(\mathbf{k},\tau) = -\langle T_\tau \mathbf{\Psi_k}(\tau)\mathbf{\Psi}^{\dagger}_{\mathbf{k}}(0)\rangle \tag{3.56}$$

$$= -\begin{bmatrix} \langle T_\tau c_{\mathbf{k}\uparrow}(\tau)c^{\dagger}_{\mathbf{k}\uparrow}(0)\rangle & \langle T_\tau c_{\mathbf{k}\uparrow}(\tau)c_{-\mathbf{k}\downarrow}(0)\rangle \\ \langle T_\tau c^{\dagger}_{-\mathbf{k}\downarrow}(\tau)c^{\dagger}_{\mathbf{k}\uparrow}(0)\rangle & \langle T_\tau c^{\dagger}_{-\mathbf{k}\downarrow}(\tau)c_{-\mathbf{k}\downarrow}(0)\rangle \end{bmatrix}. \tag{3.57}$$

The diagonal elements of this matrix are the normal propagators G. The upper right and lowest left elements, off-diagonal elements, are the Gor'kov anomalous Green's functions F and $\bar{F}$, respectively. These elements have non-zero values only when the material is in the superconducting state. For non-interacting band structures the off-diagonal elements vanish, and the normal-state Green's function for the electrons can be written in the form

$$\hat{G}_0^{-1}(\mathbf{k}, i\omega_n) = i\omega_n\hat{\tau}_0 - \epsilon_{\mathbf{k}}\hat{\tau}_3, \tag{3.58}$$

where the Pauli matrices have been used. These are defined as:

$$\hat{\tau}_0 = \begin{pmatrix} 1 & 0 \\ 0 & 1 \end{pmatrix}, \qquad \hat{\tau}_1 = \begin{pmatrix} 0 & 1 \\ 1 & 0 \end{pmatrix},$$

$$\hat{\tau}_2 = \begin{pmatrix} 0 & -i \\ i & 0 \end{pmatrix}, \qquad \hat{\tau}_3 = \begin{pmatrix} 1 & 0 \\ 0 & -1 \end{pmatrix}. \tag{3.59}$$

In the same way as in the normal state, the generalised Green's function can be determined from the electronic self-energy associated with the pairing interaction $\hat{\Sigma}(\mathbf{k}, i\omega_n)$ using a matrix Dyson's equation:

$$\hat{G}^{-1}(\mathbf{k}, i\omega_n) = \hat{G}_0^{-1}(\mathbf{k}, i\omega_n) - \hat{\Sigma}(\mathbf{k}, i\omega_n). \tag{3.60}$$

The electron pairing in a conventional superconductor arises from a delicate interplay between the repulsive Coulomb interaction and the attractive e-ph interaction. For this reason both a Coulomb contribution $\hat{\Sigma}_{\mathrm{c}}(\mathbf{k}, i\omega_n)$ and an electron-phonon contribution $\hat{\Sigma}_{\mathrm{ep}}(\mathbf{k}, i\omega_n)$ to the electronic self-energy must be considered within Eliashberg theory. $\hat{\Sigma}(\mathbf{k}, i\omega_n) = \hat{\Sigma}_{\mathrm{ep}}(\mathbf{k}, i\omega_n) + \hat{\Sigma}_{\mathrm{c}}(\mathbf{k}, i\omega_n)$, where:

$$\hat{\Sigma}_{\mathrm{ep}}(\mathbf{k}, i\omega_n) = -T \sum_{\mathbf{k}'n'} \hat{\tau}_3 \hat{G}(\mathbf{k}', i\omega_{n'}) \hat{\tau}_3 \sum_{\lambda} |g_{\mathbf{k}\mathbf{k}'\nu}|^2 D_\nu(\mathbf{k} - \mathbf{k}', i\omega_n - i\omega_{n'}), \tag{3.61}$$

$$\hat{\Sigma}_{\mathrm{c}}(\mathbf{k}, i\omega_n) = -T \sum_{\mathbf{k}'n'} \hat{\tau}_3 \hat{G}^{\mathrm{od}}(\mathbf{k}', i\omega_{n'}) \hat{\tau}_3 V(\mathbf{k} - \mathbf{k}'). \tag{3.62}$$

These self-energies correspond to only the lowest order Feynman diagrams, i.e. Migdal's theorem. $\hat{G}^{\mathrm{od}}$ refers to only the off-diagonal elements of the Green's function. The reason for this is so that the Coulomb effects already included in $\hat{G}_0(\mathbf{k}, i\omega_n)$ are not double counted in the self-energy. It can be seen that equations (3.9) and (3.61) are energetically equivalent, provided that we write the dressed Green's function for the phonons as:

$$D_\nu(\mathbf{q}, i\omega_n) = \frac{2\omega_{\mathbf{q}\nu}}{(i\omega_n)^2 - \omega_{\mathbf{q}\nu}^2}. \tag{3.63}$$

The electronic self-energy itself is a 2×2 matrix, and so can be decomposed into a linear combination of Pauli matrices. Typically this is done in terms of

the three scalar functions known as the mass renormalisation factor $Z(\mathbf{k}, i\omega_n)$, the energy shift $\chi(\mathbf{k}, i\omega_n)$, and the order parameter $\phi(\mathbf{k}, i\omega_n)$:

$$\hat{\Sigma}(\mathbf{k}, i\omega_n) = i\omega_n \left[1 - Z(\mathbf{k}, i\omega_n)\right] \hat{\tau}_0 + \chi(\mathbf{k}, i\omega_n)\hat{\tau}_3 + \phi(\mathbf{k}, i\omega_n)\hat{\tau}_1 + \overline{\phi}(\mathbf{k}, i\omega_n)\hat{\tau}_2. \quad (3.64)$$

By substituting equations (3.64) and (3.58) into the electronic Dyson equation (3.60) $\hat{G}^{-1}(\mathbf{k}, i\omega_n)$ can be written as

$$\hat{G}^{-1}(\mathbf{k}, i\omega_n) = i\omega_n Z\hat{\tau}_0 - (\epsilon_k + \chi)\hat{\tau}_3 - \phi\hat{\tau}_1 - \overline{\phi}\hat{\tau}_2. \quad (3.65)$$

At this point we note that $\overline{\phi}(\mathbf{k}, i\omega_n)$ and $\phi(\mathbf{k}, i\omega_n)$ are equal except for a phase factor. This is chosen to be zero, which allows the the $\overline{\phi}(\mathbf{k}, i\omega_n)$ term to be omitted in Eq. (3.65). By inverting this matrix the the Green's function can be obtained:

$$\hat{G}(\mathbf{k}, i\omega_n) = -\left\{i\omega_n Z(\mathbf{k}, i\omega_n)\hat{\tau}_0 + \left[\epsilon_{\mathbf{k}} + \chi(\mathbf{k}, i\omega_n)\right]\hat{\tau}_3 + \phi(\mathbf{k}, i\omega_n)\hat{\tau}_1\right\} / \Theta(\mathbf{k}, i\omega_n), \quad (3.66)$$

where the denominator is defined as:

$$\Theta(\mathbf{k}, i\omega_n) = \left[\omega_n Z(\mathbf{k}, i\omega_n)\right]^2 + \left[\epsilon_{\mathbf{k}} + \chi(\mathbf{k}, i\omega_n)\right]^2 + \left[\phi(\mathbf{k}, i\omega_n)\right]^2. \quad (3.67)$$

Finally, the anisotropic Eliashberg gap equations can be derived by taking this explicit expression for the Green's function and inserting it into the expressions for the electronic self-energy in the Migdal approximation found in equations (3.61) and (3.62):

$$Z(\mathbf{k}, i\omega_n) = 1 + \frac{T}{\omega_n N_{\mathrm{F}}} \sum_{\mathbf{k}'n'} \frac{\omega_{n'} Z(\mathbf{k}', i\omega_{n'})}{\Theta(\mathbf{k}', i\omega_{n'})} \lambda(\mathbf{k}, \mathbf{k}', n - n'), \quad (3.68)$$

$$\chi(\mathbf{k}, i\omega_n) = -\frac{T}{N_\mathrm{F}} \sum_{\mathbf{k}'n'} \frac{\epsilon_{\mathbf{k}'} + \chi(\mathbf{k}', i\omega_{n'})}{\Theta(\mathbf{k}', i\omega_{n'})} \lambda(\mathbf{k}, \mathbf{k}', n - n'), \tag{3.69}$$

$$\phi(\mathbf{k}, i\omega_n) = \frac{T}{N_\mathrm{F}} \sum_{\mathbf{k}'n'} \frac{\phi(\mathbf{k}', i\omega_{n'})}{\Theta(\mathbf{k}', i\omega_{n'})} \times \left[\lambda(\mathbf{k}, \mathbf{k}', n - n') - N_\mathrm{F} V(\mathbf{k} - \mathbf{k}')\right], \tag{3.70}$$

where the definition of the anisotropic electron-phonon coupling constant has been used

$$\lambda(\mathbf{k}, \mathbf{k}', n - n') = \int_0^\infty d\omega \frac{2\omega}{(\omega_n - \omega_{n'})^2 + \omega^2} \alpha^2 F(\mathbf{k}, \mathbf{k}', \omega). \tag{3.71}$$

The superconducting gap is defined as the order parameter divided by the mass renormalisation function,

$$\Delta(\mathbf{k}, i\omega_n) = \frac{\phi(\mathbf{k}, i\omega_n)}{Z(\mathbf{k}, i\omega_n)}. \tag{3.72}$$

By self-consistently solving the anisotropic Eliashberg gap equations, this superconducting gap can be calculated for each temperature. It can be seen that $\phi = 0$ is a trivial solution for all temperatures. This corresponds to the normal state of the material. However, if a solution with $\phi \neq 0$ exists then it can be shown that it has a lower free energy and so describes a state with Cooper-pair condensation [141]. The T_c is thus defined as the highest temperature at which a nontrivial solution for the order parameter exists.

3.3.3 Practical Calculations

In order to solve the anisotropic Eliashberg equations, a few approximations must be made. Firstly it can be seen that the superconducting pairing occurs mainly within a characteristic phonon energy of the Fermi surface. Therefore, only electron bands near the Fermi energy need be considered. This can be achieved by inserting the unity relation $\int_{-\infty}^{\infty} d\epsilon' \delta(\epsilon_{\mathbf{k}'} - \epsilon') = 1$ on the right-hand side in Eqs. (3.68)-(3.70).

In this region we can approximate the density of states as being constant and set it to the value at the Fermi level N_F. The energies ϵ' can also be set to the Fermi energy, as it is assumed that any variation takes place on a larger energy scale. This is not the case for the numerator of equation (3.69) or $\Theta(\mathbf{k}', i\omega_{n'})$, which both vary rapidly. These two quantities can be integrated analytically. From these approximations it follows that the energy shift $\chi(\mathbf{k}, i\omega_n) = 0$. This leaves two coupled nonlinear equations which need solving at each temperature, one for the renormalisation function and one for the order parameter. From equation (3.72), it can be seen that the latter is equivalent to the product of the superconducting gap and the renormalisation function. Therefore these self-consistent equations are written as:

$$Z(\mathbf{k}, i\omega_n) = 1 + \frac{\pi T}{\omega_n} \sum_{\mathbf{k}'n'} W_{\mathbf{k}'} \frac{\omega_{n'}}{\sqrt{R(\mathbf{k}', i\omega_{n'})}} \lambda(\mathbf{k}, \mathbf{k}', n-n'), \tag{3.73}$$

$$Z(\mathbf{k}, i\omega_n)\Delta(\mathbf{k}, i\omega_n) = \pi T \sum_{\mathbf{k}'n'} W_{\mathbf{k}'} \frac{\Delta(\mathbf{k}', i\omega_{n'})}{\sqrt{R(\mathbf{k}', i\omega_{n'})}} \times \left[\lambda(\mathbf{k}, \mathbf{k}', n-n') - N_{\mathrm{F}} V(\mathbf{k}-\mathbf{k}')\right], \tag{3.74}$$

where $R(\mathbf{k}, i\omega_n) = \omega_n^2 + \Delta^2(\mathbf{k}, i\omega_n)$ and $W_{\mathbf{k}} = \delta(\epsilon_{\mathbf{k}})/N_{\mathrm{F}}$.

These equations involve a summation over an infinite set of Matsubara frequencies, which must be truncated in practical calculations. There are two methods for doing this. One is to set the sum of the frequencies to a given cutoff energy ω_c, which is usually set at ten times the largest phonon energy. This will mean that, as the number of Matsubara frequencies depends on the temperature being solved for, different temperatures are solved with different numbers of frequencies. As a result, calculations become more expensive computationally as $T \to 0$. An alternative method is to set the number of Matsubara frequencies to a fixed number which satisfies or exceeds the cutoff energy at all temperatures, and allows for equal

computational expense at each temperature of interest. The main disadvantage of this scheme is that a variable cutoff is required.

Including the Coulomb interaction in the Eliashberg equations is more difficult, as it does not have a natural cutoff to ensure it convergences over Matsubara frequencies. The time scale of the interaction is much shorter than the e-ph coupling, and so is typically dealt with by use of the Morel-Anderson pseudopotential

$$\mu_{\mathrm{c}}^{*} = \frac{\mu_{\mathrm{c}}}{1 + \mu_{\mathrm{c}} \ln(\epsilon_F/\omega_{\mathrm{c}})}, \tag{3.75}$$

where μ_c is a dimensionless parameter describing the double Fermi surface average of the matrix element of the screened Coulomb interaction times the density of states at the Fermi level:

$$\mu_{\mathrm{c}} = N_{\mathrm{F}} \langle \langle V(\mathbf{k} - \mathbf{k}') \rangle \rangle_{\mathrm{FS}}. \tag{3.76}$$

In practice μ_{c} replaces the $N_{\mathrm{F}} V(\mathbf{k} - \mathbf{k}')$ term in equation (3.74), and is set as a material dependent parameter. This dimensionless parameter is usually in the range $0.05 - 0.2$.

3.3.4 Superconducting Gap on the Real Frequency Axis

As described in the previous section, it is computationally efficient to calculate the Eliashberg gap equations on the imaginary axis using Matsubara frequencies. However most spectral properties, such as the quasiparticle density of states, can only be obtained from real-axis formulation of the Eliashberg equations. Rather than calculating the superconducting gap along the real axis, which is extremely demanding numerically, the real axis solutions can be found by analytic continua-

tion from the imaginary axis [142,143]. This can be achieved either by an iterative process or by use of Padé approximants [144–147]. In general, Padé approximants are much less demanding computationally, but they are also less accurate, as they may miss some fine features of the superconducting gap. In order to calculate the N-point Padé approximant to a complex function $u(z)$ of the complex variable z, whose N values $u_i = u_i(z_i)(i = 1, ..., N)$ are given at N complex points z_i, the continued fraction is defined as:

$$C_N(z) = \cfrac{a_1}{1 + \cfrac{a_2(z - z_1)}{1 + \cfrac{a_3(z - z_2)}{\ddots + \cfrac{a_n(z - z_{n-1})}{1}}}} \tag{3.77}$$

where the coefficients a_i are to be determined so that $C_N(z_i) = u_i$, where $i = 1, ..., N$ [144]. The coefficients are given by the recursive formula $a_i = g_i(z_i)$, where

$$g_1(z_i) = u_i \quad \text{with} \quad i = 1, ..., N \tag{3.78}$$

$$g_p(z_i) = \frac{g_{p-1}(z_{p-1}) - g_{p-1}(z)}{(z - z_{p-1})g_{p-1}(z)} \quad \text{for} \quad p \geq 2. \tag{3.79}$$

The continued fraction can then be evaluated order-by-order using $C_N(z) = A_N(z)/B_N(z)$ where A_N and B_N are polynomials given by the recursion relation

$$A_{n+1}(z) = A_n(z) + (z - z_n)a_{n+1}A_{n-1}(z) \quad \text{with} \quad n = 1, ..., N - 1 \tag{3.80}$$

$$B_{n+1}(z) = B_n(z) + (z - z_n)a_{n+1}B_{n-1}(z) \quad \text{with} \quad n = 1, ..., N - 1 \tag{3.81}$$

with $A_0 = 0$, $A_1 = a_1$, and $B_0 = B_1 = 1$.

Alternatively, the exact iterative analytic continuation involves solving the two self-consistent equations:

$$\begin{aligned} Z(\mathbf{k},\omega) &= 1+i\frac{\pi T}{\omega}\sum_{\mathbf{k}'n'} W_{\mathbf{k}'}\frac{\omega_{n'}}{\sqrt{R(\mathbf{k}',i\omega_{n'})}}\lambda(\mathbf{k},\mathbf{k}',\omega-i\omega_{n'}) \\ &+ i\frac{\pi}{\omega}\int_{-\infty}^{\infty}d\omega'\Gamma(\omega,\omega')\sum_{\mathbf{k}'} W_{\mathbf{k}'}\alpha^2F(\mathbf{k},\mathbf{k}',\omega')\frac{(\omega-\omega')Z(\mathbf{k}',\omega-\omega')}{\sqrt{Z^2(\mathbf{k}',\omega-\omega')R(\mathbf{k}',\omega-\omega')}}, \end{aligned} \tag{3.82}$$

$$\begin{aligned} Z(\mathbf{k},\omega)\Delta(\mathbf{k},\omega) &= \pi T\sum_{\mathbf{k}'n'} W_{\mathbf{k}'}\left[\lambda(\mathbf{k},\mathbf{k}',\omega-i\omega_{n'})-\mu_{\rm c}^*\right]\frac{\Delta(\mathbf{k}',i\omega_{n'})}{\sqrt{R(\mathbf{k}',i\omega_{n'})}} \\ &+ i\pi\int_{-\infty}^{\infty}d\omega'\Gamma(\omega,\omega')\sum_{\mathbf{k}'} W_{\mathbf{k}'}\alpha^2F(\mathbf{k},\mathbf{k}',\omega')\frac{Z(\mathbf{k}',\omega-\omega')\Delta(\mathbf{k}',\omega-\omega')}{\sqrt{Z^2(\mathbf{k}',\omega-\omega')R(\mathbf{k}',\omega-\omega')}}, \end{aligned} \tag{3.83}$$

where

$$\Gamma(\omega,\omega') = \frac{1}{2}\left(\tanh\frac{\omega-\omega'}{2T}+\coth\frac{\omega'}{2T}\right), \tag{3.84}$$

$$\lambda(\mathbf{k},\mathbf{k}',\omega-i\omega_n) = -\int_{-\infty}^{\infty}d\omega'\frac{\alpha^2F(\mathbf{k},\mathbf{k}',\omega')}{\omega-i\omega_n-\omega'}, \tag{3.85}$$

$$\alpha^2F(\mathbf{k},\mathbf{k}',-\omega) = -\alpha^2F(\mathbf{k},\mathbf{k}',\omega). \tag{3.86}$$

Once the superconducting gap $\Delta(\mathbf{k},\omega)$ and the mass renormalisation function $Z(\mathbf{k},\omega)$ are obtained on the real axis, the quasiparticle energies, $E_{\mathbf{k}}$, can thus be found as the poles of the electron Green's function in the superconducting state:

$$E_{\mathbf{k}}^2 = \left[\frac{\epsilon_{\mathbf{k}}}{Z(\mathbf{k},E_{\mathbf{k}})}\right]^2+\Delta^2(\mathbf{k},E_{\mathbf{k}}). \tag{3.87}$$

As the the anisotropic Eliashberg gap equations are very computationally de-

manding to solve, it is sometimes useful, as a first approximation, to solve the isotropic versions. The isotropic Eliashberg gap equations can be obtained by averaging **k** over the Fermi surface in Eqs. (3.73),(3.74). This results in the following isotropic expressions for the mass renormalisation and superconducting gap:

$$Z(i\omega_n) = 1 + \frac{\pi T}{\omega_n} \sum_{n'} \frac{\omega_{n'}}{\sqrt{R(i\omega_{n'})}} \lambda(n-n'), \tag{3.88}$$

$$Z(i\omega_n)\Delta(i\omega_n) = \pi T \sum_{n'} \frac{\Delta(i\omega_{n'})}{\sqrt{R(i\omega_{n'})}} \left[\lambda(n-n') - \mu_{\rm c}^*\right], \tag{3.89}$$

where $R(i\omega_n) = \omega_n^2 + \Delta^2(i\omega_n)$, and $\lambda(n-n') = \int_0^\infty d\omega \frac{2\omega\alpha^2F(\omega)}{(\omega_n-\omega_{n'})^2+\omega^2}$. By averaging **k** over the Fermi surface in Eqs. (3.83),(3.84), the isotropic Eliashberg superconducting gap on the real axis $\Delta(\omega)$ can be found. This is needed to calculate the normalised quasiparticle density of states in the superconducting state:

$$\frac{N_S(\omega)}{N_F} = \mathrm{Re}\left[\frac{\omega}{\sqrt{\omega^2 - \Delta^2(\omega)}}\right]. \tag{3.90}$$

This density of states is exactly what is measured in tunnelling experiments, and can be used to determine the Eliashberg spectral function experimentally [148].

Chapter 4

The Electron-Phonon Interaction in Doped Monolayer MoS_2

4.1 Introduction

In the last decade the discovery of graphene, a planar sheet of carbon atoms arranged in a hexagonal lattice, has stimulated a tremendous amount of research activity due to its rich physics and high mobility [149–154]. As a two-dimensional material, it is more attractive for use in next-generation nanoelectronic devices because, compared to one-dimensional materials such as carbon nanotubes, fabrication of the devices is relatively easy [43]. However, one major disadvantage of graphene in developing novel field effect transistors with a high on-off ratio is the lack of band gap in the monolayer. Thus, much effort has been undertaken in order to modify graphene to open up a gap. Various different avenues have been pursued including quantum confinement in nanoribbons [155], surface functionalisation [156], applying an electric field in the bilayer [157], deposition of graphene onto boron nitride substrates [158, 159], and B or N substitutional dop-

ing [160]. Unfortunately, the experimental realisation of a band gap larger than 400 meV remains a challenge and causes a deterioration in the high mobility that makes graphene so appealing in the first place [161]. An alternative strategy in the search for materials for next-generation electronic devices, is therefore to fabricate atomically thin sheets of materials with a finite band gap.

It has been recently demonstrated that other layered compounds such as MoS_2, WS_2, BN, etc. can be produced by scotch tape-based micromechanical exfoliation [46], liquid exfoliation techniques [55], as well as direct growth methods [162]. Of particular interest is the new family of 2D materials, the monolayers of semiconducting transition metal dichalcogenides (MX_2) [54, 163]. The most well-studied of these is single-layer molybdenum disulphide (MoS_2), which has a large band gap, making it very well-suited for potential low-power applications [164]. Monolayer MoS_2 has also been noted for its chemical sensing and photovoltaic properties [165, 166]. Recently a single-layer MoS_2 field effect transistor (FET) has been successfully fabricated [43]. It exhibits an on-off ratio of $\sim 10^8$ and an electron mobility of ~ 200 cm^2/Vs which is comparable to silicon based devices but is less thick then even the thinnest silicon films fabricated to date [43, 167, 168]. While much progress has been made in fabrication and transport measurements, much less is known about the intrinsic carrier mobility [169, 170]. In a FET, the carrier mobility is limited by scattering from phonons, and the maximum current is controlled by hot phonons [167]. Both of these issues depend upon the electron-phonon coupling, and so it is this consideration which motivates the work done in this chapter.

The chapter is organised as follows: first the electronic structure and lattice dynamics of bulk MoS_2 is investigated. The same is then done for the monolayer and the two are compared. Next the electron-phonon interaction in n-type single-

layer MoS_2 is studied, with particular attention paid to the considerations in a calculation using the `EPW` code, such as the choice of maximally localised Wannier functions and the convergence of the Brillouin zone integrals. The e-ph coupling in n-type monolayer MoS_2 is further investigated using a jellium model for the electron doping. The importance of the lattice parameters is examined. Finally, the phonon linewidths for electron doped monolayer MoS_2 are studied.

4.2 Bulk MoS_2

Bulk MoS_2 is a well-known transition metal dichalcogenide which has been of interest for its tribological, catalytic, and photovoltaic properties [171–174]. It has two different stable structures which are the 3R-MoS_2 polytype and 2H-MoS_2 [175]. The latter is of interest in this thesis as it is this layered material from which monolayer MoS_2 can be produced. 2H-MoS_2 crystallises in a hexagonal structure with space group $P6_3/mmc$ that consists of S-Mo-S trilayers that are weakly bonded by van der Waals forces. Each unit cell contains two formula units, as seen in Fig. 4.1. Each layer consists of a Mo plane sandwiched by two S planes with the same 2D hexagonal lattice as in graphene. However, unlike in multi-layer graphene, the two layers in the unit cell are displaced so that the Mo atoms of one layer lie above the S atoms in the next layer. The first task was to determine the equilibrium geometry for bulk MoS_2, that is, the lattice constants that yield a zero-stress tensor, and the atomic positions within the unit cell which lead to zero forces. This was carried out using density functional theory as implemented in the `Quantum ESPRESSO` package [176]. The exchange-correlation energy was approximated with the local density approximation as parametrised by Perdew and Zunger [98]. Norm-conserving Troullier-Martins pseudopotentials for Mo and

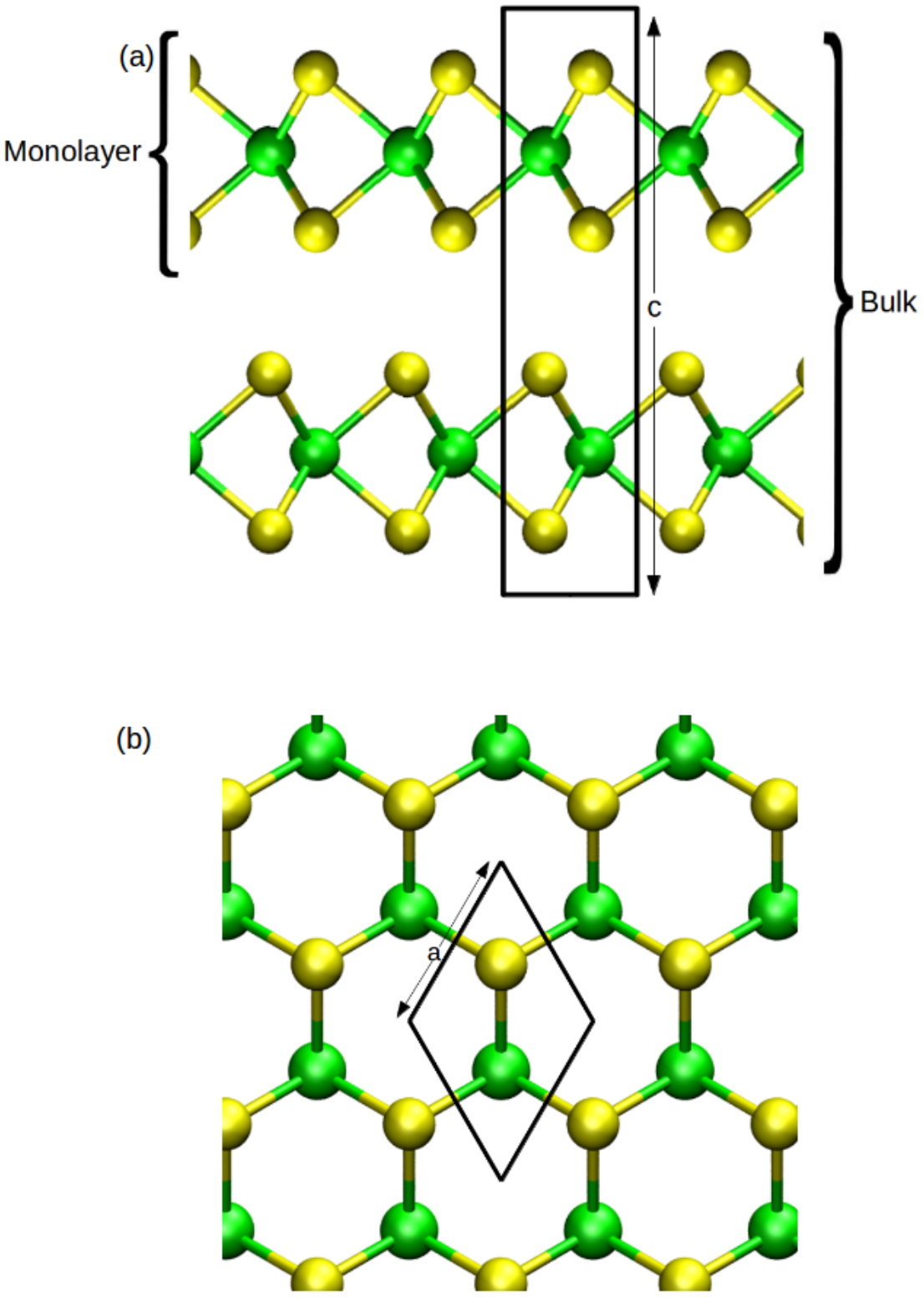


Figure 4.1: Ball and stick representation of MoS_2 showing both the bulk and monolayer. (a) The side view showing the unit cell and lattice parameter c for the bulk. The Mo atoms are shown in green and the S in yellow. (b) The top-view showing the a lattice parameter.

	1H-MoS_2	2H-MoS_2	
	a (Å)	a (Å)	c (Å)
This work	3.132	3.134	12.03
Experiment [180]	-	3.15	12.3
Ref. [181]	3.125	3.127	12.066

Table 4.1: A comparison of the lattice parameters for both bulk and monolayer MoS_2. It can be seen that the calculated values described in this chapter are in good agreement with both experiment and other DFT calculations.

S were generated using the Fritz-Haber code [177,178]. A nonlinear core correction was included for Mo, to take into account the interacting charge densities of the core and valence electrons without having to include additional semi-core electrons [179]. By converging both the total energy and the electronic eigenvalues with respect to the plane wave energy cutoff, a value of 80 Ry was determined as sufficient for accurate results. A similar convergence analysis was conducted for the sampling of the Brillouin zone which resulted in a Monkhorst-Pack **k**-point of $8 \times 8 \times 3$. The convergence threshold for the self-consistent total energy of the system was chosen as 10^{-8} Ry between two steps. The cell geometry was considered optimum when the Hellmann-Feynman forces acting on each atom were less than 10 meV/Å and the pressure in the unit cell was less than 0.5 kbar.

The optimised lattice parameters are summarised in Table 4.1. It can be seen that they are in good agreement with both experimental values and values obtained from other DFT calculations. As it is known that the LDA overestimates the strength of covalent bonds, it is not surprising that the in-plane lattice constant a is slightly underestimated in comparison to the experiment by 0.6% [180]. More remarkable is the fact that the c parameter is in such good agreement, an underestimation of 2.2%, as the LDA does not take into account the van der Waals forces which form the main part of the interlayer interaction. It is possible that a better

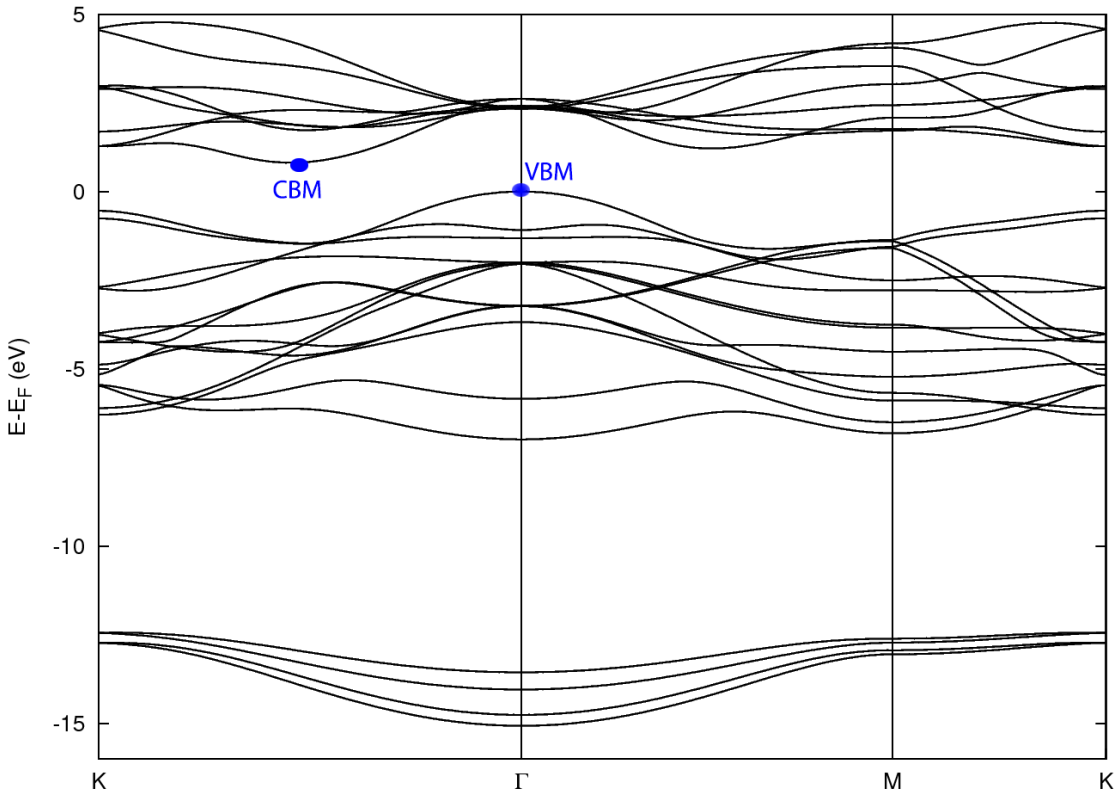


Figure 4.2: The calculated band structure of bulk MoS_2. $E = 0$ is set to the valence band maximum, which is at the zone centre and marked in blue. The conduction band minimum is found approximately halfway between Γ and K and is also marked in blue.

c parameter could be obtained by properly describing the van der Waals interaction either by use of dedicated nonlocal functionals, or treatments based on the random phase approximation. However, as the LDA has been demonstrated to produce good results for the calculation of lattice dynamics in similar layered materials such as BN and graphite, it was decided that such complications were unnecessary for this thesis [182, 183]. It is known that GGA considerably overestimates the lattice parameter for both the a and c axis and so was not considered [184].

4.2.1 Electronic structure

The electronic band structure for 2H-MoS_2 has been calculated along a high symmetry path through **k**-space, K-Γ-M-K. These points all lie in the plane so as to make the comparison with the monolayer easier. The maximum of the valence band is found at the Γ point, while the conduction band minimum is between K and Γ. The indirect band gap is calculated as 0.82 eV, which is in good agreement with other DFT-LDA calculations (0.7-0.77 eV) [185, 186]. In comparison to the experimental band gap of 1.23 eV, this calculation vastly underestimates the gap [187]. This is a well-known problem with DFT calculations of band gaps, and can be addressed more accurately by using alternative methods, such as hybrid functionals or the GW approximation [188].

4.2.2 Phonons

Next the phonon dispersions of 2H-MoS_2 were calculated using DFPT. The dynamical matrices were calculated for the 10 irreducible Brillouin zone points from a **q**-point grid of $8 \times 8 \times 1$. The phonon frequencies along the high symmetry path K-Γ-M-K were then found by Fourier interpolation. Fig. 4.3 shows the calculated phonon dispersions, with a comparison made to the results reported by Wakabayashi *et al.* obtained by neutron scattering [180]. Due to the limitations of the experiment only 12 phonon modes were found along Γ-M. Although the experimental measurements have an error bar of ±5%, it can be seen that there is generally a good agreement between the calculated and experimental phonon dispersions. This justifies the choice of describing the exchange-correction energy with the LDA, even if it is not properly describing the interlayer interaction. As expected the calculation, which contains 6 atoms in the unit cell, finds 18 phonon

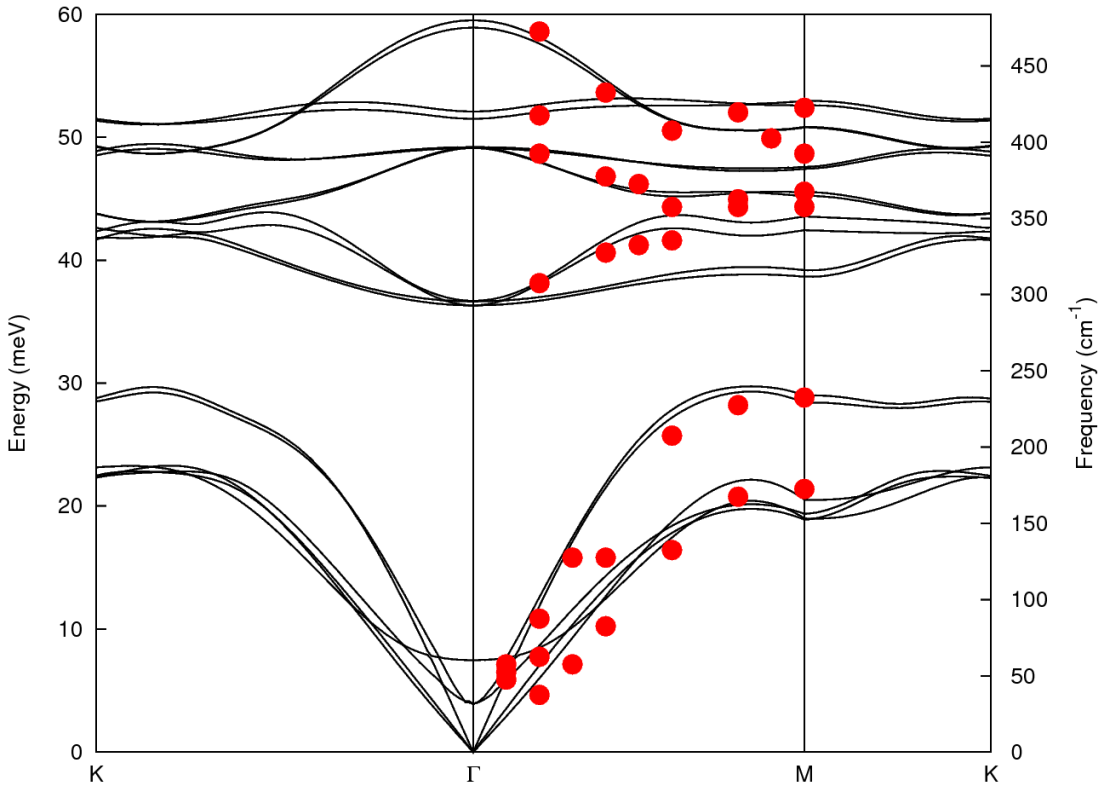


Figure 4.3: Phonon dispersion curve for 2H-MoS_2. The red points correspond to neutron scattering data extracted from Ref. [180].

modes. Due to degeneracies at the Γ point, this is reduced to 10 nondegenerate optical modes. It can be shown from an analysis of the D_{6h} symmetry that these modes can be decomposed into the irreducible representations:

$$\Gamma_{\text{optical}} = 2E_{2g} + 2B_{2g} + E_{2u} + E_{1g} + E_{1u} + B_{1u} + A_{1g} + A_{2u}. \tag{4.1}$$

The E_{1u} and A_{2u} modes are infrared active, that is, they create a dipole moment in the system [189]. The A_{1g}, E_{1g}, and E_{2g} phonon modes are Raman-active, meaning that they induce a polarisation or quadrupole moment in the material. The in-plane longitudinal acoustic (LA) and transverse acoustic (TA) modes have higher energy than the out of plane acoustic (ZA) mode.

				Frequency (cm^{-1})		
D_{6h}	Character	Direction	Atoms	This work	Exp. [189–191]	DFT [181]
A_{2u}	Acoustic	Out of plane	Mo + S	0	0	0
E^2_{2g}	Raman	In plane	Mo + S	31.7	32	35.2
B^2_{2g}	Inactive	Out of plane	Mo + S	60.2	-	55.7
E_{2u}	Inactive	In plane	S	292.8	-	287.1
E_{1g}	Raman	In plane	S	294.8	286	288.7
E^1_{2g}	Raman	In plane	Mo + S	396.5	383	387.8
E_{1u}	Infrared	In plane	Mo + S	396.9	384	391.2
B_{1u}	Inactive	Out of plane	S	414.6	-	407.8
A_{1g}	Raman	Out of plane	S	417.1	408	412.0
A_{2u}	Infrared	Out of plane	Mo + S	475.9	470	469.4
B^1_{2g}	Inactive	Out of plane	Mo + S	479.5	-	473.2

Table 4.2: Phonon symmetry representations of bulk MoS_2 (point group D_{6h}). The direction out of plane is parallel to the c axis and the one in plane is perpendicular to this axis. Experimental and DFT phonon frequencies from other groups are included for comparison. It can be seen that there is a good agreement.

One striking feature of the 2H-MoS_2 phonon dispersion is that the low-frequency optical modes are very similar in frequencies to the ZA modes, and are in fact of lower frequency than the LA and TA branches, for all $\mathbf{q}$ except near the Γ point. At Γ these low-frequency optical modes, which correspond to a rigid layer shear and vertical motion, are found at 4.6 meV and 7.5 meV respectively, which is in good agreement with other DFT calculations [181]. There is a gap of 8 meV separating the high-frequency optical modes from the low-frequency branches.

4.3 Monolayer MoS_2

Recent advances in the synthesis of two dimensional materials has lead to keen interest in monolayer MoS_2, which is often referred to as 1H-MoS_2 [46, 55, 162]. For calculations of the monolayer an $8 \times 8 \times 1$ $\mathbf{k}$-point grid was deemed to be sufficient. As periodic boundary conditions are being used, a unit cell with a large

vacuum in the z axis must be included to avoid spurious interactions between periodic images. A vacuum region of ∼15 Å separating layers was found to be large enough to achieve this goal. All other calculation details were identical to the bulk calculations.

The optimised lattice parameter a was determined to be 3.132 Å, in excellent agreement with other theoretical studies [192]. This is also nearly identical to the a lattice parameter in 2H-MoS_2, which is not surprising given the weak interlayer bonding. The main structural difference between bulk and single-layer MoS_2 is the lack of inversion symmetry. This is true of all MoS_2 systems with an odd number of layers, for example trilayer MoS_2, whereas the bilayer and other systems with an even number of layers retain the symmetry of the bulk system. The symmetry space group for the monolayer is P6m2 (point group D_{3h}) and Fig 4.1 shows the structure in comparison to the bulk.

4.3.1 Electronic Structure

The electronic band structure and density of states of single-layer MoS_2 are shown in Fig. 4.4. It is very similar to 2H-MoS_2 but with only half the number of bands. The most interesting differences involve the band gap edges. The valence band maximum (VBM) is now at the K point, which is 6 meV higher in energy than at the zone centre. The conduction band minimum (CBM) has also changed compared to the bulk, as it is at the K point. This means that 1H-MoS_2 is a direct gap semiconductor rather than indirect as found in multilayer MoS_2. The calculated direct gap of 1.81 eV is in excellent agreement with the experimentally obtained optical gap of 1.80 eV [49]. In fact this agreement must be a fortuitous coincidence because, as previously mentioned, the LDA is not suitable for accurate calculation of non ground state properties such as band gaps. It is also worth noting that the

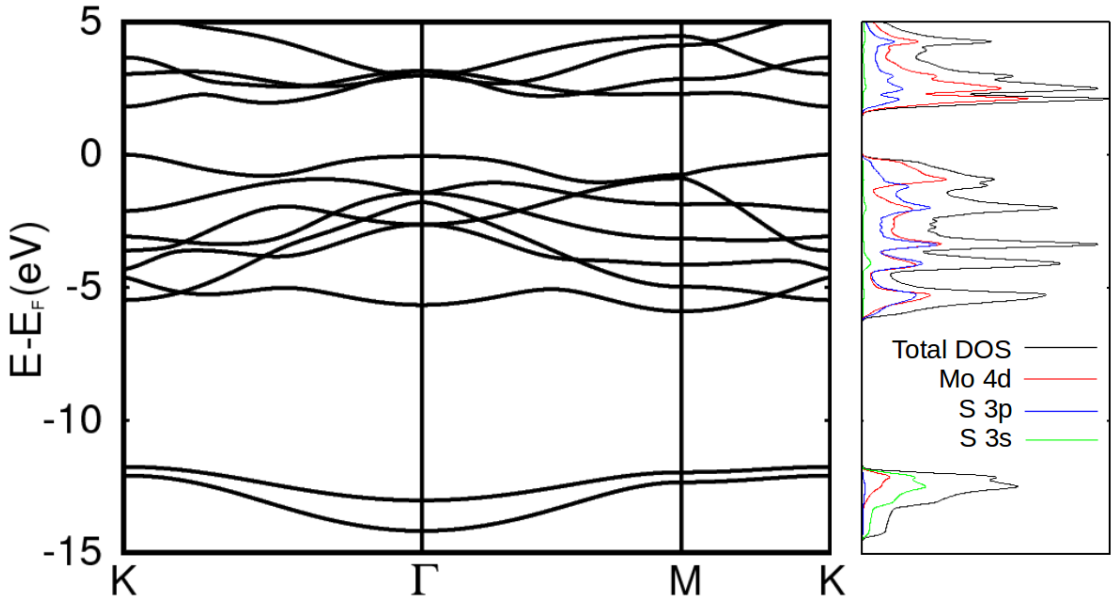


Figure 4.4: The electronic band structure and projected density of states of monolayer MoS_2. $E = 0$ is set to the top of the valence band. It can be seen that there is a direct band gap at the K point.

calculated value corresponds to the fundamental gap, which is always larger than the optical gap due to the neglect of the exitonic binding energy.

Interestingly it is found that the calculated direct K-K gap in bulk MoS_2 is identical to that of the monolayer at 1.81 eV. There is, however, a large difference in the indirect Γ-Q gap, as in the monolayer it is 2.01 eV compared to just 0.82 eV in the bulk. The density of states and partial density of states were calculated for 1H-MoS_2 as shown in Fig. 4.4. For this a $250\times250\times1$ **k**-point grid with 0.1 eV smearing was used. The electronic structure of monolayer MoS_2 can be thought of as three distinct regions of bands. The first are the deep lying states between 12 eV and 15 eV below the VBM which are separated from any other bands by a gap of ∼6 eV. These are mainly due to the sulphur 3*s* orbitals. The region of bands from 6 eV below the VBM to the band edge are mainly derived from Mo 4*d* and S 3*p* orbitals. It was found that there is a strong hybridisation between these

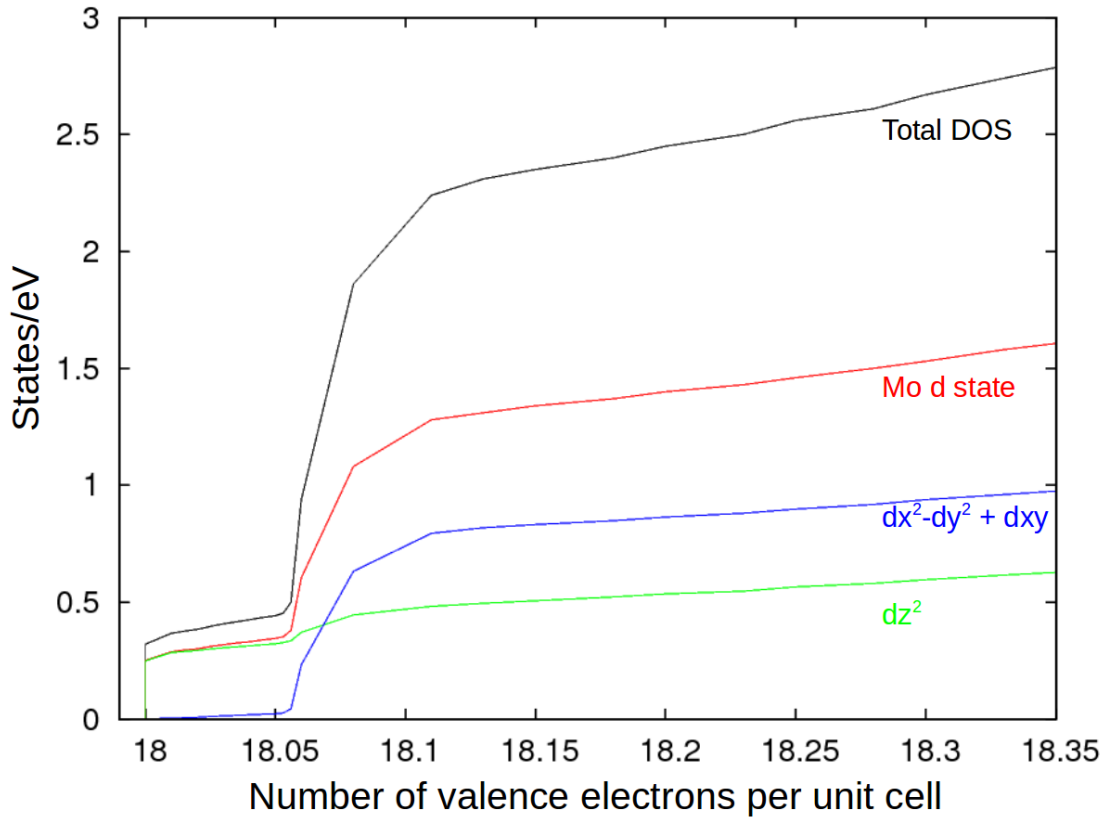


Figure 4.5: The projected density of states at the bottom of the conduction band for 1H-MoS_2. Any additional electrons will mainly fill the $4d$ state of Mo.

states. The final region of interest are the conduction bands between the CBM and approximately 5 eV above the VBM. These again are predominately Mo $4d$ and S $3p$ in character. There is then a gap in the conduction band between these bands and the higher energy bands dominated by Mo $5s$ states. This is useful for the creation of the maximally localised Wannier functions, as it means that disentanglement procedures are not needed. This will be explained in more detail later in this chapter. It was determined that the band edges, in agreement with other DFT studies, are mainly Mo d orbitals [167]. Specifically, the VBM around K is mainly of Mo d_{xy} character, and the bottom of the conduction band at K is strongly of Mo d_{z^2} character. This can be seen in more detail in Fig. 4.5.

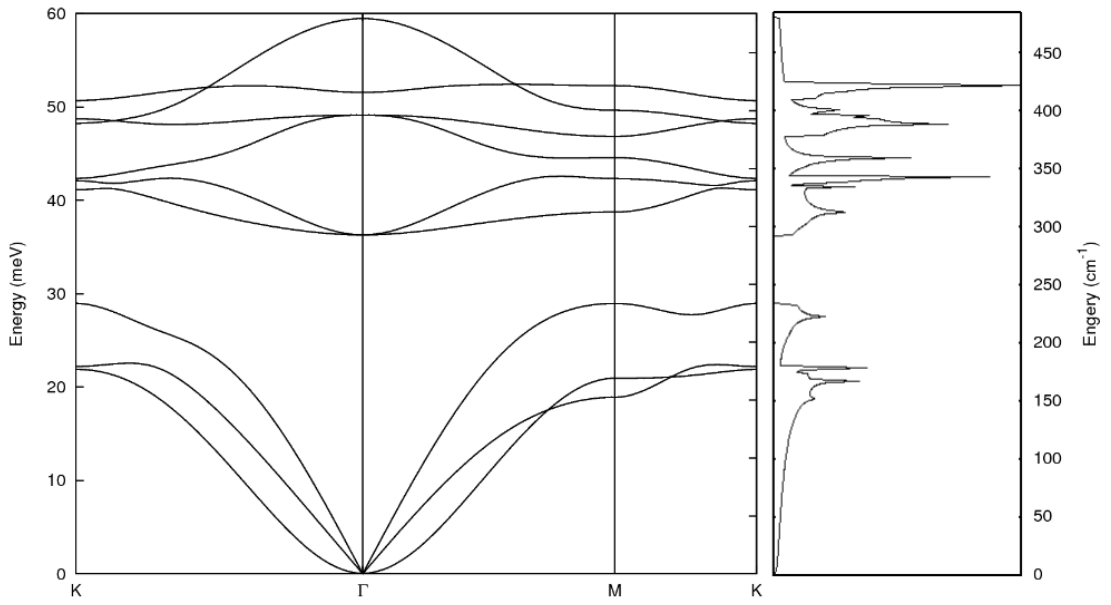


Figure 4.6: Phonon dispersion curve and phonon density of states of 1H-MoS_2. It can be seen that the largest peaks in the phonon DOS stem from regions where phonon dispersion flattens, leading to van Hove singularities.

4.3.2 Phonons

Fig. 4.6 shows the phonon dispersions of monolayer MoS_2 together with the phonon density of states. In general, the phonon dispersions are very similar to the bulk case, except they exhibit half the number of branches. In the bulk all single layer modes have split into two modes; the slightness of this splitting indicates that the interlayer bonding is weak. The phonon frequencies are real throughout the Brillouin zone, which demonstrates that the single-layer MoS_2 is dynamically stable. One major difference between the bulk and monolayer dispersions is the lack of low-frequency optical modes in 1H-MoS_2. The in-plane acoustic modes display a linear dispersion near the zone centre, whereas the out-plane ZA branch has a parabolic dispersion in a similar manner to that of graphene. Overall, the phonon frequencies for the single-layer are slightly lower in frequency in comparison to the bulk. This is due to the weak interlayer interaction acting as an additional

				Frequency (cm^{-1})		
D_{6h}	Character	Direction	Atoms	This work	Ref [181]	Ref [193]
A_2	Acoustic	Out of plane	Mo + S	0	0	0
E''	Raman	In plane	S	292.8	289.2	298.2
E'	IR + Raman	In plane	Mo + S	396.5	391.7	402.7
A_1	Raman	Out of plane	S	415.9	410.3	423.9
A_2''	IR	Out of plane	Mo + S	479.6	476.0	490.5

Table 4.3: The phonon symmetry representations of single-layer MoS_2 (point group D_{3h}). The phonon frequencies from this thesis are in good agreement with those of other DFT studies.

"spring" between sulphur atoms, leading to an increased frequency compared to the monolayer.

Due to the lack of inversion symmetry in 1H-MoS_2, the mode labels are different, and it is no longer the case that the Raman active and infrared (IR) active modes must be mutually exclusive. The IR active A_{2u} and E_{1u} modes of 2H-MoS_2 are replaced by the IR active A_2'' and E' modes respectively. The E' modes are also Raman active, as are the A_1' and E'' modes, which match the A_{1g} and E_{1g} modes of 2H-MoS_2, respectively. In Table 4.3 these modes are summarised, and the calculated phonon frequencies at the zone centre are compared to other DFT studies. It can be seen that they are in good agreement.

4.4 Rigid band electron doping in MoS_2

It has been proposed that, by better understanding its electron-phonon coupling, higher mobilities may be achieved in monolayer MoS_2 field effect transistors [43]. In these devices MoS_2 acts as an n-type carrier doped system, the surface charge of which has been estimated as $n \approx 2 \times 10^{14} \mathrm{cm}^{-2}$ [43]. It has also been observed, by use of the electric field effect in electric double layer transistors, that carrier

dopings as large as 3×10^{14} cm^{-2} can be achieved in few-layer MoS_2 [69]. It is therefore important to understand how the electron-phonon coupling varies as a function of electron doping.

The simplest method of describing the electric field induced carrier doping in a DFT calculation is called "rigid band" doping. In this method, the electronic structure and lattice dynamics are assumed to be unaffected by the presence of extra electrons, and so the pristine electronic eigenvalues and derivatives of the self-consistent phonon potential can be used to calculate the electron-phonon matrix elements. The degree of doping is determined by the placement of the Fermi energy into the conduction band. Fig. 4.5 shows the density of states (DOS) at the conduction band edge and the doping levels considered in this section. By integrating the DOS up to the placed Fermi level, the number of valence electrons per unit cell can be established. As there is only one formula unit per unit cell in 1H-MoS_2, there are 18 valence electrons in the pristine case. In order to understand the effect of electron doping over a wide but experimentally accessible range, first a very low doping level of 0.01 electrons per unit cell (e/u.c.), which corresponds to a carrier concentration of $\sim 1.2 \times 10^{13}$ cm^{-2}, was studied. The next doping level considered here is 0.06 e/u.c. or n_{2D}=7×10^{13} cm^{-2}. This has been suggested to be just above the minimum carrier concentration required for the onset of superconductivity in few-layer flakes of MoS_2 [44]. A further carrier concentration of $\sim 4 \times 10^{14}$ cm^{-2} or 0.32 e/u.c. has also been considered, in order to investigate claims that the superconducting transition temperature decreases at larger carrier concentrations.

4.4.1 Calculation details

In order to calculate the phonon linewidths required for an understanding of the total electron-phonon coupling in the most computationally efficient manner, the

`EPW` software package was used [130]. This requires use of maximally localised Wannier functions as explained in Chapter 3. The gap in the conduction band at 5 eV above the VBM allowed for a composite group of bands to be studied. There is no entanglement with higher energy states, and so the 9 valence bands and first 4 conduction bands can be fitted with 13 MLWFs without any need for complicated disentanglement procedure. The relevant energy window was set up using the `wannier90` code, which is called as a library from `EPW` [130, 131]. It was noted that the best method for finding Wannier functions with a large number of **k**-points was to first determine the MLWFs with a very small number of **k**-points, and then use the centres obtained as an input for the `wannier90` calculation with a large grid. Based on the density of states, the initial projections were chosen as the d orbitals of Mo and the p orbitals of S. The MWLFs found with these conditions display a maximum spatial quadratic spread of 1.65 Å. The accuracy of the Wannier interpolation method was checked by computing the electronic band structure obtained directly from *ab-initio* calculation and via interpolation. These two methods produced identical results.

For the Wannier interpolation to be effective, the spatial decay of the Hamiltonian matrix elements in the Wannier representation as a function of the distance between unit cells (in which the MLWFs are located) must be exponential [194]. A rapid spatial decay is also needed for the dynamical matrix in the Wannier representation and the e-ph matrix elements in the joint electron-phonon Wannier representation. It is therefore vitally important that these decays are checked before any calculation is undertaken with `EPW`. Fig. 4.7 shows the maximum values of these quantities as the distance between unit cells is increased. It can be seen that the Hamiltonian matrix elements in the Wannier representation are already very small for next-nearest-neighbour Wannier functions, with a $\sim 97.5\%$ reduction in

size. This justifies the use of next-nearest-neighbour tight-binding models for MoS_2 as in Ref [195]. It can also be seen that the interatomic force constants related to further neighbours are negligible in comparison to those of the nearest neighbour, in agreement with previous studies of the force constants between atoms in single-layer MoS_2 [181]. Although the range of the interatomic force constants does slightly increase in the monolayer compared to the bulk (due to the decrease in the dielectric screening which increases the long-range Coulomb interaction), the phonon dynamical matrix in the Wannier representation still shows strong spatial localisation [181]. In the case of the electron-phonon matrix elements in the joint e-ph Wannier representation, there are two spatial variables, and so it is convenient to discuss the two limiting cases as in Ref. [125]. In the first, the localised phonon perturbation and one electronic Wannier function are located within the same unit cell, and the distance to the unit cell which contains the other electronic Wannier function is measured. The expected spatial decay is then similar to that of the Hamiltonian matrix elements in the Wannier representation. This is indeed the case, as displayed by Fig. 4.8. The second case refers to when two electron Wannier functions are in the same unit cell, and the localised phonon perturbation is located in some other unit cell a distance $\mathbf{R}$ away. The spatial decay in this case is then very rapid for next-nearest-neighbours onwards.

A uniform unshifted $16 \times 16 \times 1$ grid has been used to sample both the electrons and phonons in the Brillouin zone. This corresponds to interactions in the Wannier representation extending to ~ 27.5 Å. However, the spatial localisation of Fig. 4.7 and 4.8 are already very good at much shorter values of $\mathbf{R}$ and so it was decided to use a sampling of $8 \times 8 \times 1$ for both the coarse $\mathbf{k}$-point and $\mathbf{q}$-point grids. This corresponds to a maximum $\mathbf{R}$ of ~ 14 Å. The coarse phonon grid contains 10 irreducible phonon wavevectors compared to 30 for the larger $16 \times 16 \times 1$ grid.

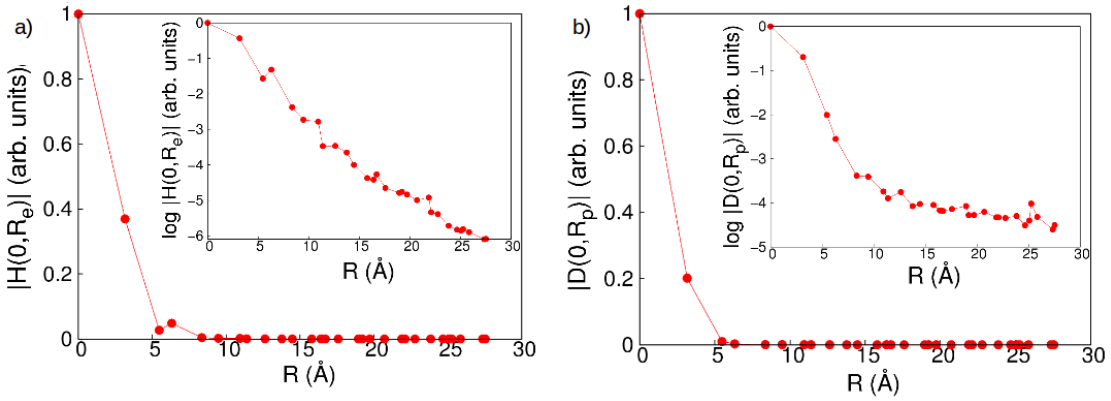


Figure 4.7: The spatial decay of the largest components of a) the Hamiltonian $H^{\text{el}}_{0,\mathbf{R_e}}$, and b) the dynamical matrix $D^{\text{ph}}_{0,\mathbf{R_p}}$. Values are normalised to the largest element. The same value is shown on the inset on a logarithmic scale.

This represents a large time-saving in the computation of the dynamical matrices and derivatives of the self-consistent potential needed as inputs for the `EPW` calculation. As there is a lack of inversion symmetry in 1H-MoS_2, `EPW` also requires the explicit calculation of phonons when $-\mathbf{1}$ is not in the star of $\mathbf{q}$. For this reason the dynamical matrices and potentials are calculated explicitly for a further 5 phonon wavevectors for the $8 \times 8 \times 1$ grid and 21 phonon wavevectors for the $16 \times 16 \times 1$ grid. To check that the symmetry operations were indeed calculating the correct dynamical matrices and potentials for the full Brillouin zone, calculations were done by obtaining these quantities explicitly for all 64 points of the $8 \times 8 \times 1$ grid and all 256 $\mathbf{q}$-points of the $16 \times 16 \times 1$, and the resulting e-ph matrix elements obtained via `EPW` were compared.

Once it had been established that coarse grids of $8 \times 8 \times 1$ were suitable for the `EPW` inputs of the electronic eigenvalues and eigenfunctions, and for the phonon dynamical matrices and derivatives of the self-consistent potential, the next step was to determine the number of electron and phonon wavevectors needed for the interpolated results to be considered converged. As can be seen from Eq. 3.20, cal-

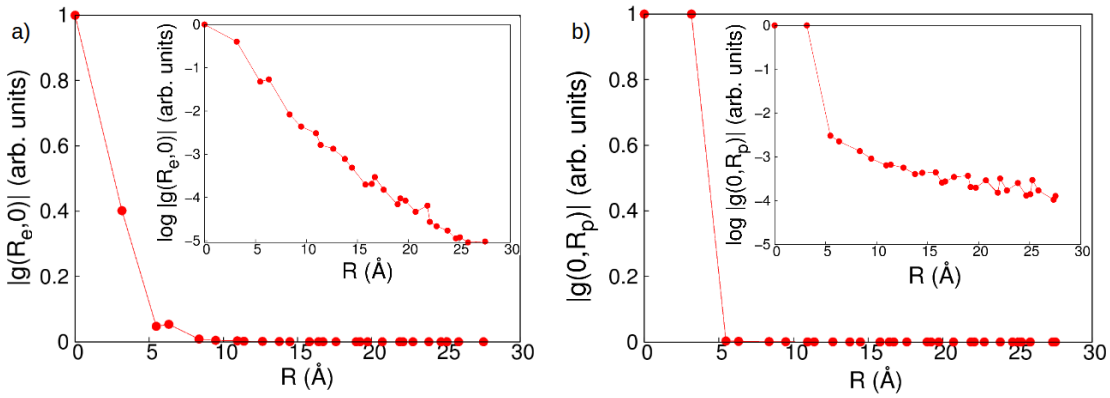


Figure 4.8: The spatial decay of the largest components of a) the electron-phonon matrix elements in the Wannier representation $g(\mathbf{R_e}, 0)$ and b) the electron-phonon matrix elements in the Wannier representation $g(0, \mathbf{R_p})$. Values are normalised to the largest element. The same value is shown on the inset on a logarithmic scale.

culation of the phonon self-energy requires an integration over the Brillouin zone, and due to the Dirac delta functions, only states near the Fermi surface will contribute. It therefore requires a very large number of **k**-points in the interpolated fine grid. In practical calculations, the Dirac delta functions are replaced by Gaussian functions with a small standard deviation, representing a smearing parameter. This smearing parameter will effect how many **k**-points are required and also the value of the density of states at a certain energy. The smallest smearing value considered in this thesis is 10 meV, and so for our convergence tests of the fine **k**-point grid this was the value used. Table 4.4 shows the calculated phonon linewidths for the highest-frequency acoustic mode (LA) and the Raman active A_1 mode at the K point for a variety of interpolated fine **k**-point grids. The number of electron wavevectors refers to the number in the irreducible wedge of the Brillouin zone. Although only certain modes at one phonon wavevector are shown in Table. 4.4 for clarity, the convergence was checked at all phonon branches for a number of different **q**-points. The converged value of 125000 electron wavevectors was used for all calculations of the phonon self-energies in this chapter, and was checked to

	Phonon linewidth (meV)						
No. **k**-points	1000	10 000	100 000	125 000	200 000	500 000	1 000 000
LA	1.829	1.278	1.218	1.201	1.204	1.201	1.203
A_1	1.496	1.103	1.103	1.138	1.142	1.140	1.139

Table 4.4: Convergence of the phonon linewidths at the K point for **k**-point grids of different sizes. A smearing of 10 meV was used. The number of points refers to those in the irreducible Brillouin zone.

be appropriate for all different doping levels considered. In the case of calculations with larger smearing values, such as 50 meV and 100 meV, a smaller number could have probably been used.

The total electron-phonon coupling parameter, λ, and the Eliashberg spectral functions, α^2F, are both computed via summations over a number of phonon wavevectors as shown in Chapter 3. Therefore the convergence over **q**-points in the fine grid must also be considered. Fig. 4.9 shows the how value of λ changes as the number of random **q**-points in the irreducible wedge of the Brillouin zone changes. Although this convergence depends greatly on the type of doping and doping level used, all calculations of the Eliashberg spectral function and λ were converged by 18000 **q**-points and so this was the number used in all calculations of this kind. The Dirac delta function of Eq. 3.25 was smeared using a Lorentzian broadening of 0.2 meV. In order to speed up the calculations it was noted that only **k**-points with states which lie within $4\times$ the smearing parameter (σ) of the Gaussian which replaces the Dirac delta functions in Eq. 3.20 actually contribute to the phonon linewidth. Thus an energy window was defined as 4σ, or $4\omega_{\max}$ (where $\omega_{\max}$ is the largest phonon frequency), depending on which is larger, either side of the Fermi energy, and only those **k**-points with states in this energy window entered the calculation. This allowed for large numbers of the 125000 electron wavevectors to be skipped, depending on the phonon wavevector being calculated.

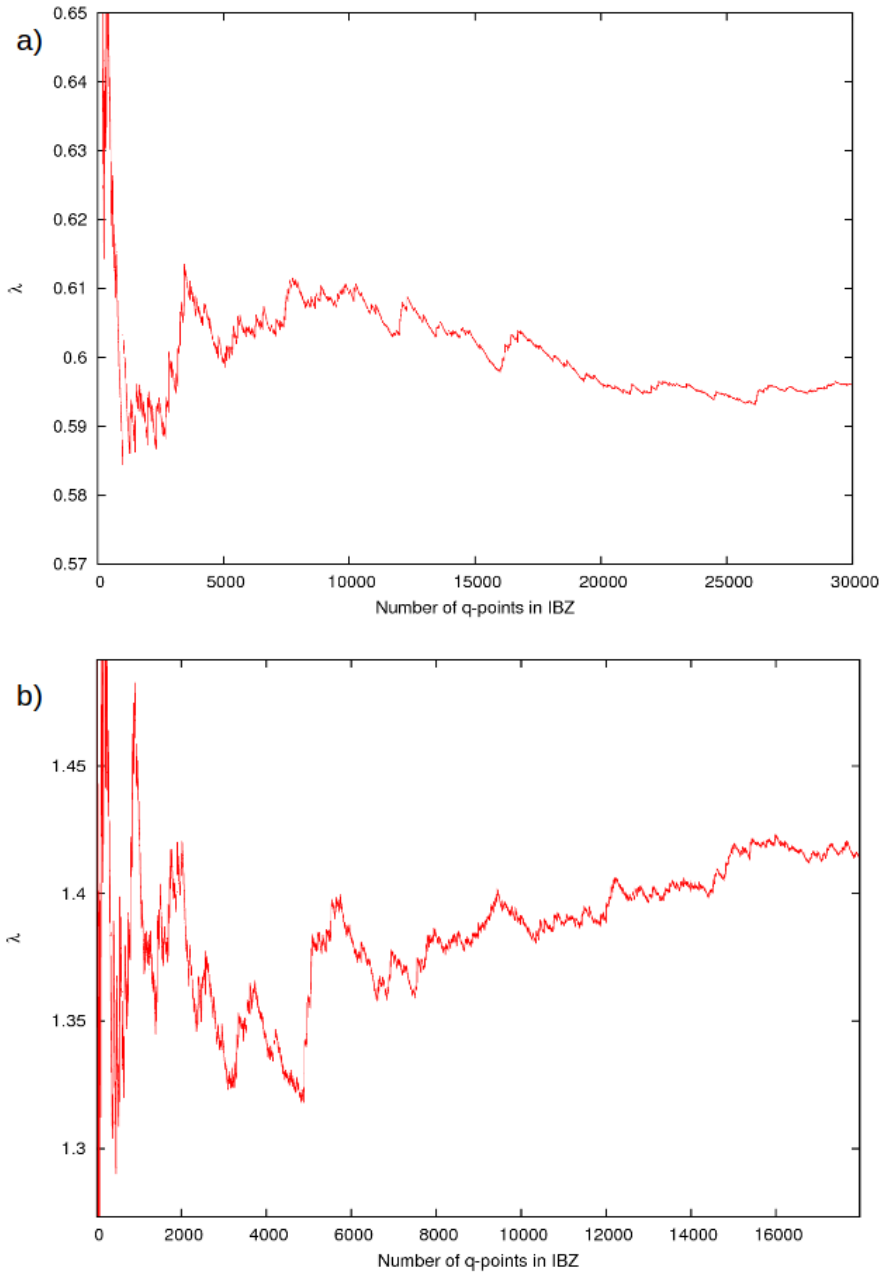


Figure 4.9: Convergence of the electron-phonon coupling constant, λ, with respect to the number of **q**-points in the irreducible Brillouin zone. a) Displays a doping level which converges rapidly and b) is slower to converge. However, both panels demonstrate that 18000 **q**-points are sufficient for accurate calculations of λ. It should be noted that traditional methods of calculating λ which use less than 1000 **q**-points are clearly unsuitable.

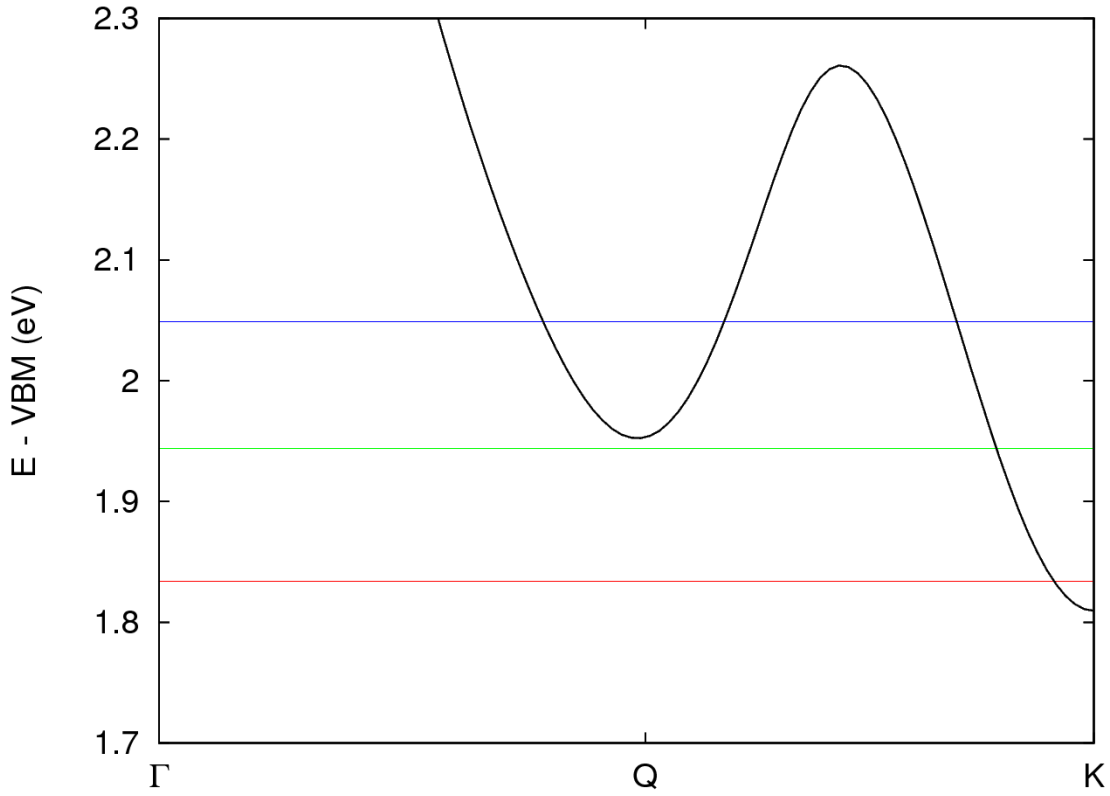


Figure 4.10: The electronic band structure at the bottom of the conduction band in 1H-MoS_2. The three horizontal lines correspond to the different Fermi levels in the rigid band approximation. The red line corresponds to 0.01 e/u.c, the green line corresponds to 0.06 e/u.c, and the blue line is the Fermi level for 0.32 e/u.c. $E = 0$ is set to the valence band maximum.

4.4.2 Total electron-phonon coupling

The total electron-phonon coupling was calculated for the three doping levels considered within the rigid band approximation. That is 0.01 e/u.c, 0.06 e/u.c, and 0.32 e/u.c, as shown in Fig. 4.10. In order to analyse the strength of this interaction, the Eliashberg spectral function as well as the cumulative e-ph coupling parameter $\lambda(\omega)$ are plotted in Figs. 4.11-4.13.

For the lowest doping level, the α^2F is particularly simple with only a few sharp peaks contributing to the total λ. The coupling can be explained by considering the Fermi surface. From the red line in Fig. 4.10, it can be seen that the Fermi surface

for this doping level will consist of a very small electron pocket centred at K. The only phonon wavevectors which can scatter an electron from one point on the Fermi surface to another are those at or very near $\mathbf{q} = K$, which scatter from one Fermi sheet at the zone edge to another (K-K' intersheet scattering), and those very near but not actually at $\mathbf{q} = \Gamma$, which scatter within the Fermi sheet (K-K intrasheet scattering). The intersheet scattering for this doping level is shown schematically in Fig. 4.14. The peaks in the α^2F of Fig. 4.11 due to intersheet scattering are the peak at 22 meV, which is due to transverse acoustic phonons with $\mathbf{q} = K$, and the peak at 42.5 meV, which is due to longitudinal optical (LO) E' modes of phonons with $\mathbf{q} = K$. The other peaks can all be attributed to intrasheet scattering of phonons with wavevectors very near Γ. The small but broad peak at 2.5-6 meV is due to the longitudinal acoustic modes. It can be seen in Eq. 3.21 that the phonon frequency appears in the denominator of the expression for the electron-phonon coupling parameter. Thus, low frequency phonons such as these contribute greatly to the total λ. The remaining peaks include a very small feature at 36 meV due to LO E'' modes and a large peak at 49.1 meV due to LO E' modes. The largest peak in the isotropic Eliashberg spectral function for monolayer MoS_2 doped with 0.01 e/u.c. is at 51.6 meV, and is due to the intrasheet scattering of the A_1 mode. The total electron-phonon coupling in this case is $\lambda = 0.09$. Two thirds of this coupling is derived from the acoustic modes. It should be noted that the value of the smearing parameter used in the calculation of Fig. 4.11 is very important for obtaining a correct Fermi surface, and hence the correct electron-phonon coupling. In order to obtain a correct description of the electronic structure of 0.01 e/u.c. doped single-layer MoS_2 a smearing of 10 meV was used. However, if a smearing of 100 meV is used then a very different α^2F is calculated. This is because the smearing changes the Fermi surface so that a sheet appears at Q as well as K.

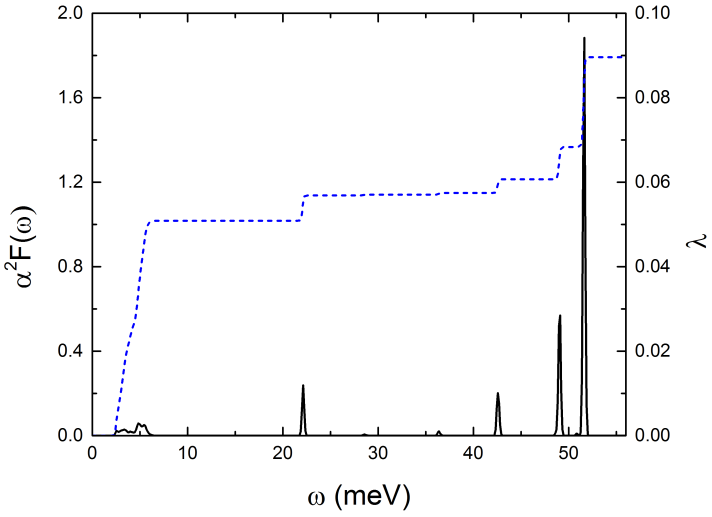


Figure 4.11: The isotropic Eliashberg spectral function, $\alpha^2F(\omega)$, for the rigid band doping of 0.01 e/u.c. (black lines). The cumulative contribution to the electron-phonon coupling, λ, is shown by the blue dashed line.

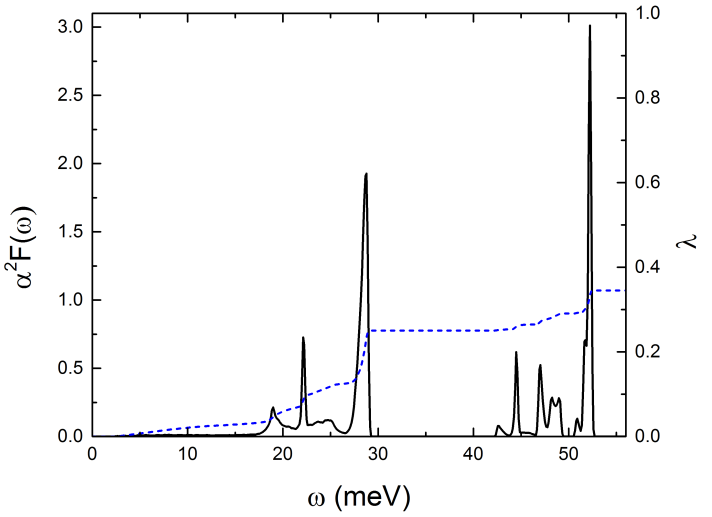


Figure 4.12: The isotropic Eliashberg spectral function, $\alpha^2F(\omega)$, for the rigid band doping of 0.06 e/u.c. (black lines). The cumulative contribution to the electron-phonon coupling, λ, is shown by the blue dashed line.

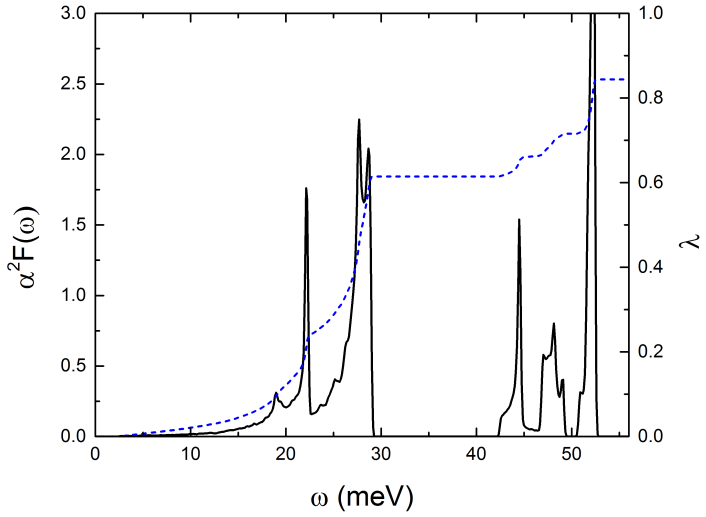


Figure 4.13: The isotropic Eliashberg spectral function, $\alpha^2F(\omega)$, for the rigid band doping of 0.32 e/u.c. (black lines). The cumulative contribution to the electron-phonon coupling, λ, is shown by the blue dashed line.

It can be seen that increasing the electron doping from 0.01 e/u.c. to 0.06 e/u.c. changes spectral function quite dramatically. In Fig. 4.12, there are many more peaks in the α^2F than in Fig. 4.11. Again, this can be explained by considering the Fermi surface and the possible scattering mechanisms. From the green line in Fig. 4.10, it might be expected that the Fermi surface would again consist of a single sheet at K. However, the minimum at Q is very close in energy to the Fermi level, and so electrons can be scattered from the Q valley to K and vice versa. The Fermi surface can thus be considered as two electron pockets, with one sheet centred at K and another much smaller one at Q. All of the peaks in the 0.01 e/u.c. spectral function remain; however, additional peaks from the newly available scattering channels are present. These intersheet scattering mechanisms are shown schematically in Fig. 4.15. The lowest energy new peak is at 19.2 meV, and is due to the coupling of transverse acoustic modes with phonon wavevectors

$\mathbf{q} = M$. Intervalley scattering between K and Q' as well as between Q and Q' can be induced by $\mathbf{q} = M$ phonons. The TA modes couple between the two different valleys K and Q'. The broad peak at 24 meV is also due to scattering between K and Q', but caused by LA modes with $\mathbf{q} = Q$. The large peak at 28.7 meV can be attributed to LA modes, although for $\mathbf{q} = M$ scattering between Q and Q'. Scattering between Q and Q' via phonons with $\mathbf{q} = M$ also causes the peaks at 44.5 meV and 47 meV, via LO E' and TO E' modes, respectively. Like the doping level of 0.01 e/u.c, the largest peak in the α^2F is at 52 meV. This arises from a combination of the dominant intrasheet scattering of A_1 modes with $\mathbf{q} \approx \Gamma$, dominant intersheet scattering of A_1 modes with $\mathbf{q} = M$, and also less important intervalley scattering mechanisms of the A_1 modes with $\mathbf{q} = Q$ and $\mathbf{q} = K$. As the phonon dispersion of the A_1 mode is very flat across the whole Brillouin zone, all of these different mechanisms appear in the spectral function at the same peak between 51-52 meV. The effect of all these additional scattering mechanisms is a large enhancement of the total electron-phonon coupling constant, $\lambda = 0.35$. This is almost four times greater than the 0.01 e/u.c. doping level. It can be seen that acoustic phonons are responsible for just over 70% of the total λ.

Addition of further electrons results in an increase in total coupling λ in a very uniform manner from 0.06 e/u.c. to 0.32 e/u.c, as shown in Fig. 4.12. There are no new peaks in the α^2F; however, the existing peaks have been enhanced. This can be explained once more by the difference in the Fermi surface. From the blue line in Fig. 4.10, it can be seen that the Fermi surface will again have two sheets, one centred at K and the other at Q. Both pockets are much wider than in the 0.06 e/u.c. case. This is what drives the larger coupling. The total $\lambda = 0.84$, again with just over 70% of the total λ deriving from the acoustic phonon modes.

The total λ increases linearly with increasing density of states once both the K

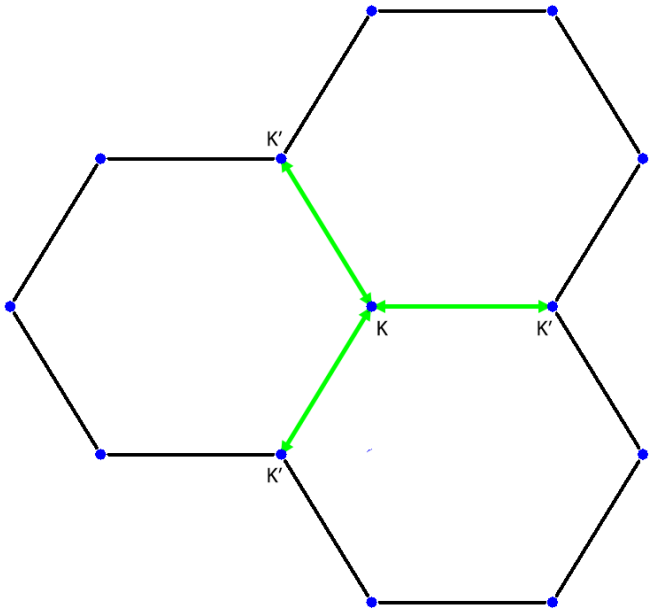


Figure 4.14: A schematic of the phonon intervalley scattering in monolayer MoS_2 for the 0.01 e/u.c. doping level. The Fermi surface is represented by the blue filled circles at K. The green arrows represent $\mathbf{q} = K$ phonons.

and Q valleys are occupied. For 0.06 e/u.c, $\lambda = 0.35$ and the density of states at the Fermi level is 0.518 states/spin/eV/unit cell, therefore $\lambda/N_F = 0.67$. At 0.32 e/u.c., $\lambda/N_F = 0.66$, as $\lambda = 0.84$ and $N_F = 1.289$. Therefore, in the rigid band model, there is no indication of a decrease in λ at higher doping levels, as might be expected from the trend in the superconductivity found in few-layer flakes of MoS_2 [44]. One possible reason for this failure to reproduce the expected trend could be the limitations of the rigid band model. The electronic structure may be modified by the electron doping, and this could subtly change the e-ph coupling. Likewise, the phonon frequencies may soften or harden due to the presence of the extra electrons. In order to investigate this aspect further, the doping was modelled within a jellium model.

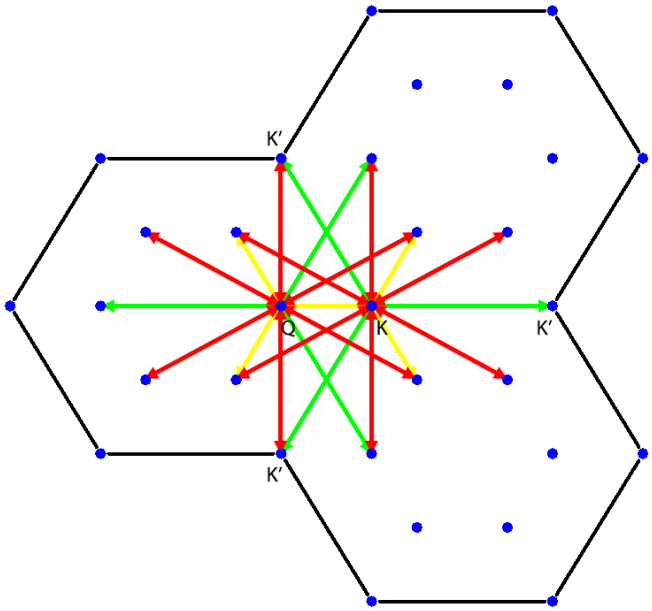


Figure 4.15: A schematic of the intervalley phonon scattering in electron-doped monolayer MoS_2 when the Fermi surface consists of pockets at K and Q, as in the 0.06 e/u.c. and 0.32 e/u.c. doping levels in the rigid band model. The Fermi surface is represented by the blue filled circles at K and Q. The green arrows represent $\mathbf{q} = K$ phonons, yellow arrows represent $\mathbf{q} = Q$ phonons, and red arrows represent $\mathbf{q} = M$ phonons.

Name	Carrier concentration (cm^{-2})	a (Å)
0.06	7×10^{13}	3.146
0.06-fix	7×10^{13}	3.132
0.1	1.2×10^{14}	3.183
0.1-fix	1.2×10^{14}	3.132
0.17	2×10^{14}	3.219
0.17-fix	2×10^{14}	3.132

Table 4.5: Lattice parameter and carrier concentrations of the various doping levels considered within the jellium model.

4.5 Jellium model electron doping in MoS_2

In a jellium model, carrier doping is simulated by the addition of excess electronic charge into the unit cell which is compensated by a uniform positive background. In order to understand the evolution of the electron-phonon coupling as a function of electron doping, and also so that our results may be used for calculation of the superconducting transition temperature in the next chapter, three doping levels were considered, which correspond to different regimes in the carrier concentration vs T_c plot of Fig. 1.3. The first is 0.06 e/u.c., which corresponds to the carrier concentration at the onset of the superconductive phase, $n_{2D} = 7 \times 10^{13}$ cm^{-2}. The next doping level to be considered is that which corresponds to the carrier concentration for which the maximum T_c is found experimentally for few-layer MoS_2, $n_{2D} = 1.2 \times 10^{14}$ cm^{-2} or 0.1 e/u.c. The final doping level corresponds to an even higher, yet still obtainable by electrolyte gating techniques, carrier concentration of $n_{2D} = 2\times10^{14}$ cm^{-2} or 0.17 e/u.c. It was also hoped that an even higher doping concentration might be modelled to simulate the chemical doping regime, although for technical reasons (which will be described in the next chapter) this proved impractical.

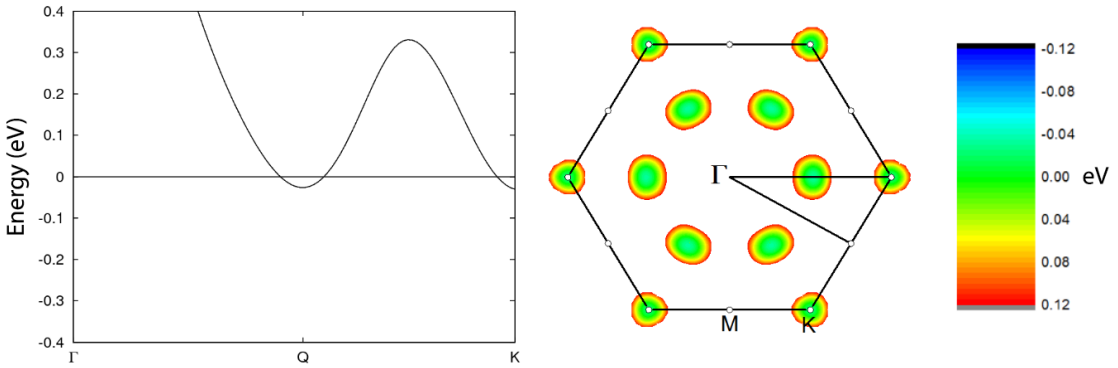
It is not obvious what the lattice parameters should be in an electron doped

monolayer. Therefore it was decided to calculate all three doping levels with both a fully optimised lattice parameter, keeping the vacuum fixed, and also with the parameter fixed for all dopings. The fixed lattice parameter was set to the optimised parameter of the pristine case. The lattice parameters for the various doping levels considered in this section are summarised in Table 4.5. For the remainder of this thesis, the notation "0.06 e/u.c." will refer to the relaxed parameter for that doping, while "0.06-fix e/u.c." will denote the same carrier concentration but with the pristine lattice constant.

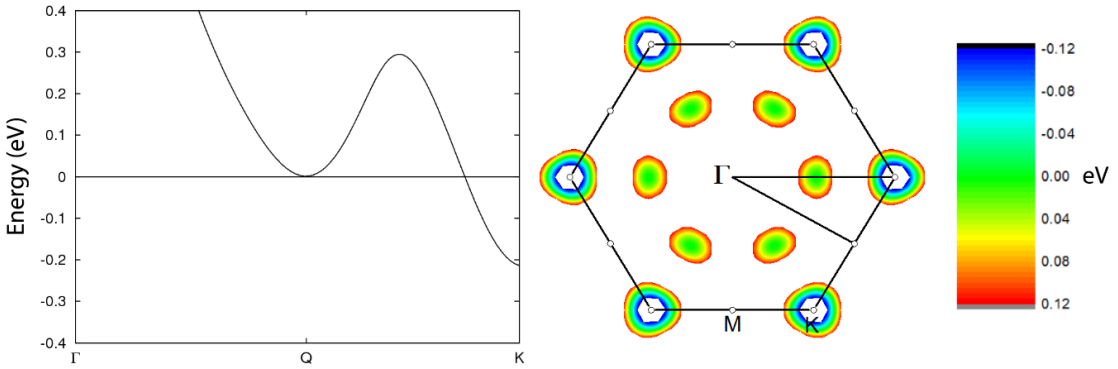
4.5.1 Electronic structure

Figs. 4.16-4.17 display the evolution of the electronic structure upon electron doping for both the fully relaxed and fixed lattice parameters. The valence bands are almost identical to the pristine case, therefore only the lowest energy conduction band is of interest. It can been seen that the Fermi surfaces, which are denoted by the green regions of the energy isosurfaces, consist of pocket at the K point and also at Q. In the case of the relaxed lattice monolayers, the increase in carrier concentration leads to an increase in the size of the Fermi sheet at K, as all the additional electrons fill these states. The size of the Fermi sheet at Q is not affected by the doping and remains very small. At the lowest doping level of 0.06 e/u.c., the difference in the energies of the minima in the conduction band at K and Q is very small. However, as the doping increases, the difference in these energies increases greatly as the conduction band valley at Q becomes much higher in energy than the valence band minimum. The Fermi sheets at K for the doping levels of 0.1 e/u.c. and 0.17 e/u.c. display trigonal warping. This effect is a consequence of the hexagonal symmetry, and has been observed in other low dimensional materials such as graphene and carbon nanotubes [196, 197]. The situation for the fixed

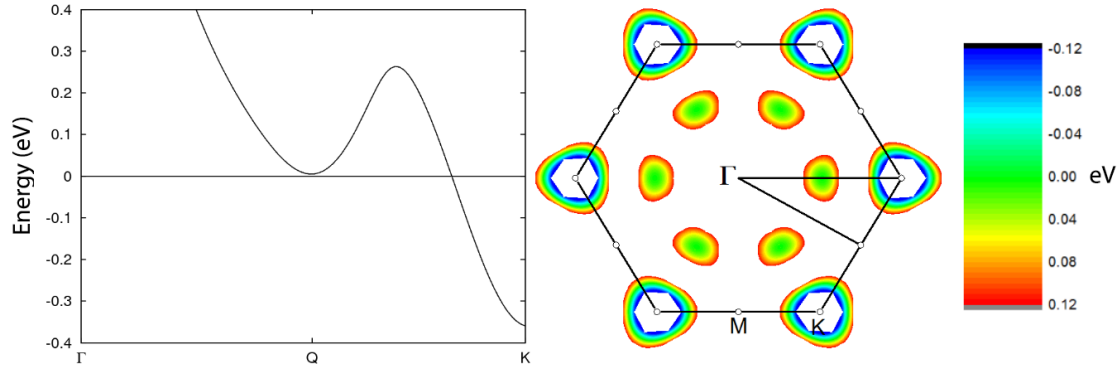
lattice monolayers, however, is quite different. At the lowest doping concentration the electrons occupy states near the conduction band minimum. An increase in doping causes the energy difference in the minima at Q and K to decrease, and eventually the minima swap; at the largest doping level considered, 0.17 e/u.c, the Q point has become the conduction band minimum. As a result, the Fermi surface changes considerably, from a single small sheet at K, to small sheets at both Q and K, to finally a large sheet at Q and a very small sheet at K. The differences in the evolution of the Fermi surfaces with increased electron doping should allow for experimental clarification of whether the model with fixed lattice constants or with optimised geometry better describes the physics of the electron-doped monolayer MoS_2.



(a) 0.06 e/u.c.

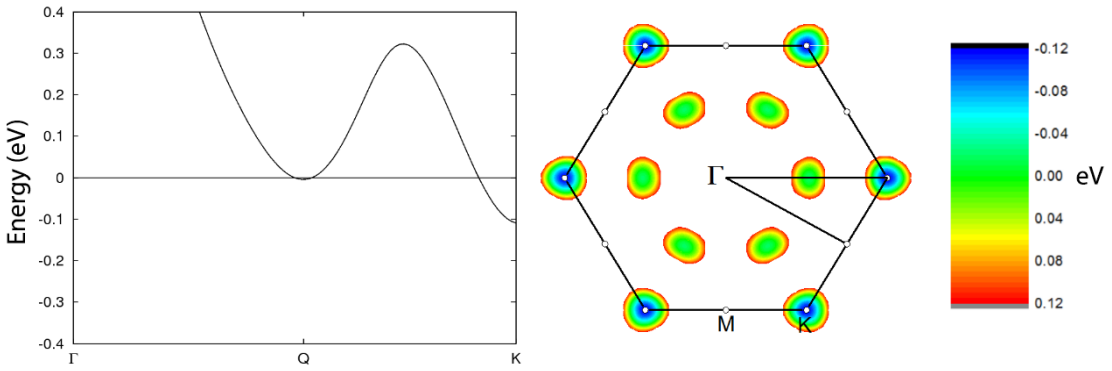


(b) 0.1 e/u.c.

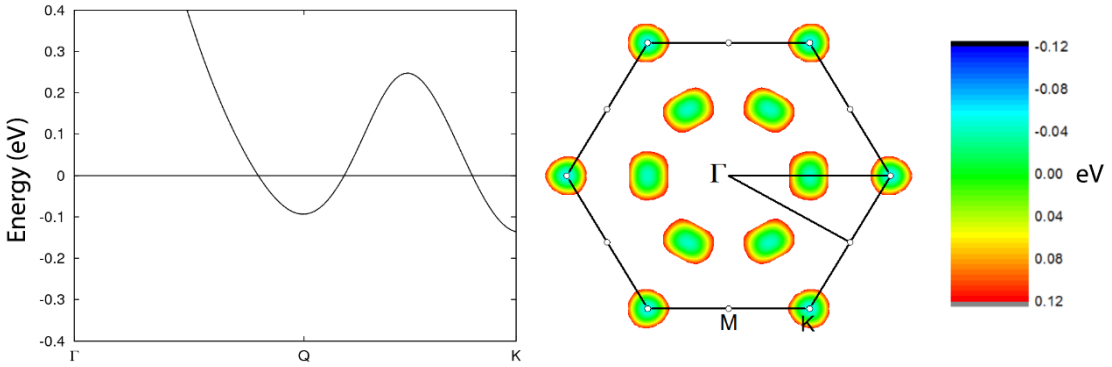


(c) 0.17 e/u.c.

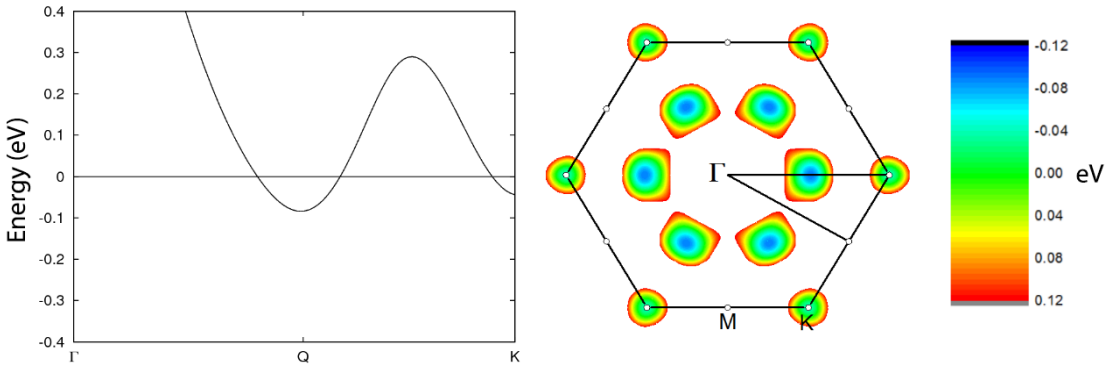
Figure 4.16: The electronic band structure for the bottom of the conduction band and Fermi surface for the optimised unit cell jellium model. The individual captions provide information on the doping levels.



(a) 0.06-fix e/u.c.



(b) 0.1-fix e/u.c.



(c) 0.17-fix e/u.c.

Figure 4.17: The electronic band structure for the bottom of the conduction band and Fermi surface for the fixed unit cell jellium model. The individual captions provide information on the doping levels.

4.5.2 Phonons

The lattice dynamics for the jellium model doped monolayers were studied and can be seen in Figs 4.18a and 4.18b. All doping levels, no matter the structural geometry considered, display a softening in phonon modes, which are even under mirror transformation with respect to the Mo plane, at the M point. The optical phonon modes are plotted in Fig. 4.19, and it can be seen that the E' and A_1 modes are even, as are the LA and TA modes, while the E'' and A_2'' modes are odd under mirror transformation with respect to the Mo plane. The Kohn anomaly at M is associated with the intersheet scattering of electrons from $Q - Q'$. The A_1 and LA modes soften the most, indicating strong coupling of these modes at M. An increase in doping leads to a larger phonon softening as expected.

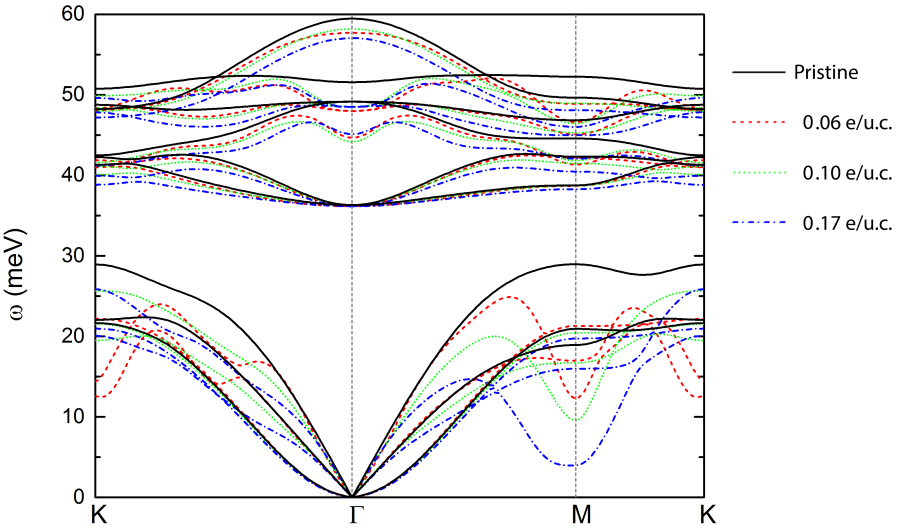
There is also substantial phonon softening at the zone centre for all doping levels considered. This is due to the intrasheet scattering of electrons on the Fermi surface. The E'' and A_2'' modes are relatively insensitive to the doping concentration, in good agreement with prior calculations [167]. The frequencies of the phonon modes at the zone centre are shown in Fig. 4.19, and clarify how the softening develops in certain modes with increasing electron doping.

In Fig. 4.18a, the phonon dispersions for the different doping levels with the relaxed unit cell are compared. It can be seen that the green dotted lines and blue dot-dashed lines, which correspond to the 0.1 e/u.c. and 0.17 e/u.c. doping levels, respectively, are very similar. The main difference is that that the 0.17 e/u.c. phonons have slightly lower frequencies everywhere in the Brillouin zone and particularly in the LA mode near M. This can be explained by the increase in the size of the Fermi sheets leading to increased phonon softening. The red dashed lines of the 0.06 e/u.c. doping level are, however, quite different. There

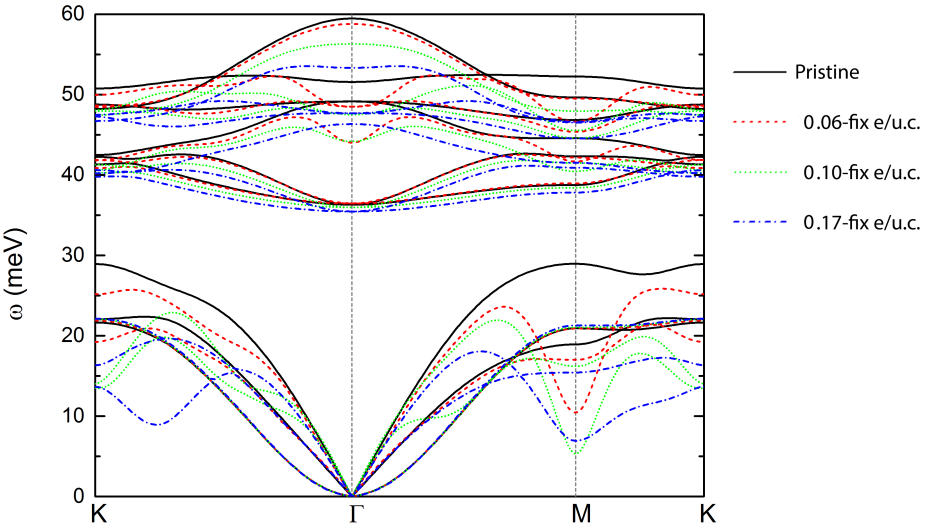
are additional Kohn anomalies at the Q and K points causing a large softening of the LA and TA modes at these phonon wavevectors. These can be explained by considering the Fermi surface of Fig. 4.16. The size of the electron pockets at K and Q are very similar. This means that all the scattering channels shown in Fig. 4.15 lead to a Kohn anomalies. As electrons are added to the unit cell, the sizes of the Fermi sheets at K and Q differ, as seen in Figs. 4.16b and 4.16c. The result is that scattering from Q to K no longer leads to Kohn anomalies. Thus only the scattering between Q and Q' via $\mathbf{q} = M$ leads to a Kohn anomaly. It might be expected that in the 0.1 e/u.c. and 0.17 e/u.c. doping levels, there is a large softening at K from scattering from $K - K'$; however this is not the case, as there is trigonal warping in the Fermi sheets at K and K'. This means the the sheets are no longer equivalent and so the phonon softening does not occur.

The calculated phonon dispersions for electron-doped 1H-MoS_2 within a jellium model with a fixed lattice parameter are shown in Fig. 4.18b. Again, the large softening of the LA and TA modes at K and Q are present for some doping levels but not others. Due to the difference in how the doping affects the lowest conduction band in the fixed lattice case compared to the relaxed unit cell, it is the lowest doping level which has a large difference in the shapes of the Fermi sheets at K and Q. This results in a lack of phonon softening at K and Q as explained above. The 0.1-fix e/u.c and 0.17-fix e/u.c. doping levels have Fermi surfaces with similar sized Fermi sheets (Figs. 4.17b and 4.17c) and so display the expected softening of the LA and TA modes at K and Q.

While the modes which did not soften significantly upon doping such the A_2'' and E'' modes converged rapidly with respect to the number of $\mathbf{k}$-points used to obtain them, the same cannot be said of the LA and A_1 branches. As a result the convergence of all the phonon modes was extensively studied at the high symmetry



(a) Jellium model with a relaxed unit cell.



(b) Jellium model with a fixed unit cell.

Figure 4.18: The calculated phonon dispersion curves for doped monolayer MoS_2 when (a) the lattice parameter has been relaxed and (b) the lattice parameter is fixed at the pristine value. The doping levels considered are 0.06 e/u.c. (red dashed lines), 0.10 e/u.c. (green dotted lines), and 0.17 e/u.c. (blue dot-dashed lines). The pristine case is included for comparison (black lines).

points of Γ, K and M. **k**-point grids ranging in size from $4 \times 4 \times 1$ to $128 \times 128 \times 1$ and smearings from 250 meV to 10 meV were considered. It was found that in order to obtain a converged Kohn anomaly at the M point, a **k**-point grid of $64 \times 64 \times 1$ and a smearing parameter of 10 meV were needed. For the 0.17-fix doping level, it was found that imaginary phonon frequencies were calculated at the M point for a 10 meV smearing even using a dense grid of $128 \times 128 \times 1$. Thus a larger smearing value of 100 meV was used for this doping level. It is, however, worth noting that there may be a dynamic instability, and so the results for this doping level cannot be considered as reliable.

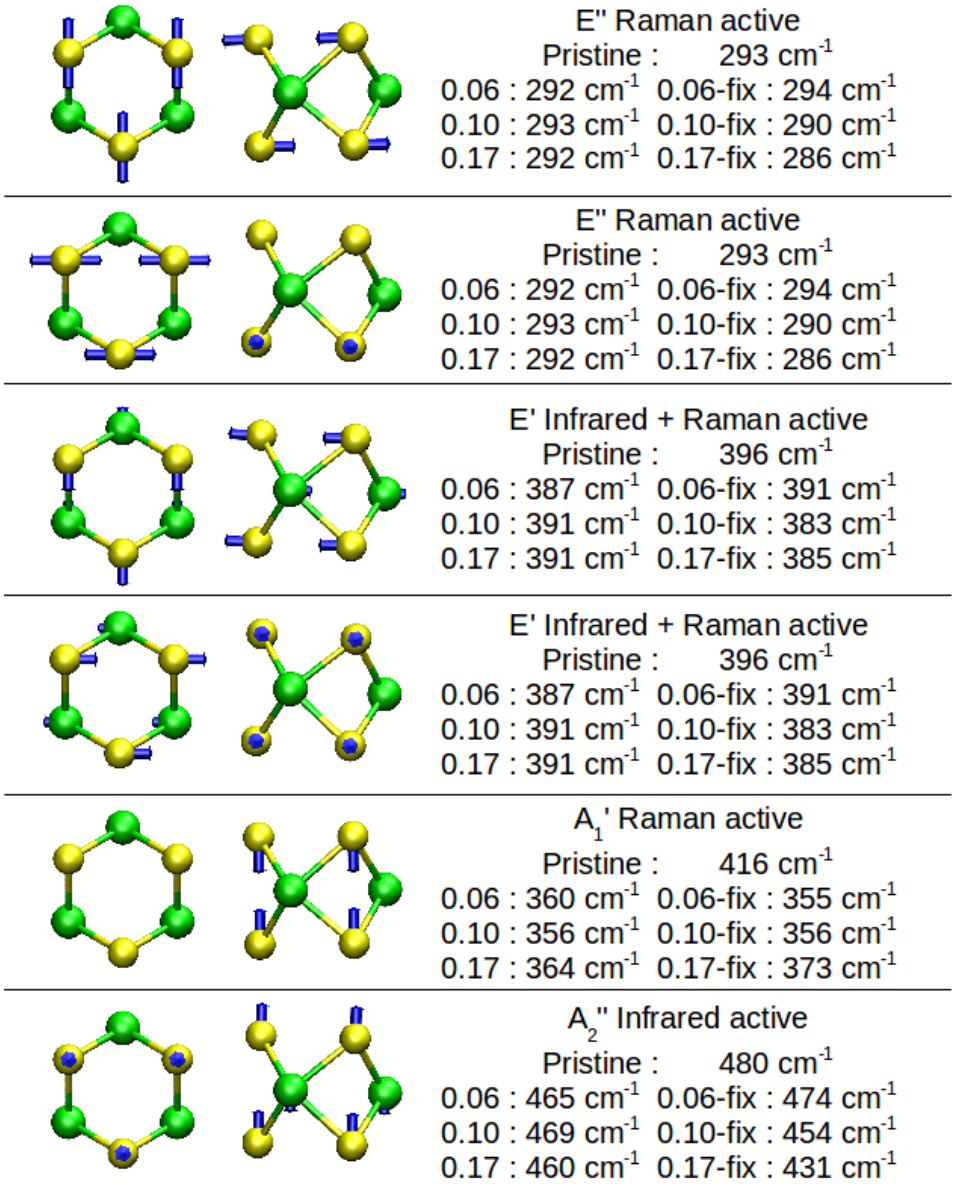
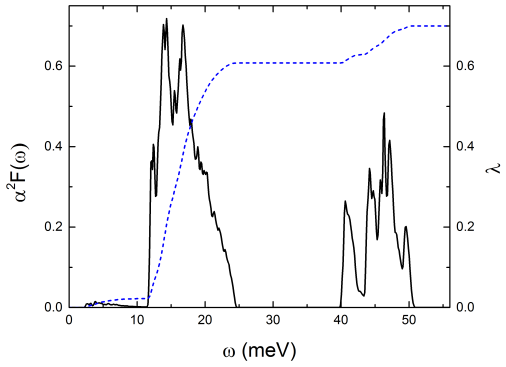


Figure 4.19: The optical phonon modes of monolayer MoS_2. The left panel shows the phonon modes from both a top view and a side view. The Mo atoms are in green and the S in yellow. The mode frequencies at Γ are presented for all the different doping levels considered in this work. It can be seen that there is a larger softening in phonon modes which are even under mirror transformation in the Mo plane.

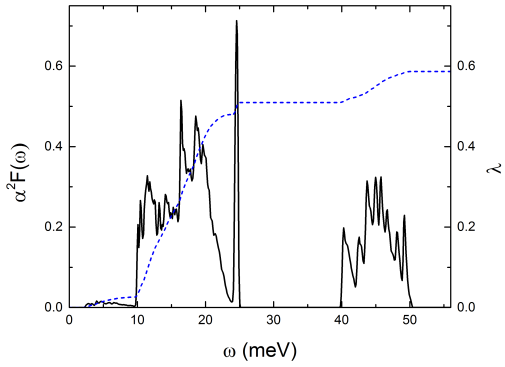
4.5.3 Total electron-phonon coupling

The isotropic Eliashberg spectral functions were calculated for all 6 jellium models considered. This was repeated for three different smearing parameters of 100 meV, 50 meV and 10 meV. As expected, the smaller the smearing, the finer the features which appear in the $\alpha^2F(\omega)$. Although the choice of smearing parameter influences the value of the calculated λ, the trends discussed here are not affected by the smearing.

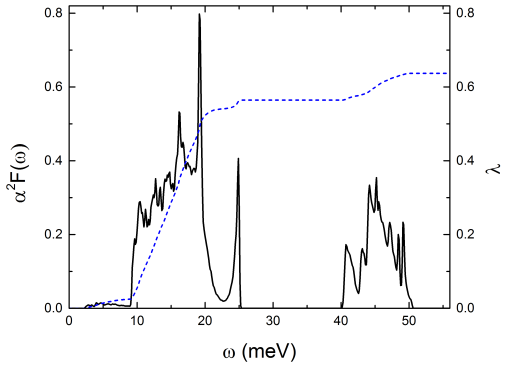
It can be seen that for the relaxed unit cells, which are displayed in order of increased electron doping in the left hand column of Figs. 4.20- 4.22, the increase in doping, which softens the phonons, leads to the largest e-ph coupling at the highest doping level. The contribution to the coupling from the acoustic modes, which is already around 85% for 0.06 e/u.c., increases to $\sim$ 95% for 0.17 e/u.c. The decrease in the phonon frequencies, especially for the LA mode, result in a larger λ as compared to that obtained from the rigid band model in Section 4.4. However, the λ actually decreases between the 0.06 e/u.c. and 0.1 e/u.c. doping levels, despite an increase in the density of states. Once more, the explanation is due to the underlying electronic structure. For the 0.06 e/u.c. doping level the acoustic phonons soften at M, K and Q due to the similar sizes of the Fermi sheets at K and Q. Thus the LA and TA phonons, which strongly couple at these phonon wavevectors, have a lower frequency. This results in a larger coupling. In Figs. 4.20a, 4.21a, and 4.22a it can be seen that peaks of high intensity in the isotropic Eliashberg spectral function have shifted to lower frequencies due to this phonon softening at K and Q compared to Figs. 4.20c, 4.21c, and 4.22c. The α^2F functions for both the 0.1 e/u.c. and 0.17 e/u.c. doping levels display a peak at around 25 meV which is missing in the spectral function of the 0.06 e/u.c. doping



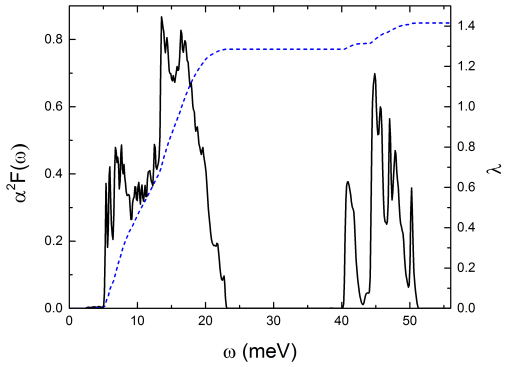
(a) 0.06 e/u.c. ($\sigma = 100$ meV).



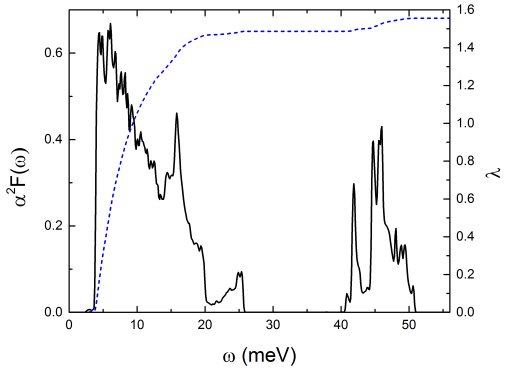
(b) 0.06-fix e/u.c. ($\sigma = 100$ meV).



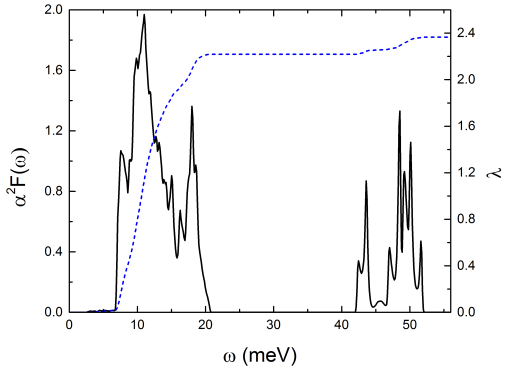
(c) 0.1 e/u.c. ($\sigma = 100$ meV).



(d) 0.1-fix e/u.c. ($\sigma = 100$ meV).

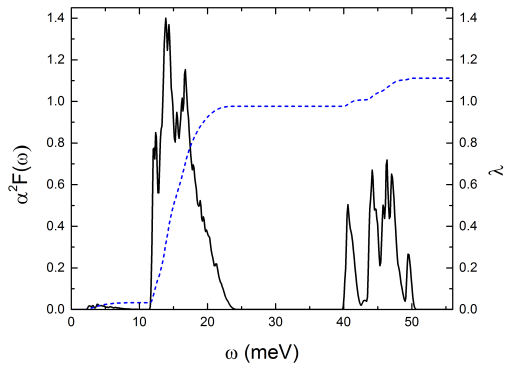


(e) 0.17 e/u.c. ($\sigma = 100$ meV).

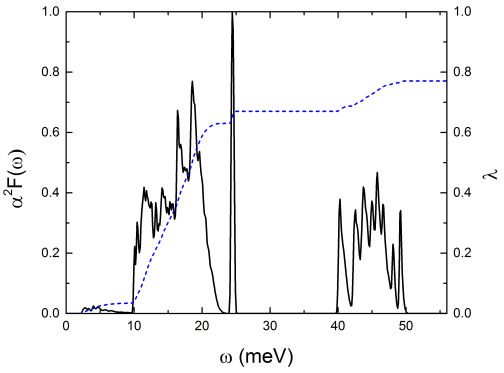


(f) 0.17-fix e/u.c. ($\sigma = 100$ meV).

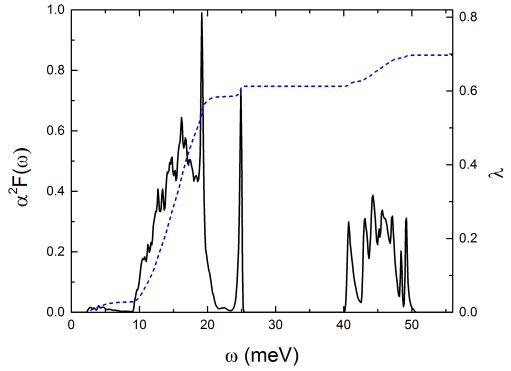
Figure 4.20: The isotropic Eliashberg spectral function, $\alpha^2F(\omega)$, for the jellium model doping (black lines). The cumulative contribution to the electron-phonon coupling, λ, is shown by the blue dashed line. The individual captions provide information on the doping levels. All six doping levels considered here have been calculated with an electronic smearing parameter of 0.1 eV.



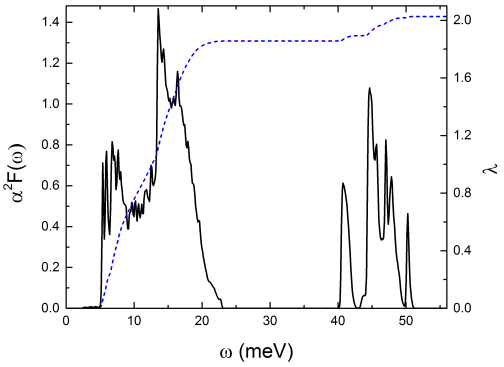
(a) 0.06 e/u.c. ($\sigma = 50$ meV).



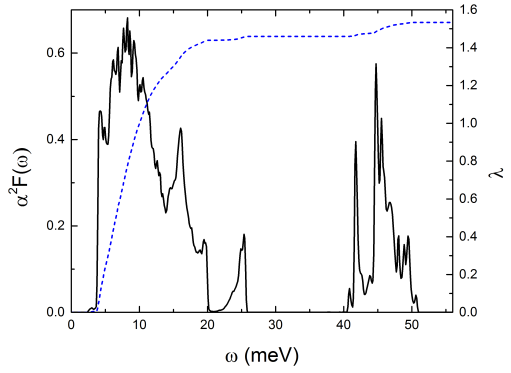
(b) 0.06-fix e/u.c. ($\sigma = 50$ meV).



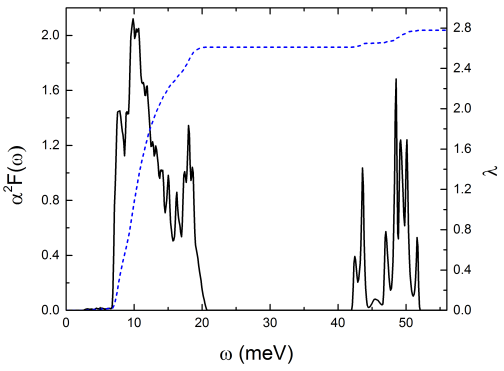
(c) 0.1 e/u.c. ($\sigma = 50$ meV).



(d) 0.1-fix e/u.c. ($\sigma = 50$ meV).

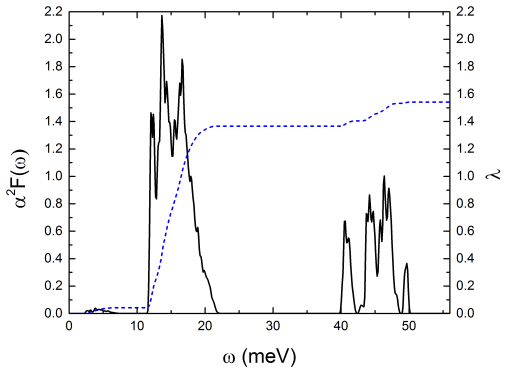


(e) 0.17 e/u.c. ($\sigma = 50$ meV).

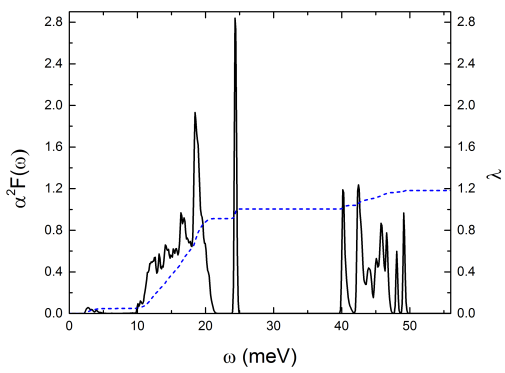


(f) 0.17-fix e/u.c. ($\sigma = 50$ meV).

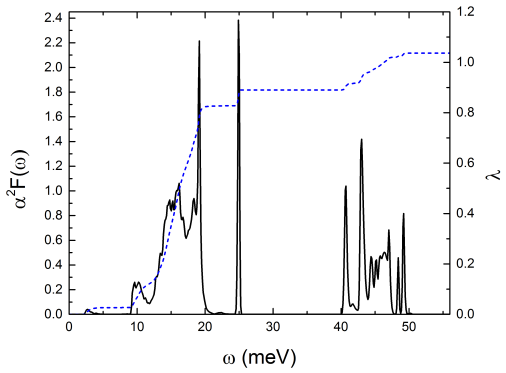
Figure 4.21: The isotropic Eliashberg spectral function, $\alpha^2F(\omega)$, for the jellium model doping (black lines). The cumulative contribution to the electron-phonon coupling, λ, is shown by the blue dashed line. The individual captions provide information on the doping levels. All six doping levels considered here have been calculated with an electronic smearing parameter of 0.05 eV.



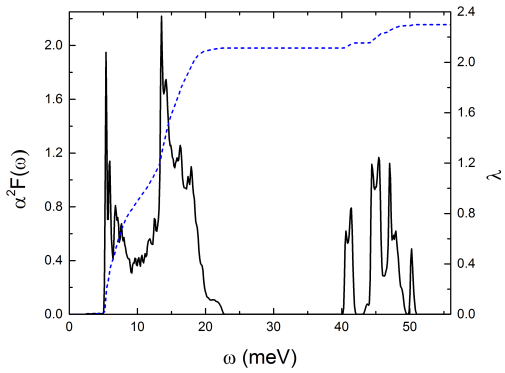
(a) 0.06 e/u.c. ($\sigma = 10$ meV).



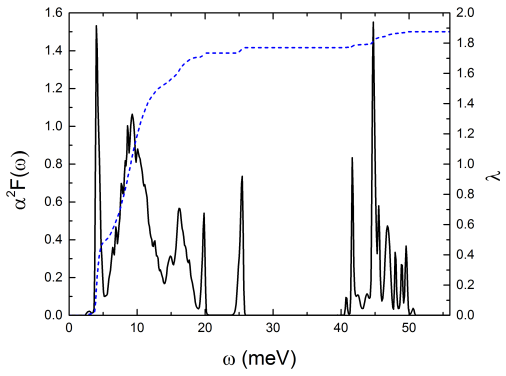
(b) 0.06-fix e/u.c. ($\sigma = 10$ meV).



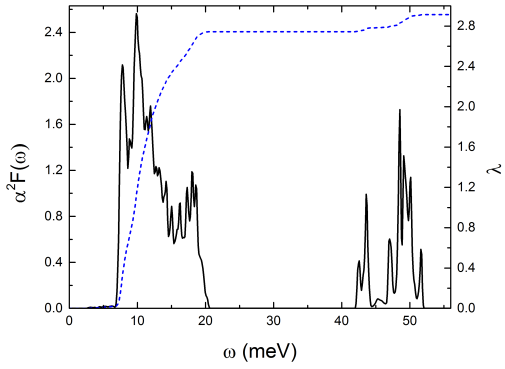
(c) 0.1 e/u.c. ($\sigma = 10$ meV).



(d) 0.1-fix e/u.c. ($\sigma = 10$ meV).



(e) 0.17 e/u.c. ($\sigma = 10$ meV).



(f) 0.17-fix e/u.c. ($\sigma = 10$ meV).

Figure 4.22: The isotropic Eliashberg spectral function, $\alpha^2F(\omega)$, for the jellium model doping (black lines). The cumulative contribution to the electron-phonon coupling, λ, is shown by the blue dashed line. The individual captions provide information on the doping levels. All six doping levels considered here have been calculated with an electronic smearing parameter of 0.01 eV.

level. This peak arises due to the coupling between electrons scattering from Q to Q' by phonons with $\mathbf{q} = K$. Due to the large softening at this wavevector in the phonon dispersion of the 0.06 e/u.c. doping level, this peak is now at the much lower energy of 14 meV. This enhances the electron-phonon coupling for this doping level.

The right-hand column of Figs. 4.20- 4.22 display the isotropic Eliashberg spectra and cumulative total electron-phonon coupling for the doping levels in which the lattice parameter has been fixed. An increase in the electron doping leads to an increase in the λ. However, unlike in the case of the rigid band model, this increase in the total electron-phonon interaction does not scale linearly with the density of states. As previously mentioned, the energetics of the K and Q minima in the lowest conduction band are different in the fixed lattice than in the relaxed unit cell, and increased electron doping leads to a lowering in energy of the Q minima. Thus, the Fermi sheets are of different sizes at the lowest doping level, leading to a lack of softening of the acoustic phonons at K and Q, and so a peak at 25 meV is present which is associated with the scattering between Fermi sheets at Q and Q' by $\mathbf{q} = K$ LA phonon modes. With increased doping, the isotropic Eliashberg spectrum reflects the softening of the phonons at the high symmetry points K, Q, and M, displaying intense peaks between 5-20 meV. The largest coupling is due to the LA phonon modes between 5-15 meV with phonon wavevectors $\mathbf{q} = M$.

The largest λ is thus obtained when the sizes of the Fermi surfaces at K and Q are similar. This induces Kohn anomalies in the LA and TA modes at K, M, and Q. These modes are important for intersheet scattering, and the λ increases further as the size of the Fermi sheets at K and Q increases. Neither the fixed lattice or relaxed cell jellium models produce the expected decrease in λ at high doping levels; however, it has been shown in the jellium model with a relaxed unit

cell that an increase in the doping level can lead to a decrease in λ.

4.6 Conclusion

In conclusion, the electronic structure of pristine 2H-MoS_2 and 1H-MoS_2 have been studied and compared favourably to both experiment and prior calculations. It is found that single-layer MoS_2 is a direct band gap semiconductor, in contrast to the bulk, which has an indirect band gap. The lattice dynamics of both bulk and monolayer have been investigated. These are very similar due to the weak interlayer bonding in 2H-MoS_2.

The effect of electron doping on the electron-phonon interaction in the monolayer has been studied using both a rigid band model and a jellium model. It was found that in the rigid band model additional electrons fill first the states near K and then a second minimum in the lowest energy conduction band at Q. This causes an increase in the density of states at the Fermi level, and when the second conduction band valley is filled, many additional scattering mechanisms become possible. The overall effect is thus an increase in the total e-ph coupling with increased doping. However, as the pristine band structure and lattice dynamics are used in this model, the effect of the extra charge on the electronic eigenvalues and phonon frequencies is not properly captured. As a result, a jellium model was used for both fixed lattice constants and optimised geometry. It was found that this choice of lattice parameter has a profound effect on the character of the lowest energy conduction band, and thus on which additional states were filled. In the case where the lattice constant was allowed to increase upon adding electrons in the unit cell, it was found that the additional charge filled states near the K point, leaving only a small Fermi sheet at Q. The phonon dispersions displayed a large

softening at the M point of the LA modes. These modes greatly contribute to the coupling, leading to large values for the total electron-phonon coupling constant. The jellium model with fixed lattice parameters resulted in even larger total λ. This is because, as additional electrons were added to the unit cell, the Q valley of the lowest conduction band decreased in energy, leading to a Fermi surface where valleys at K and Q are filled equally. The resulting phonon dispersions show large softening of the LA and TA modes, not only the M point but also at Q and K. These modes also contribute to the electron-phonon coupling, resulting in an even larger λ.

Chapter 5

Phonon Mediated Superconductivity in Electron Doped Monolayer MoS2

5.1 Introduction

It has long been known that bulk MoS_2 can be easily metallised by the insertion of alkali or alkaline earth metals between adjacent trilayers [198]. Upon cooling many of these intercalated compounds become superconducting, with a maximum T_c=6.9 K discovered in $Rb_{0.3}MoS_2$ [199]. More Recently, the use of electric double layer transistors have emerged as a very promising technique for controlling the electrostatic carrier doping in solids [72]. Using this technique to fine-tune the carrier density in few-layer flakes of MoS_2, a dome-shaped superconductive region has been discovered in the temperature-carrier concentration phase diagram [44]. The superconductive state appears sharply for doping concentrations higher than n_{2D}=6×10^{14} cm^{-2}. At the optimal doping concentration a maximum

critical temperature of 10.8 K is attained. Slightly higher carrier densities up to $n_{2D} = 1.5 \times 10^{14}$ cm^{-2} result in a decrease in the T_c. It has been suggested that, while liquid-gating cannot achieve doping levels comparable to the intercalated bulk compounds, the phase diagram might be expanded to higher concentration levels by including the data from these compounds [44]. This results in the phase diagram reproduced in Fig. 1.3 from Ref. [44].

Although current studies of the superconductive state in liquid-gated MoS_2 have focused on flakes with multiple layers, it has been been suggested that the superconducting state is quasi-two dimensional in character [69]. The carriers are expected to be concentrated only in the top layer, making the comparison with the 1H-MoS_2 valid.

The aim of this chapter is to study the evolution of the superconductive state with carrier density. By modelling the doping with a jellium model, it is hoped that the trend in the superconducting transition temperature as a function of electron doping shown in Fig. 1.3 can be explained. In order to do so the same three doping levels as discussed in the previous chapter, 0.06 e/u.c., 0.1 e/u.c., and 0.17 e/u.c., will be studied. This covers the carrier concentrations found experimentally, from the onset of the superconductive state to the carrier density at the peak T_c, as well as a higher doping level which is still within the range achievable by liquid electrolyte gating.

The chapter is organised as follows; First the details of the calculations presented in this chapter will be explained. Estimates of the superconducting transition temperature will then be made using increasingly sophisticated methods, from the commonly used Allen-Dynes formula to solving the Eliashberg equations using the isotropic average of the Eliashberg function, to inclusion of the anisotropy of the system via the solution of the fully anisotropic Eliashberg equations [128]. Both the

temperature and **k**-point dependence of the superconducting gap will be examined. Finally the effects of Coulomb repulsion will be discussed.

5.2 Heavily Electron Doped MoS_2

By using an electric double layer transistor doping levels of up to $n_{2D} = 3 \times 10^{14}$ cm^{-2} have been observed in few-layer MoS_2 [69]. This is still a significantly lower carrier concentration than is found in intercalated bulk compounds, which typically have carrier densities of $n_{2D} \sim 4 - 8 \times 10^{14}$ cm^{-2} as seen in Fig. 1.3. The question of whether it is correct to connect the two different methods of metallising MoS_2, chemical doping and liquid-gating, is thus open to debate. In DFT calculations there should in principle be no such limitations in the range of carrier concentrations which can be investigated. It was therefore decided to examine the electron-phonon interaction and, by extension, superconducting properties of heavily electron doped 1H-MoS_2. A unit cell containing an additional 0.3 electrons was used to simulate an effective carrier concentration of $n_{2D} \sim 4 \times 10^{14}$ cm^{-2}. Regardless of whether the in-plane lattice parameter, a, was fixed at the fully optimised pristine value of 3.132 Å or was relaxed until the pressure in the unit cell was less than 0.5 kbar, it was found that the electronic structure of 0.3 e/u.c. displayed a strong sensitivity to the extent of the vacuum region between periodic images.

Fig. 5.1 shows a comparison between the band structure of the system with 0.3 e/u.c. with different interlude spacings. It can be seen that with increased interlayer spacing parabolic free electron states in the conduction band are lowered in energy, while the remaining bands, which correspond to those found in the band structures of pristine MoS_2 remain unchanged. This is important since, as it can

be seen in Fig. 5.1, the size of the the interlayer spacing will therefore determine which bands the additional doping electrons will fill. This spurious dependence of the interlayer spacing has been observed in heavily electron doped graphene, silicene, and germanene, and can be explained in terms of the (x, y)-plane-averaged self-consistent field electronic potential along the z-direction, $\bar{V}(z)$ [200, 201]. In the case of undoped calculations $\bar{V}(z)$ dips sharply at the atomic layers and rises back to the vacuum potential at which point it remains flat. In the cases of two-dimensional graphene, silicene, germanene, and now MoS_2, it is found that when there are extra electrons present in the unit cell, $\bar{V}(z)$ reaches the vacuum potential near the monolayer and then tends towards $-\infty$ as $z \to \pm\infty$. This is shown schematically in Fig. 5.2. Within periodic boundary conditions the potential therefore displays a dip reminiscent of a quantum well in the midst of the vacuum. By solving the Kohn-Sham Hamiltonian using plane waves, solutions can be found in this quantum well which are localised along the z-direction but free-electron-like in the plane of the MoS_2 layer [200]. The width of the barrier w seen in Fig. 5.2 decreases with increasing negative charge, and so higher doping levels are more likely to lead to solutions in the quantum well. The depth of the well is clearly dependent on the size of the interlayer spacing, s, and so for larger interlayer spacings these 2D free-electron-like bands are found at lower energies. For sufficiently large values of s, these parabolic bands fall below the Fermi energy, and so the excess electrons are spilled into the vacuum region. The amount of electrons in the vacuum will thus increase with interlayer spacing and doping level. It was found that, by increasing the vacuum region for the lighter-doped cases of 0.06, 0.10 and 0.17 electrons per unit cell to between 16 Å and 25 Å nearly-free electron (NFE) bands appear around the Fermi level. Thus, in order to study the case of heavily doped 1H-MoS_2, the interlayer spacing must be reduced so that these spurious

bands do not interfere with the calculations.

In practice this means that the nearly-free electron bands must be higher in energy than the 5 lowest-energy conduction bands, so that MLWFs can be used in the calculation of the electron-phonon properties via the EPW code. It was determined that the largest interlayer spacing which would have the nearly-free electron bands at energies high enough above the conduction band minimum for this to work was ~ 5 Å. At this interlayer spacing the periodic images interact with each other so it is not possible to obtain correct phonon frequencies. Even with a sensible interlayer spacings, large enough to prevent unphysical interactions between periodic cells, it was found that the phonon frequencies for the LA mode become imaginary at the K point, suggesting an instability in heavily-doped 1H-MoS_2. It should be noted that the dependence of the interlayer spacing on the electronic structure of single-layer MoS_2 can be avoided altogether by use of a localised orbitals basis set. In this case the spurious quantum well like structure in the vacuum will not effect the solutions of the electronic Hamiltonian as there is no basis set so far away from an atomic site. For the work in this thesis it was deemed sufficient to study the three carrier concentrations outlined above rather than move to a localised orbital basis set as was done in the case of 2D silicene and germanene [200]. In the case of monolayer MoS_2 the appearance of the unphysical nearly-free electron bands at the Fermi level for interlayer spacings of $\sim$15 Å which are so commonly used in the literature, is particularly unfortunate as it coincides with the optimal carrier concentration for T_c. Thus the results of Refs. [202] and [203] where a large dependence of the conduction band at Γ on carrier concentration is found to explain the drop T_c beyond the optimal doping level, in good agreement with experiment, it is most likely the spurious effect of excess charge filling the NFE states.

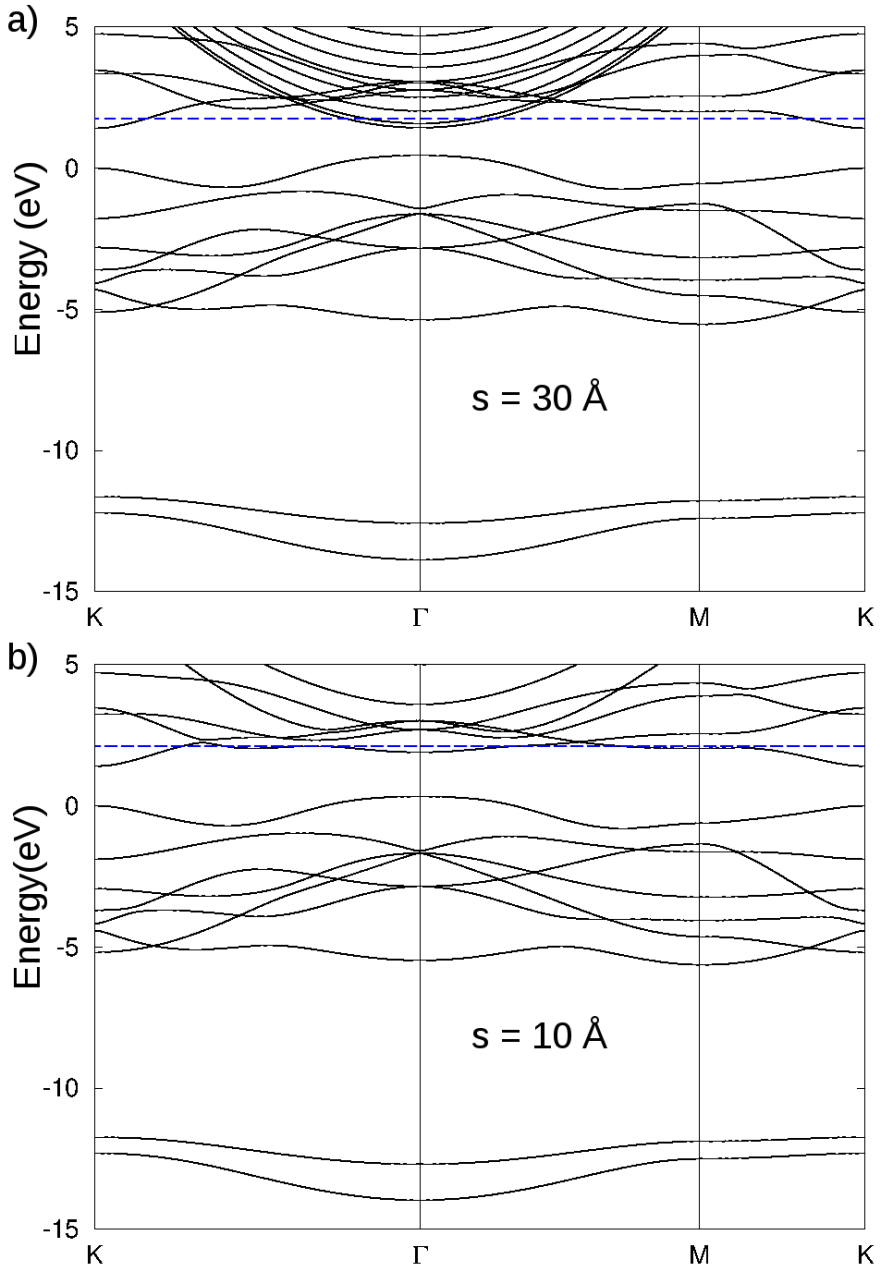


Figure 5.1: The electronic band structures of MoS_2 doped with 0.3 e/u.c. when a) the interlayer spacing is 30 Å and b) is 10 ÅIt can be clearly seen in the conduction band at Γ that unphysical nearly-free-electrons bands appear in both cases. However an increase in the interlayer spacing, s, results in these parabolic bands shifting to lower energies and falling below the Fermi level. The energy axis is set so that the valence band maximum is 0 eV. The Fermi levels are indicated by the dashed lines.

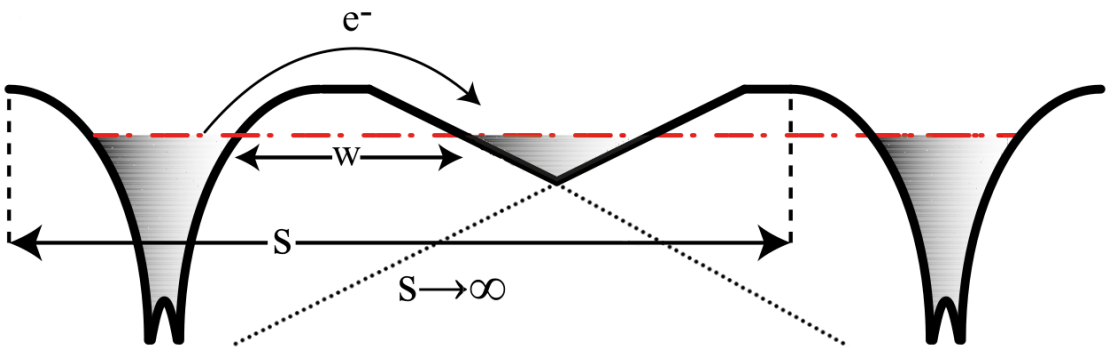


Figure 5.2: A schematic explanation of the NFE bands which appear in heavily doped two-dimensional materials when plane waves and periodic boundary conditions are used. Adapted from [200].

5.3 Calculation Details

In order to self-consistently solve both the anisotropic and isotropic Eliashberg equations on the imaginary axis and by analytic continuation onto the real axis as in Eqs. (3.84), (3.83), (3.74), (3.73), it is important to have an accurate description of the e-ph coupling near the Fermi surface. This requires, as in the previous chapter, the calculation of the electronic eigenvalues, phonon frequencies, and electron-phonon matrix elements for a very large number of electron and phonon wavevectors in the Brillouin zone. The most computationally efficient manner in which to obtain such quantities is via Wannier interpolation as implemented in the EPW code. Therefore the same pseudopotentials, kinetic energy cutoff and coarse grids for the **k**-point and **q**-point sampling were used as in the previous chapter. However, in order to evaluate the Eliashberg equations it is necessary in a practical calculation to write to file the electron-phonon matrix elements for the interpolated grids. It is also necessary to perform sums over $\mathbf{k}'$ in Eqs. (3.84), (3.83), (3.74), (3.73) over the entire Brillouin zone. These considerations mean that the interpolated grids are chosen to be uniform and zone centred. These meshes are also chosen to be commensurate, so that the final state $\mathbf{k}'$ maps onto

the same initial fine **k**-point grid as $\mathbf{q} = \mathbf{k}' - \mathbf{k}$. For these reasons interpolated uniform Γ-centred grids of 200×200×1 were used for both the electron and phonon wavevectors. The sensitivity of these grids on the momentum dependence of the superconducting gap was investigated for a number of different temperatures and grid sizes. It was found that, at variance with the convergence of λ in the previous chapter, in this case the density of the phonon meshes must be comparable to that of the electronic grid. Fig. 5.3 show the comparison of the energy distribution of the superconducting gap for one particular doping level at one temperature, for grids of $100\times100\times1$ and $200\times200\times1$. It can be seen that there is a good agreement in this energy distribution, suggesting that convergence has been achieved. Ideally even larger grids would need to be examined, however this was not possible due to the computational cost of these calculations. The Dirac delta functions were replaced by a smearing parameter of 50 meV for the electrons and 0.5 meV for the phonons.

For the iterative solution of the Eliashberg equations on the imaginary axis, an initial guess is made for the superconducting gap, corresponding to a step function in the imaginary axis. The Allen-Dynes equation provides a simple method for estimating the T_c from the calculated λ:

$$T_c = \frac{\omega_{\log}}{1.2}\exp\left[\frac{-1.04\,(1+\lambda)}{\lambda-\mu^*\,(1+0.62\lambda)}\right], \tag{5.1}$$

where $\omega_{\log} = \exp[2/\lambda \int d\omega\alpha^2F(\omega)\log(\omega)/\omega]$. Thus, by using the BCS formula $2\Delta_0(i\omega_n)/T_c = 3.52$, an estimation for the magnitude of the superconducting gap at zero temperature can be made. This is in turn can be used as the starting guess for $\Delta_0(i\omega_n)$ for Matsubara frequencies below twice the largest phonon frequency of the material, $2\omega_{\max}$. If in a calculation the superconducting gap is being evaluated

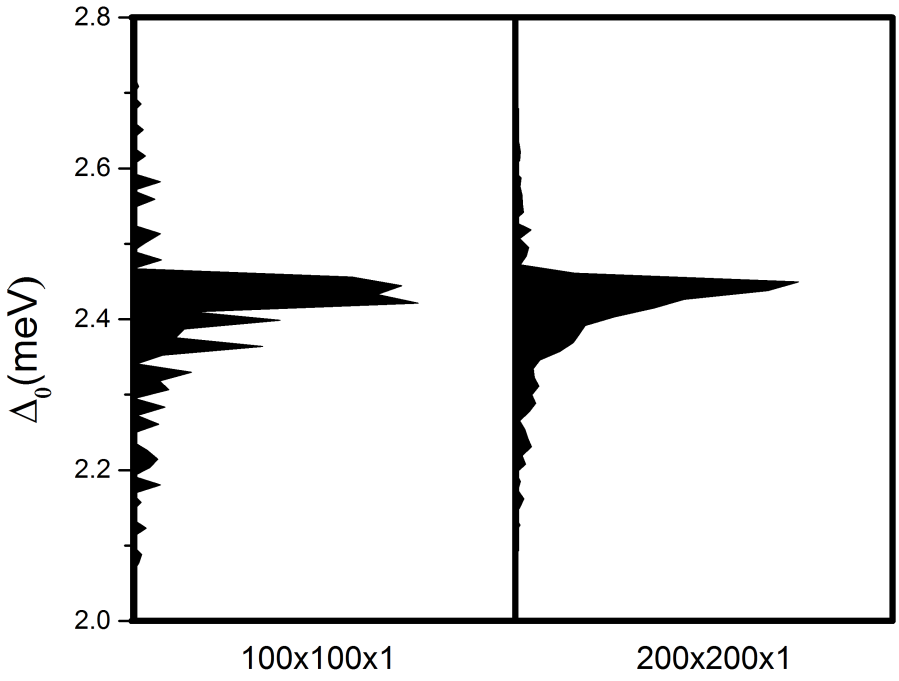


Figure 5.3: The energy dependence of the superconducting gap is compared for a doping level of 0.06-fix e/u.c. with **k**-point and **q**-point grids of 100x100x1 and 200x200x1.

for more than one temperature, then the gap function just calculated is used as the initial guess for the next temperature. The convergence of the iterative solution of the imaginary axis Eliashberg equations was considered complete when the relative difference in self-consistent steps was less than 1×10^{-4}. The number of iterations to achieve convergence increases substantially as $T \to T_c$, from approximately 15-20 iterations for $T \lesssim T_c$, to over 100 for $T \gtrsim T_c$.

The cutoff for the number of imaginary frequencies required for the calculation of the superconducting gap on the imaginary axis was set to ten times the largest phonon frequency [147]. However, as the temperature increases, the number of Matsubara frequencies decreases as $i\omega_n = i(2n+1)\pi T$. Therefore at large T fewer

frequencies are used in the evaluation of $\Delta_0(i\omega_n)$ as compared to low temperature. As a result the calculated gap is less accurate. In order to address this concern it was decided to set the number of Matsubara frequencies rather than the frequency cutoff. This number was set with reference to the cutoff calculated for $T = 4$ K. This lead to 180 imaginary frequencies being used for all temperatures considered.

5.4 Isotropic Eliashberg Equations

The accuracy of the Padé functions for the continuation of the calculated superconducting gap to the real axis was tested by comparison to the exact iterative analytic continuation for the *isotropic* Eliashberg equations. As the Padé method is far less computationally demanding it is advantageous so long as the solution can be relied upon. In solving the *anisotropic* Eliashberg equations the iterative method is so computationally intensive that it was not possible to find a real axis solution in this manner. Fig. 5.4 shows the isotropic average of the superconducting gap calculated as a function of temperature. In this case the doping level is 0.06 e/u.c. and the Coulomb parameter is set to $\mu_c^* = 0.07$, however the validity of the Padé method holds for all doping levels and Coulomb parameters. The accuracy to which the Padé approximation matches the exact analytic continuation justifies the use of the Padé method, and suggests that it is valid for finding real axis solutions from the imaginary axis solutions to the anisotropic Eliashberg equations. Fig 5.5 shows the energy dependence of the real part of the superconducting gap along the real axis, for both the Padé method and exact iterative solution. It can be seen that they are in good agreement although some of the fine features in the exact solution are missed by the Padé method. The peaks which occur below ~ 55 meV correlate with the peaks found in the Eliashberg spectral function (Fig. 4.21c).

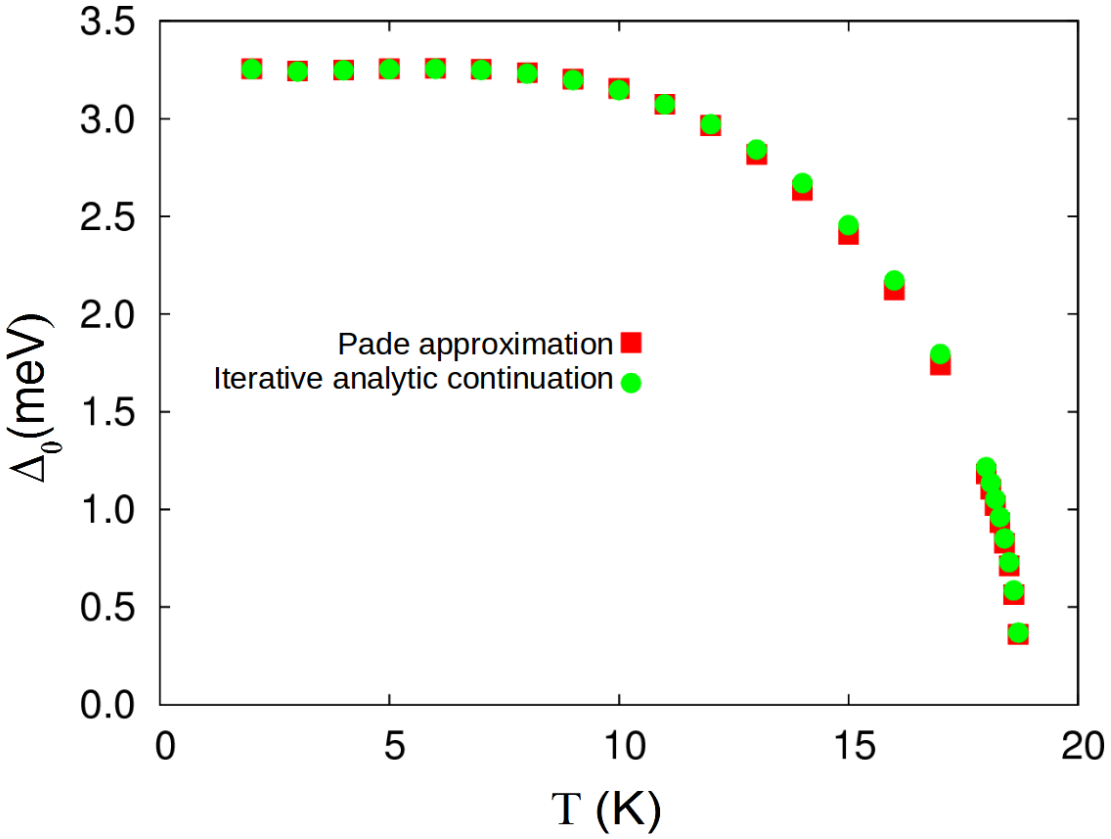


Figure 5.4: The calculated isotropic average of the superconducting gap of monolayer MoS_2 doped with 0.06 e/u.c. as a function of temperature. The green circles have been calculated on the imaginary axis and analytically continued onto the real axis by use of an iterative exact continuation, while the red squares used a Padé approximation [147]. It can be seen that both methods produce very similar results.

The normalised quasiparticle density of states of 1H-MoS_2 was calculated using Eq. (3.90) and is shown in Fig. 5.6, for a doping level of 0.06 e/u.c., μ_c^*=0.07, and $T = 2$ K. This quantity is precisely what is measured by tunnelling experiments, and a gap of 3.2 meV is clearly visible from the van Hove singularity in the DOS [204]. The deviations from unity in the range 10-55 meV are due to the peaks in the Eliashberg function, and provide the information needed for the extraction of $\alpha^2F(\omega)$ from experiment. The isotropic average of the superconducting gap at the Fermi surface is shown as a function of temperature for the full range

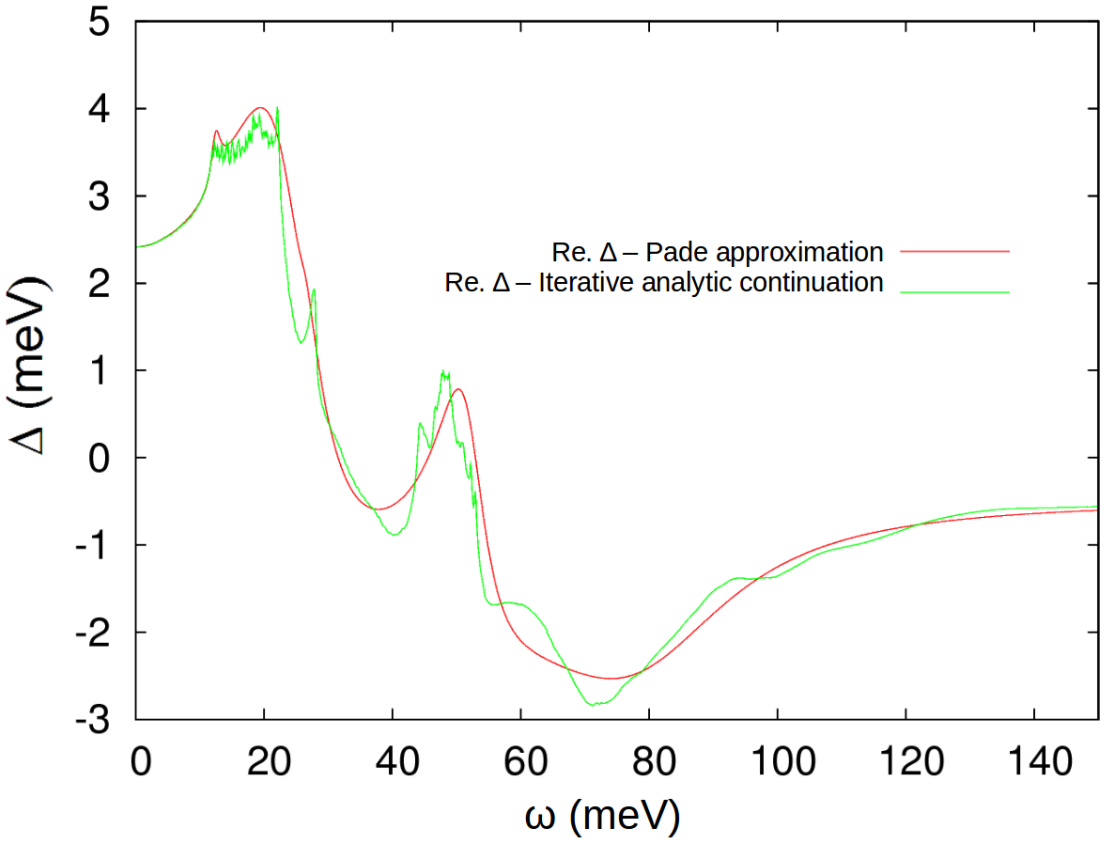


Figure 5.5: The real part of the superconducting gap along the real energy axis, obtained both via an iterative analytic continuation (green line), and the less computationally demanding Padé approximation (red line). The plot corresponds to a doping level of 0.1 e/u.c..

of dopings considered in Figs. 5.7a-5.9b by the blue circles, for the case $\mu_c^* = 0.07$. The isotropic T_c as well as the λ and superconducting gap function at $T = 0$ K are summarised in Table 5.1.

In the case of the relaxed-cell jellium model, it can be seen in Fig. 5.7a that the critical temperature obtained from the isotropic Eliashberg gap equations for the lowest doping level of 0.06 e/u.c. is 18.7 K. This is the temperature at which the superconducting gap vanishes. As the doping level is increased to 0.1 e/u.c. the critical transition temperature decreases to 13.2 K. This can be explained by the decrease in the λ at this doping level as discussed in Chapter 4. For the highest

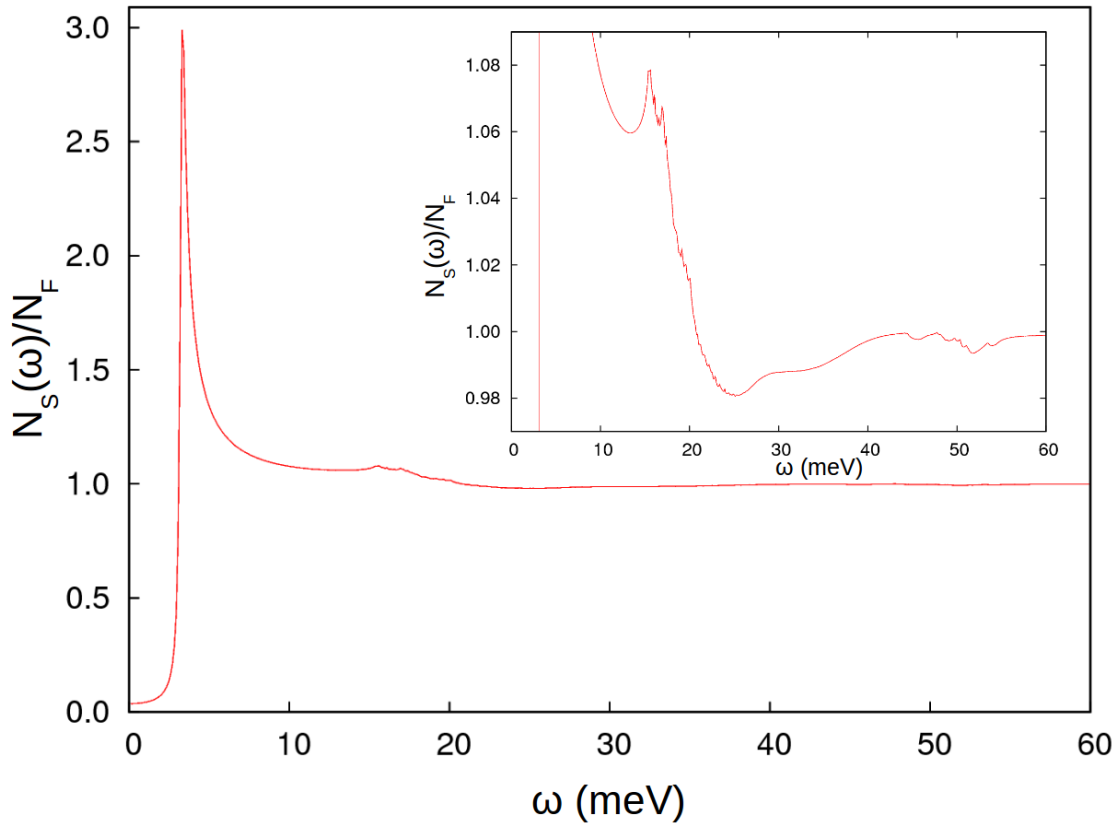


Figure 5.6: The calculated quasiparticle density of states of monolayer MoS_2 doped with 0.06 e/u.c. The insert shows the same quantity magnified in order to show the structure which is used to extract the Eliashberg spectral function in tunnelling experiments.

doping level considered in the optimised unit cell jellium model, 0.17 e/u.c, the $T_c = 19.4$ K. This is the highest T_c obtained in the relaxed cell, however, considering that the λ is twice as large at this doping level compared to the other two doping levels it is perhaps surprising that the T_c is not higher. The explanation is that the increased phonon softening with increased doping, especially at the high symmetry point M, (as discussed in Chapter 4) causes the logarithmic average of the phonon frequencies to be much smaller. The competing effects of the larger λ and lower $\omega_{\log}$ result in the 0.17 e/u.c. doping level having a very similar isotropic T_c as the lower doping of 0.06 e/u.c.

	Optimised cell			Fixed cell		
	0.06	0.1	0.17	0.06-fix	0.1-fix	0.17-fix
λ	1.04	0.85	1.98	0.84	1.88	2.71
N_F (states/spin/eV)	0.96	0.69	0.76	0.75	1.12	1.18
$\omega_{\log}$ (meV)	16.6	16.3	8.8	16.8	12.3	11.3
T_c (K) (Allen-Dynes)	16.1	11.9	15.6	12.0	21.0	23.7
$\Delta_0(T=0)$ (meV)	3.2	2.2	3.7	2.2	5.4	7.2
T_c (K) (Isotropic)	18.7	13.2	19.4	13.8	27.0	32.5

Table 5.1: The calculated total electron-phonon coupling constant λ, isotropic superconducting gaps Δ_0(T= 0), and isotropic critical transition temperatures T_c for the doping levels considered in both the optimised cell and fixed cell jellium models. The T_c as calculated by the Allen-Dynes equation (Eq. 5.1) is also included, as are the density of states at the Fermi level and the logarithmic average of the phonon frequencies. All values are for the case $\mu^* = 0.07$ although the effect of μ^* is shown in Fig 5.10.

The trend for the isotropic gaps with increased carrier concentration for the fixed lattice parameters is quite different. For the lowest doping level the isotropic T_c is calculated as 13.8 K. By increasing the electron-doping it is found that the T_c increases dramatically to 27 K. Upon further doping the isotropic T_c further increases to a value of 32.5 K for the 0.17-fix e/u.c. doping level.

5.5 Anisotropic Eliashberg Equations

Figs. 5.7-5.9 display the energy dependence of the anisotropic superconducting gap across the Fermi surface as a function of temperature. The **k**-dependence of the superconducting gap on the Fermi surface is also displayed at each doping level. The black dashed line is a fit obtained using the BCS gap equation:

$$\frac{1}{\lambda} = \int_0^{\omega_D} \tanh\frac{\sqrt{\Delta^2+\omega^2}}{2k_BT}\frac{d\omega}{\sqrt{\Delta^2+\omega^2}}, \tag{5.2}$$

with Δ being the calculated gap at $T = 0$ K. In an ideal BCS superconductor, the ratio $2\Delta_0/k_BT_c$ is equal to 3.53 and so it can be used to measure the deviation from this behaviour. Table. 5.2 displays this ratio for all the different doping levels considered in this chapter.

In terms of the evolution of T_c as a function of electron doping, the trend is very similar as those found in the isotropic case. In the case of the relaxed cell at the lowest doping of 0.06 e/u.c. the calculated $T_c = 22.9$ K. This is significantly larger than the calculated isotropic value for T_c of 18.7 K. In the anisotropic case, there is a wide spread in the energies of the superconducting gap. This is known to lead to higher critical temperatures than in the isotropic case as is seen in multigap superconductors such as MgB_2 [147, 201]. In fact, our anisotropic Eliashberg calculations demonstrate that monolayer MoS_2 can be thought of as having two different superconducting gaps from two different Fermi sheets. However, the superconducting gaps found at the Fermi sheets at K and Q are very similar in energy and so it appears that there is only one gap. The anisotropy of the gaps can be calculated as the ratio of the energy spread of the gap to the average superconducting gap as $(\Delta_0^{\max} - \Delta_0^{\min})/\Delta_0^{\text{ave}}$. The anisotropy ratios for both the gap at K and at Q are summarised along with the critical temperature $T_c(\mu^* = 0.07)$ in Table. 5.2. In the case of the 0.06 e/u.c. doping level in the relaxed cell, it is found that the anisotropy of the gaps at both K and Q are very similar, 19.5% and 20.2% respectively. This is in keeping with the explanation in the previous chapter that at this doping level the Fermi sheets at K and Q are very similar causing, large nesting which leads to Kohn anomalies at K, Q, and M phonon wavevectors. The large nesting at the doping level causes a large λ which is responsible for the high T_c.

As the doping increases, the T_c at the higher doping level of 0.1 e/u.c. is

	Optimised cell			Fixed cell		
	0.06	0.1	0.17	0.06-fix	0.1-fix	0.17-fix
λ	1.04	0.85	1.98	0.84	1.88	2.71
T_c (K)	22.9	13.5	20.1	15.0	30.3	34.3
Δ_0^{ave} at K (meV)	3.82	1.99	3.71	2.33	6.31	7.74
Δ_0^{ave} at Q (meV)	3.82	2.16	3.95	2.36	5.81	7.21
Anisotropy at K (%)	19.5	37.4	34.3	42.4	17.3	6.1
Anisotropy at Q (%)	20.2	4.8	7.3	10.2	15.6	11.3
$2\Delta/k_BT_c$ at K	3.87	3.42	4.28	3.61	4.83	5.24
$2\Delta/k_BT_c$ at Q	3.87	3.71	4.56	3.65	4.45	4.88

Table 5.2: A summary of the T_cs calculated by solving the fully anisotropic Eliashberg gap equations. The anisotropy of the superconducting gap at K and Q are also presented using the ratio defined as $(\Delta_0^{\text{max}} - \Delta_0^{\text{min}})/\Delta_0^{\text{ave}}$. The ratio $2\Delta/k_BT_c$ is useful for comparing to ideal BCS behaviour for which a value of 3.53 would be obtained.

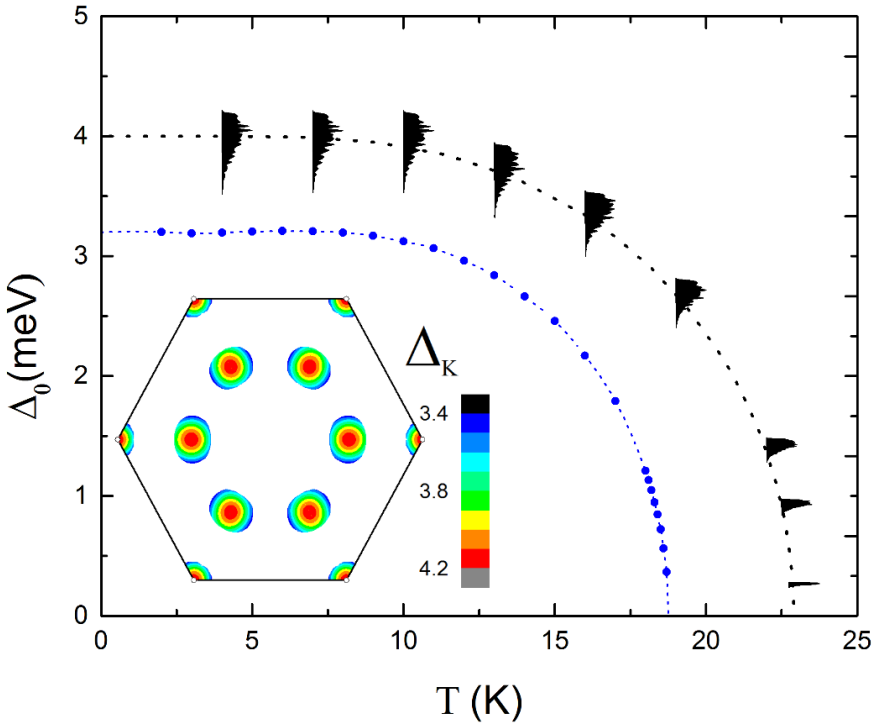
actually lower at 13.5 K, than the T_c of the 0.06 e/u.c. doping level. This can be explained by the smaller λ, as in the isotropic case. What is more interesting is that at this doping level the isotropic and anisotropic calculated T_c's are very similar, in contrast to the lower doping level. If the anisotropy ratios for the K and Q gaps are calculated, it is found that they are very different, 37.4 % and 4.8 % respectively. This indicates that the superconducting gap at K, while of a similar magnitude, is much more anisotropic than the gap at Q. The high degree of anisotropy in the gap at K does not result in a much larger T_c in the anisotropic case versus the isotropic case. It is therefore thought that the gap at Q is more important in determining the enhancement of T_c by anisotropy. This is confirmed by noting that the differences in the T_c in the isotropic and anisotropic calculations correlates very well with the anisotropy ratio of the superconducting gap at Q but not at all with the superconducting gap at K.

For the largest doping level considered in the relaxed cell jellium model, solving the anisotropic Eliashberg equations results in a calculated $T_c = 20.1$ K. Unlike in

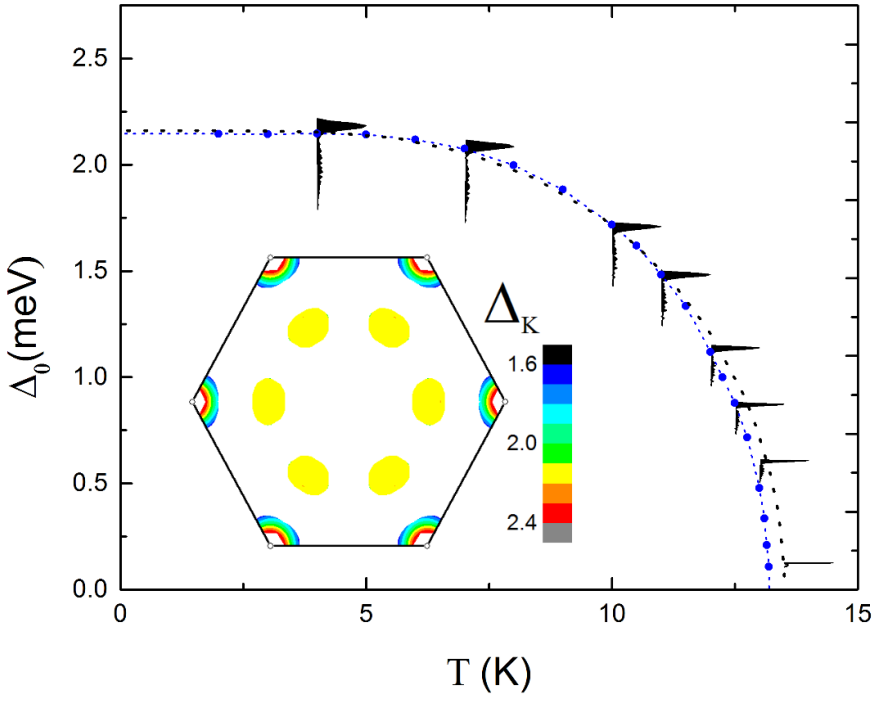
the isotropic case, this is lower than the T_c at the lowest doping level of 0.06 e/u.c. The explanation is that the superconducting gap at Q is much less anisotropic (7.3 % vs 20.2%) at this doping level and so does not enhance the T_c as greatly as in the 0.06 e/u.c. doping level.

In the fixed cell jellium model the T_c increases with increasing doping as in a similar manner to the isotropic calculation. It can be seen in Table. 5.2 that the two largest doping levels have superconducting gaps which are similarly anisotropic, while for the lowest doping level the anisotropy of the gap at K is much larger than that at Q. This is further evidence that the Fermi surfaces are more similar at these doping levels, which leads to larger values for λ as discussed in the previous chapter. This also results in larger T_c in correspondence of higher electron doping.

As expected, the deviation from the standard BCS behaviour is largest when the total electron-phonon coupling is very large, ie. $\lambda \sim 2$. This is because the BCS gap equation only holds for weak-coupling. In fact, the coupling is so large in the 0.17-fix e/u.c. doping level, that it is possible that Migdal's theory, which states that higher order corrections to the electron-phonon interaction can be ignored, is no longer valid [124]. Therefore the results at this doping level should be regarded tentatively as it is possible that they are not reliable.

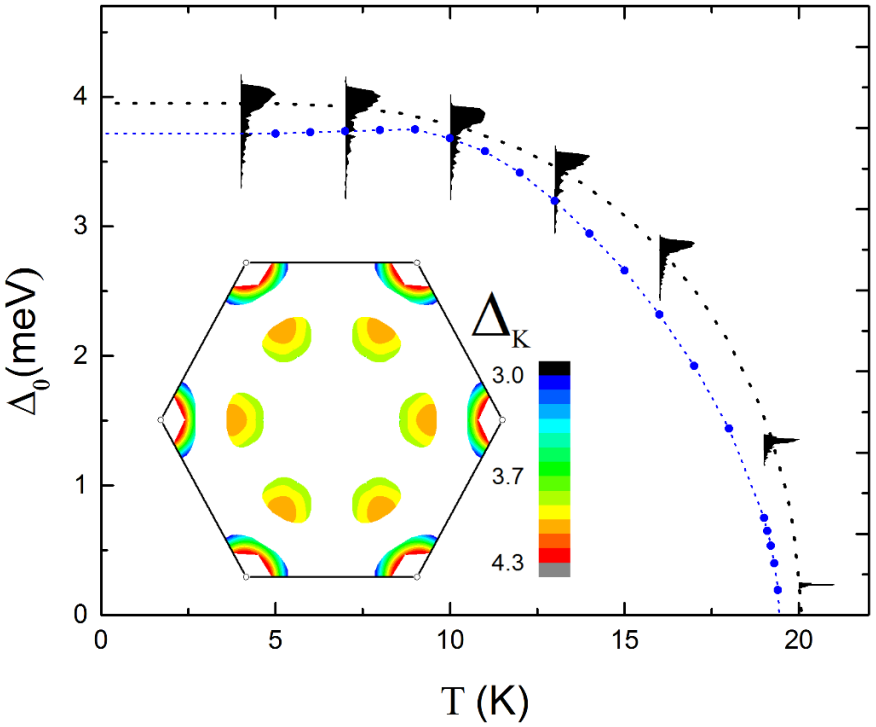


(a) 0.06 e/u.c.

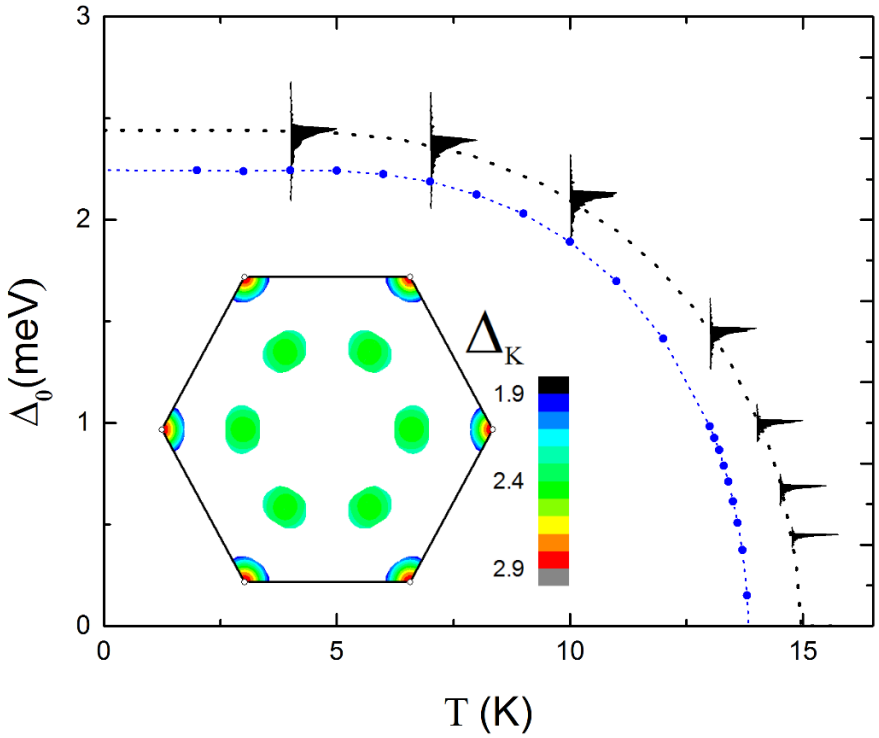


(b) 0.1 e/u.c.

Figure 5.7: The energy of the superconducting gap as a function of temperature for the jellium model with relaxed unit cell. The gaps calculated using the isotropic Eliashberg equations are shown as blue circles, and the dashed line is a guide for the eye. The energy distribution of the superconducting gaps at various temperatures as calculated from the anisotropic Eliashberg equations are shown in black. The black dashed line are fits to the BCS gap equation using the calculated data. The calculated momentum-resolved superconducting gap at zero temperature on the Fermi surface is displayed in the insert.

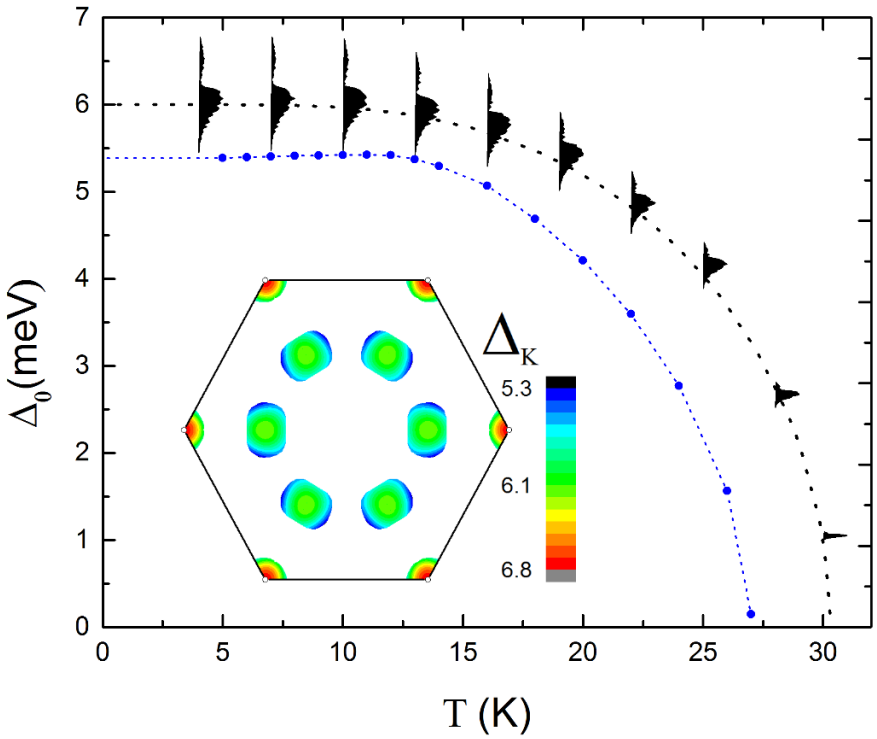


(a) 0.17 e/u.c.

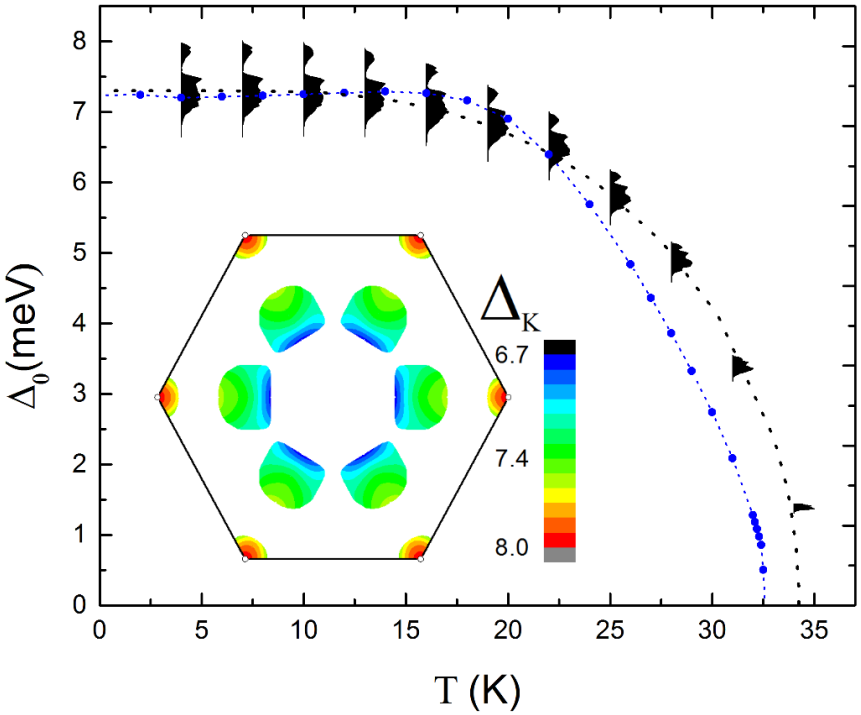


(b) 0.06-fix e/u.c.

Figure 5.8: The energy of the superconducting gap as a function of temperature for the jellium model with relaxed unit cell and jellium model with a fixed unit cell. The key is that same as that used in Fig. 5.7.



(a) 0.1-fix e/u.c.



(b) 0.17-fix e/u.c.

Figure 5.9: The energy of the superconducting gap as a function of temperature for the jellium model with a fixed unit cell. The key is that same as that used in Fig. 5.7.

5.6 Coulomb Interaction

So far all the results discussed in this chapter relate to the case where the Coulomb interaction between electrons have been incorporated by a static parameter $\mu^* = 0.07$. However it is known that this parameter can be as large as $\mu^* \sim 0.2 - 0.3$. As such it was decided to investigate the effect of the Coulomb pseudopotential on the critical temperature. Fig. 5.10 shows the dependence of the critical transition temperature when calculated using the Allen-Dynes formula, isotropic Migdal-Eliashberg theory, and anisotropic Migdal-Eliashberg theory, for the 0.06 e/u.c. doping level. It can be seen that, due to the large electron-phonon coupling $\lambda \sim 1$, T_c does not vary as strongly with μ^* as might be expected. The results show that as long as a sensible value for μ^* is used, the calculated T_c is of the same order of magnitude as the experimental value, even if it is overestimated by a factor of about 3. This overestimation of the critical transition temperature is not unexpected as in our calculation the doping is described using a highly idealised model. It is also expected that a better qualitative agreement with experiment may be found by use of a doping-dependent $\mu^*(x)$, in order to reflect the change in the Coulomb interaction when additional electrons are added to the system.

5.7 Comparison to Experiment

It is known from experiment that in gate-doped thin flakes of MoS_2 there is a dome-shaped superconductive region in the carrier concentration vs. T_c phase diagram [44]. Our results for the calculated T_c do not show a decrease at large dopings or a disappearance of the superconducting state even for large values of μ^*. The question therefore is how to reconcile our results with those of the experiment. In order to answer this it is useful to consider four regions of the experimental phase

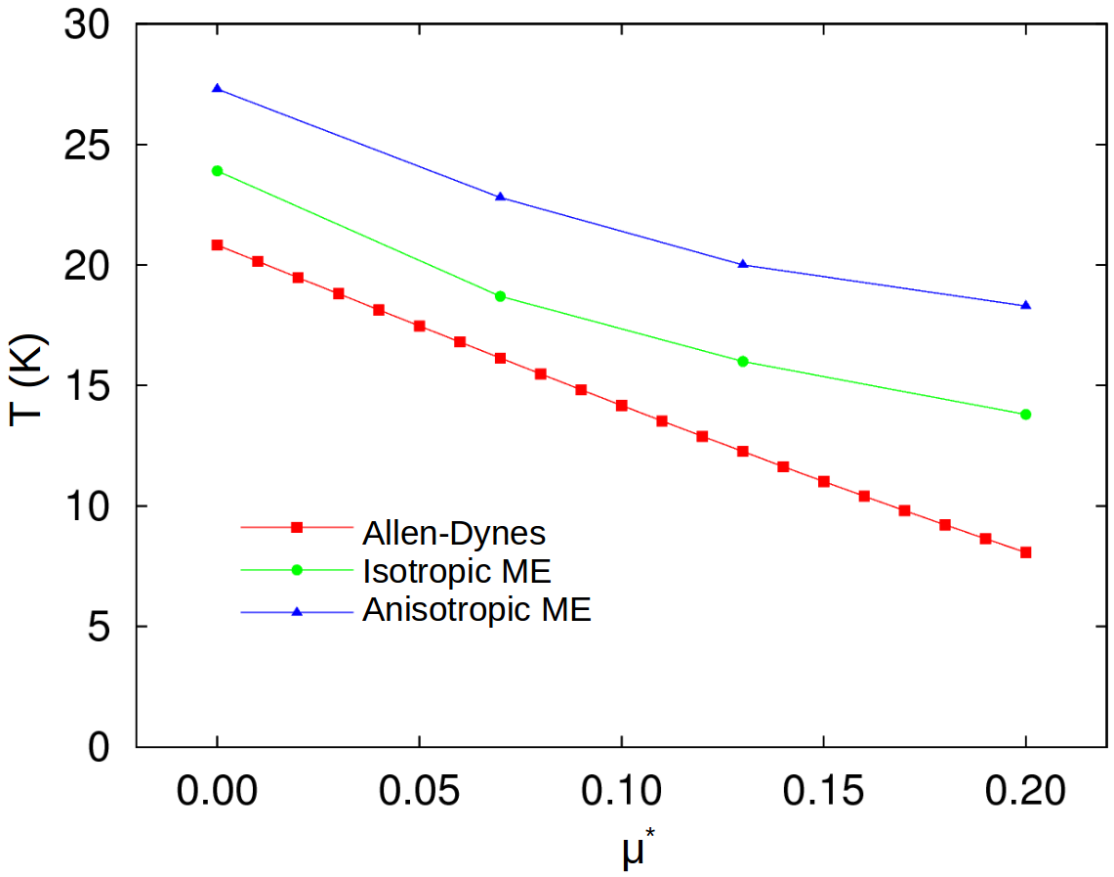


Figure 5.10: The superconducting critical temperature in 0.06 e/u.c. doped 1H-MoS_2 as a function of the Coulomb pseudopotential. The blue triangles are the solutions of the full anisotropic Eliashberg equations, while the green circles are the correspond tot he isotropic approximation and the red squares are the results of the Allen-Dynes equation.

diagram in terms of the doping concentration x. The first region concerns the part of the phase diagram $0 \leq x < 0.06$ where there is no superconductivity. Second is the region $0.06 \leq x \lesssim 0.1$, where the T_c increases in temperature with increasing x. The third region is the start of the decrease in T_c with increasing carrier density, which roughly corresponds to $0.1 \leq x \lesssim 0.13$. The final region is for $x \geq 0.13$ for which there is no available data for gate-doping induced superconductivity although it has been suggested that the decrease in T_c connects smoothly to the alkali metal-doped MoS_2 compounds [44].

Firstly, it should be noted that our calculations can explain the sharp onset of superconductivity at a carrier density of n_{2D}=6×10^{14} cm^{-2}. This carrier concentration corresponds to a doping concentration of 0.06 extra electrons per unit cell. In both our rigid band model and the fixed lattice jellium model a doping concentration of 0.06 e/u.c. is exactly the concentration at which the Fermi surface at Q appears. As discussed in Chapter 4, the presence of a Fermi sheet at Q massively increases the number of possible phonon scattering mechanisms, leading to a larger value for λ. As a result the material becomes superconducting. Our calculation of the λ for the doping concentration of 0.01 e/u.c. yielded a very small value for $\lambda = 0.09$. The T_c can be calculated for this doping level using the Allen-Dynes equation (Eq. 5.1). Even in the best-case scenario of vanishing Coulomb pseudopotential, $\mu^* = 0$, the calculated $T_c = 0.0002$ K. Thus, the onset of superconductivity in monolayer electron-doped MoS_2 can be attributed to the filling of electronic states at Q, rather than just at K.

The second region identified above was studied using the jellium model for both an optimised unit cell and fixed unit cell. It was found that in the case of the optimised cell, the T_c actually decreases between the 0.06 e/u.c. and 0.1 e/u.c. doping levels. Although an explanation for why this is the case can be provided, it is clear that this model is not capturing the physics of the system correctly. On the other hand, the fixed lattice jellium model does find that T_c increases from an onset near 0.06 e/u.c. Furthermore, it has been shown that the electron-phonon coupling and T_c are greatly enhanced when the sizes of the Fermi sheets at K and Q are similar. In the fixed lattice jellium model this occurs very near $x = 0.1$. This may explain why the maximum T_c is found at this carrier density. It is therefore clear that the fixed-cell jellium model is superior for studying the electron-doping dependence of the electron-phonon interaction in monolayer MoS_2.

There are however, discrepancies between the calculated T_c vs doping concentration dependence in the fixed-lattice jellium model and experiment. Firstly, the calculated T_c is larger than the temperature found in experiment. More importantly, at very the very high doping level of 0.17 e/u.c. the T_c increases rather than the expected decrease. This is not however, as big a problem as it might seem. As no experimental data exists for this doping concentration it is possible that the experimental T_c is actually higher at this concentration and connecting the phase diagram to that of bulk alkali metal-doped compounds is not appropriate. Another consideration is that when calculating the phonons at this doping using a small smearing of 10 meV, it was found that there is a dynamical instability at M. This does not occur in the relaxed cell due to the different electronic structure of the lowest energy conduction band. In addition, by using a larger smearing real phonon frequencies were obtained for the 0.17-fix e/u.c. doping level. However, if this effect is physical as opposed to an artifact of the calculation as it assumed, then this may indicate the onset of a charge density wave regime, as it has been suggested in a very recent paper [205].

The question still remains of how an increase in doping can lead to a decrease in the critical temperature, as is found experimentally in the region $0.1 \leq x \lesssim 0.13$. In the relaxed cell jellium model it was shown that T_c can decrease with increasing electron-doping. This occurred between the 0.06 e/u.c. and 0.1 e/u.c. doping levels and was attributed to the fact that at 0.06 e/u.c. the Fermi sheets at K and Q were of very similar size and shape, and this causes stronger nesting leading to greater λ and hence T_c. As the doping increases, the additional electrons all fill states near K, and so the sizes of the Fermi sheets at K and Q are very different. The result is a smaller λ and hence lower T_c. It is proposed that in the fixed-cell jellium model a similar trend would occur just above the 0.1 e/u.c. doping

level. This is because the sizes of the K and Q Fermi surfaces are very similar at 0.1 e/u.c. and extra electron are expected to fill only states near Q. This would in turn cause a difference in the sizes of the Fermi pockets at K and Q leading to a smaller λ and lower T_c. Therefore, a clear direction for further work is to calculate the electron-phonon coupling and superconducting critical transition temperature for a range of doping levels between 0.1 e/u.c and 0.17 e/u.c. As it is also possible that the relaxed unit cell model is correct but finds the peak T_c at lower doping concentrations it is also worth investigating the electron-phonon coupling and superconductivity in this model for doping levels between 0.01 e/u.c. and 0.06 e/u.c.

Chapter 6

The Role of the Fluorine Dopant in the Magnetic Phase Diagram of $LaFeAsO_{1-x}F_x$ Superconductors

6.1 Introduction

The discovery of superconductivity in $LaFeAsO_{1-x}F_x$ with a critical temperature T_c of 26 K generated considerable interest in the iron pnictides [38]. Substitution of La by other rare-earth elements has been found to lead to even higher T_c values, up to 55 K in F-doped SmFeAsO [206]. Other related iron-based compounds are also superconducting when doped, such as $BaFe_2As_2$, LiFeAs, and $FeSe_{1-\delta}$ [207–209].

As discussed in Chapter 1, it is thought that the pairing mechanism in iron-based superconductors is not primarily phonon-mediated [210, 211]. As a result, it is not appropriate to use the Migdal-Eliashberg theory to calculate the critical temperature as in the last chapter.

Instead, the onset of the superconductive state from the magnetic parent com-

pound LaFeAsO can be studied. Despite considerable efforts in the area of first-principles computational modelling of $LaFeAsO_{1-x}F_x$ and other iron-based superconductors, the atomistic mechanism underlying this magnetic to nonmagnetic transition remains an outstanding issue. For instance, while neutron scattering experiments yield a magnetic moment of 0.36 μ_B for the Fe atoms in LaFeAsO at T=8 K, the moment predicted by density-functional theory calculations ranges between 0.8 and 2.6 μ_B [212–215]. The origin of this discrepancy is still under debate [216]. The analysis of the magnetic phase diagram is further complicated by the strong sensitivity of the electronic ground state of LaFeAsO to the fine details of the crystal structure [213]. Most importantly, several attempts at modelling the evolution of the magnetic ground state as a function of F doping in $LaFeAsO_{1-x}F_x$ consistently failed to reproduce the magnetic/nonmagnetic transition observed in experiment [212, 217–219].

This chapter is organised as follows. Firstly, the calculation details are provided, including an explanation of the different models used to simulate the F doping. The magnetic parent compound LaFeAsO is then investigated. The electronic structure and magnetic ground state of this material are determined. Next, the effect of increased fluorine doping on the magnetic moment of the Fe atoms in $LaFeAsO_{1-x}F_x$ is studied.

Experimental studies have shown that this magnetic moment is quenched at the onset of the superconductive state in this material, and thus the role of the F dopants in this phase transition can be investigated. The effect of the F dopants on the structure of $LaFeAsO_{1-x}F_x$ is also examined.

Based on results obtained in this chapter, a minimal model which can describe the physics of the magnetic to nonmagnetic transition is developed. Using this model, the evolution of the electronic structure with increased F doping is studied.

Finally, the lattice dynamics of both the undoped parent compound LaFeAsO and non-magnetic $LaFeAsO_{1-x}F_x$ are compared, in order to determine how the electron-phonon interaction differs in these cases.

6.2 Computational Methods

As in the study of monolayer MoS_2, all DFT calculations were performed using the `Quantum ESPRESSO` software package [176]. The exchange-correlation energy was approximated with the generalised gradient approximation of Ref. [100]. Previous work on these materials showed that the lattice parameters are better described in GGA than LDA [220]. The valence electronic wavefunctions and charge density were described using planewaves basis sets, which were considered converged with kinetic energy cutoffs of 35 Ry and 420 Ry, respectively. In order to describe the core-valence interaction, ultrasoft pseudopotentials were used for La, As, O, and F [105]. In the case of Fe, the projector-augmented wave method was used [106]. This is because it has been shown that the core electrons of Fe are important for distorting the lattice in $LaFeAsO_{1-x}F_x$ [220]. Structural optimisations were carried out until the force on each atom was below 10 meV/Å and the pressure in the unit cell was below 0.5 kbar.

Most structural optimisations were performed using the standard Broyden-Fletcher-Goldfarb-Shanno method [176]. However, occasionally during the relaxation, while the true ground state was magnetic, it was found that the system became trapped in a nonmagnetic local minimum. This effect arises from the connection between the As height and the magnetic moment [217]. This difficulty was circumvented by validating all the calculated structures and magnetic ground states using additional structural optimisations at fixed lattice parameters.

Calculations of the Fe magnetic moment as a function of F doping in $LaFeAsO_{1-x}F_x$ were carried out within a jellium model, a virtual-crystal approximation model, and by explicitly including the F atoms in the computational cell (explicit doping model). In the jellium model, as with modelling of the electron doping in 1H-MoS_2, the negative charge of the doped electrons is compensated by a uniform positive background. In contrast, in the virtual crystal approximation model, ultrasoft pseudopotentials were generated for the virtual atoms $O_{1-x}F_x$ using the ionic charge $Z_{O_{1-x}F_x} = 6 + x$. This method is expected to be an improvement on the jellium model, as the extra electrons introduced by the F dopants are located in the LaO layers, rather than spread uniformally across the unit cell, as in the jellium model.

For the calculations on the parent compound LaFeAsO and for those on the doped compound within the jellium model and virtual crystal approximation model, a $\sqrt{2} \times \sqrt{2}$ supercell in the FeAs plane was adopted. This is the smallest supercell which can support a stripe-antiferromagnetic ground state (see Fig. 6.3). The Brillouin zone of this cell was sampled on a 6×6×5 Monkhorst-Pack grid [103].

6.3 LaFeAsO

LaFeAsO crystallises in the ZrCuSiAs type structure (space group P4/nmm). As shown in Fig. 6.1, LaFeAsO consists of alternating layers of FeAs and LaO, and the tetragonal unit cell is comprised of two formula units. The a and c lattice parameters and the internal coordinates of the La and As atoms along the c axis are sufficient to fully describe the crystal structure.

Before studying the effect of doping in $LaFeAsO_{1-x}F_x$, it is first instructive to investigate the pristine material LaOFeAs. The electronic band structure was

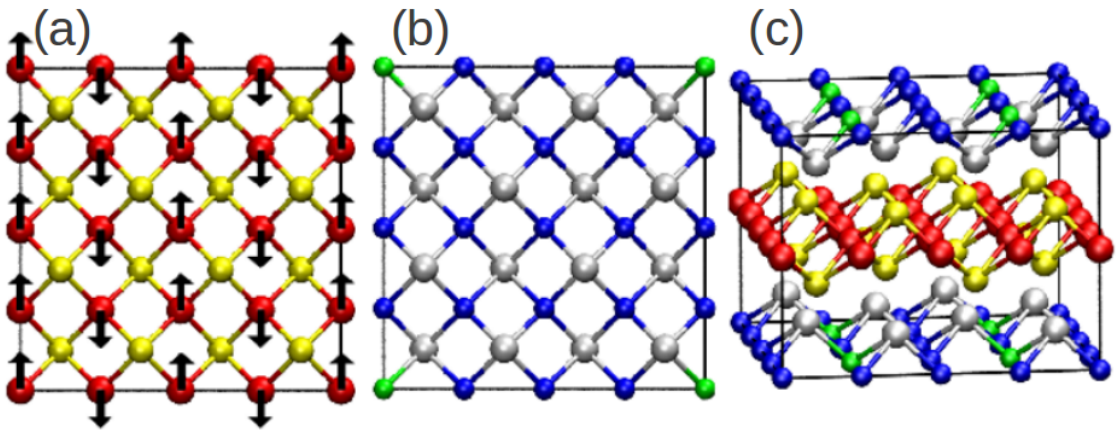


Figure 6.1: Ball-and-stick representation of $LaFeAsO_{1-x}F_x$. (a) Top-view of the Fe-As layer in the $2\sqrt{2}\times2\sqrt{2}$ unit cell, containing 16 FeAs units (Fe and As atoms in red and yellow, respectively. The stripe-antiferromagnetic spin texture of the Fe atoms in pristine LaFeAsO is shown schematically. (b) Top view of the LaO layer (La and O atoms in silver and blue, respectively), with one O atom replaced by F (green). In this model corresponding to x=0.0625 the nearest-neighbour distance between F dopants is 11.3 Å. (c) Lateral view of $LaFeAsO_{1-x}F_x$ with $x = 0.5$ and the F atoms in the most symmetric arrangement. The unit cell contains 64 atoms.

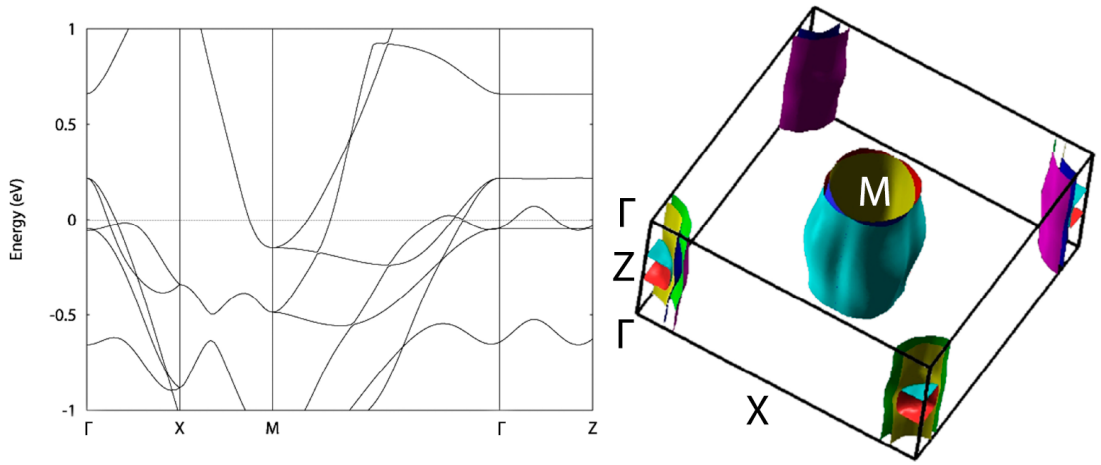


Figure 6.2: Band structure and Fermi surface of non-magnetic pristine LaFeAsO with optimised lattice parameters.

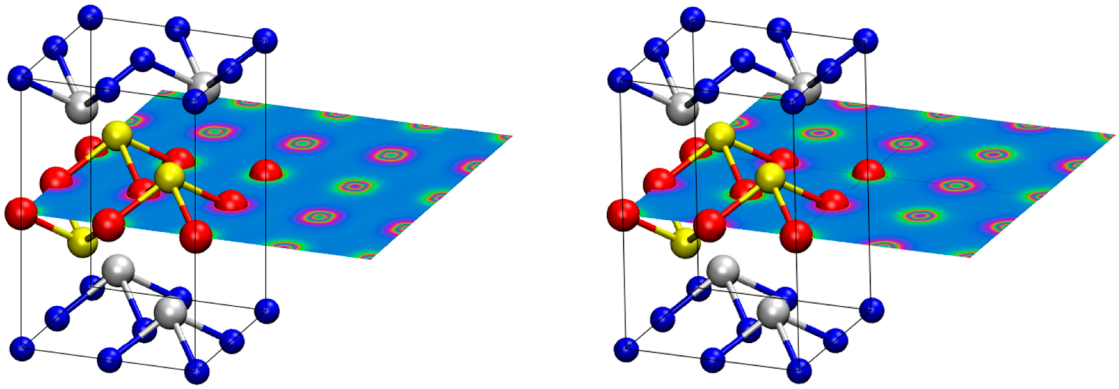


Figure 6.3: The spin-polarised DFT calculations indicate that the magnetic ground state of LaFeAsO is stripe antiferromagnetic (left), as opposed to checkerboard AFM (right), ferromagnetic, or non-magnetic states. The atoms are of the same colour as 6.1 and the isosurface shows the spin-up or spin-down alignment of the Fe atoms.

calculated, and can be seen in Fig. 6.2. It shows that LaFeAsO is a semimetal and the calculated Fermi surface displays five sheets. These can be attributed to Fe $3d$ orbitals, in good agreement with other DFT studies [79, 80]. There are two cylindrical electron sheets centred at the M point and two cylindrical hole sheets centred at the zone centre. The fifth sheet is a hole pocket centred at the Z point, and is more three-dimensional in character due to hybridisation between Fe d and La states [79].

The magnetic ground state of LaFeAsO was investigated previously in Ref. [220]. The results are included here in order to understand the energy separation between the magnetic and nonmagnetic ground states. Within the $\sqrt{2}\times\sqrt{2}$ supercell there are four Fe atoms. This allows for four different possible magnetic states: firstly, the nonmagnetic (NM) state, in which there is no spin polarisation; and secondly, a ferromagnetic (FM) configuration, in which all Fe atoms are spin polarised in the same direction. The final two configurations are both antiferromagnetic, that is, the Fe atoms alternate between spin up and spin down. A stripe antiferromagnetic

	a (Å)	b (Å)	c (Å)	z(As)
Expt.	5.70	5.70	8.74	0.6513
NM	5.64	5.64	8.60	0.6408
FM	-	-	-	-
AFM(c)	5.68	5.68	8.72	0.6514
AFM(s)	5.67	5.73	8.72	0.6514

Table 6.1: A comparison of the lattice parameters as calculated in Ref. [220] for various magnetic configurations. Also included are the experimental values from Ref [212]. Adapted from [220].

[AFM(s)] and checkerboard antiferromagnetic [AFM(c)] ordering were considered. These can be seen in Fig. 6.3. The optimised lattice parameters and energetics for each magnetic ordering were calculated and are summarised in Tables 6.1 and 6.2, respectively. Here a stabilisation energy, E_{stab}, has been defined as:

$$E_{\text{stab}} = -[E_{\text{tot(mag)}} - E_{\text{tot(non-mag)}}], \tag{6.1}$$

where $E_{\text{tot(mag)}}$ is the total energy of the magnetic case, i.e. FM, AFM(c) or AFM(s); and $E_{\text{tot(non-mag)}}$ is the total energy of the non-magnetic case.

It can be seen in Table. 6.2 that, in good agreement with other DFT studies, the stripe antiferromagnetic ordering is the most energetically stable [213, 214]. It is also within this ordering that the optimised lattice parameters are closest to those found experimentally, as shown in Table. 6.1. It was discovered that ferromagnetic ordering was energetically unfavourable, and all relaxation calculations which started in a ferromagnetic configuration converging to a nonmagnetic solution.

The magnetic ordering along the c-axis was also considered. The 2D planes of Fe atoms can be stacked along the c-axis in either a ferromagnetic or antiferro-

	Total energy per Fe atom (eV)	Stabilisation energy (meV)	Stabilisation energy from [222] (meV)
NM	-5660.055	0	0
FM	-	-	-
AFM(c)	-5660.15	97	86
AFM(s)	-5660.245	192	190

Table 6.2: The stability of the various magnetic ordering as calculated in GGA. Results agree well with values obtained from the literature. Adapted from [220].

magnetic fashion. Due to the periodic boundary conditions used, the ferromagnetic alignment along the c-axis has already been considered in the $\sqrt{2}\times\sqrt{2}$ supercell calculations. In order to investigate the antiferromagnetic stacking, a supercell with dimensions $\sqrt{2}\times\sqrt{2}\times 2$ was used. Using this larger cell it was found that the stripe antiferromagnetic ordering in the plane of the FeAs layers, with antiferromagnetic stacking along the c-axis, is the most energetically stable magnetic ordering. Muon spin relaxation experiments have confirmed that this is indeed the observed magnetic ordering in LaFeAsO [221]. However, while the in-plane stripe antiferromagnetic ordering is over 100 meV more stable than the checkerboard antiferromagnetic configuration, antiferromagnetic ordering along the c-axis is less than 0.1 meV more stable than ferromagnetic ordering along the c-axis. This is a very small stabilisation energy, and to be correctly modelled it requires a cell twice as large, thereby drastically increasing the computation time. Therefore it is a sensible approximation to ignore this magnetic ordering and describe LaFeAsO using only the $\sqrt{2}\times\sqrt{2}$ supercell with in plane stripe antiferromagnetic magnetic ordering. Using this magnetic configuration a calculated magnetic moment of 2.13 μ_B per Fe atom was obtained. This is within the range of previous first-principles calculations [213–215].

6.4 $LaFeAsO_{1-x}F_x$

The magnetic phase diagram of $LaFeAsO_{1-x}F_x$ was investigated by calculating the magnetic moment of the Fe atoms as a function of F doping in three different models. From Fig. 6.4, it is clear that calculations within the jellium model or the virtual crystal approximation model fail to reproduce the measured magnetic/nonmagnetic phase transition with increasing F doping. Even when considering a heavily doped compound such as $LaFeAsO_{0.5}F_{0.5}$, both the jellium model and the virtual crystal approximation model yield a stripe-antiferromagnetic ground state, as in LaFeAsO. Figure 6.4 also shows that, within the jellium model and the virtual crystal approximation model, the magnetic moment does not decrease as a function of the F content x, contrary to experimental observations [219].

It is worth noting that in two previous studies a magnetic phase transition was reported within a jellium model and within constrained DFT based on the virtual crystal approximation, respectively [223, 224]. However, Ref. [223] relies on a localised DZP basis set, which is known to incorrectly describe the energetics of magnetic Fe [225]. Furthermore, unconstrained virtual crystal approximation calculations performed by some of the authors of Ref. [224] are in line with our results and demonstrate the failure of the virtual crystal approximation in $LaFeAsO_{1-x}F_x$ [218].

Due to the failure of the jellium and virtual crystal approximation models, a new model was proposed, where the F atoms were explicitly included, which will be referred to as the "explicit doping model". It was hoped that this model could capture the mechanism underlying the phase transition observed in experiments. In order to include F atoms in these calculations, a larger supercell was considered, corresponding to a $2\sqrt{2} \times 2\sqrt{2}$ unit cell (Fig. 6.1). This supercell contained 16

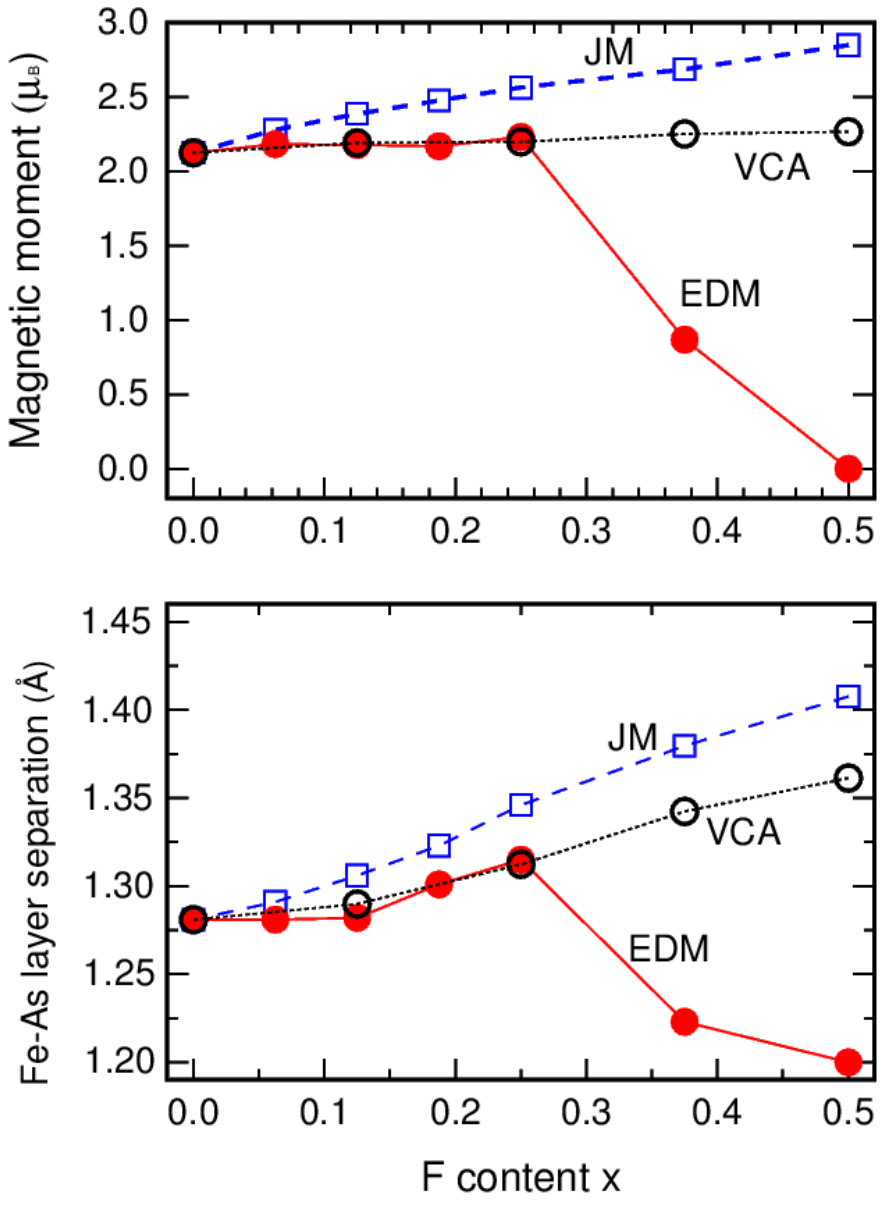


Figure 6.4: (a) Calculated magnetic moment per Fe atom in $LaFeAsO_{1-x}F_x$ as a function of F content x. The red disks correspond to the explicit doping model, the open blue squares correspond to the jellium model, and the black circles are for the virtual crystal approximation model. The lines are guides to the eye. A magnetic/nonmagnetic phase transition is obtained only within the explicit doping model. (b) Variation of the As height in $LaFeAsO_{1-x}F_x$ as a function of F content x. The red disks, blue squares, and black circles refer to the explicit doping model, jellium model, and virtual crystal approximation model calculations, respectively, and the lines are guides to the eye. The calculations using the jellium and virtual-crystal approximation models yield incorrect structural trends. The explicit doping model calculations reveal a compression of the Fe-As layer upon doping.

LaFeAsO formula units, allowing the investigation of the effect of F corresponding to doping levels, x, in multiples of 1/16=0.0625. For consistency with the previous jellium model and virtual crystal approximation model calculations, the Brillouin zone of the large supercell was sampled on a 3×3×5 Monkhorst-Pack grid. For a given doping level $x = n/16$ (n integer), n O atoms were replaced substitutionally by an equal number of F atoms. It was found that, even after taking into account the symmetry of the system, the number of possible inequivalent structures grows very rapidly with n. For example, there are 1, 5, and 16 inequivalent structures when replacing 1, 2, or 3 O atoms in the supercell by F, respectively.

Since the energy separation between magnetic and nonmagnetic ground states is of only 12 meV/atom, all the calculations required *full* atomic and lattice optimisations, and were computationally extremely intensive. As it proved impractical to analyse every possible dopant configuration, an alternative strategy was adopted: for each doping level, a small subset of configurations was sampled. This always included the least and the most symmetric F patterns. Systematics within this small subset of configurations were then sought in order to formulate a hypothesis on the effect of the F dopants. This hypothesis was then tested by performing separate calculations which did not depend on the precise location of the F atoms. A total of 14 F configurations were considered. While this set of configurations is not statistically significant, it represents a useful starting point for identifying trends.

Figure 6.4 shows that, within the explicit doping model, the inclusion of the F dopant produces a phase transition with an onset at x∼0.25. At x=0.5, the ground state of the system is nonmagnetic. It can also be observed that the $LaFeAsO_{1-x}F_x$ crystal structure is essentially unchanged up to x=0.25. Above this dopant concentration, the c-axis shortens and the average As height is *reduced*

from 1.31 Å (x=0) to 1.20 Å (x=0.5).

6.5 Fe-As Layer Separation

In the non-magnetic phase, the F dopants induce a uniform contraction of the Fe and As planes. The compression of the c-axis is consistent with powder X-ray diffraction data, although the calculated contraction (0.33 Å) is more pronounced that in the experiment (0.04 Å) [226]. This is consistent with the overestimation of the magnetic moment of pristine LaFeAsO.

A previous theoretical study, where the F dopants are explicitly included, reports a non-magnetic configuration at x=0.125, in apparent contradiction with the present results [227]. However, in Ref. [227] the calculations are spin-unpolarised, hence they correspond to a local energy minimum, while here the magnetic ground state is addressed (which is spin-polarised at x=0.125, Fig. 6.4).

In order to identify the atomistic mechanism underlying the phase transition shown in Fig. 6.4, the correlation between magnetic moment and structural parameters was investigated. The only quantities which show a clear correlation are the As height (Fig. 6.5) and the c-axis length. A similar effect has been observed in neutron diffraction experiments on the related ferropnictide compound $CeFeAs_{1-x}P_xO$ [228]. The correlation here determined between Fe magnetic moment and pnictogen height is in line with previous DFT calculations on LaFeAsO [217].

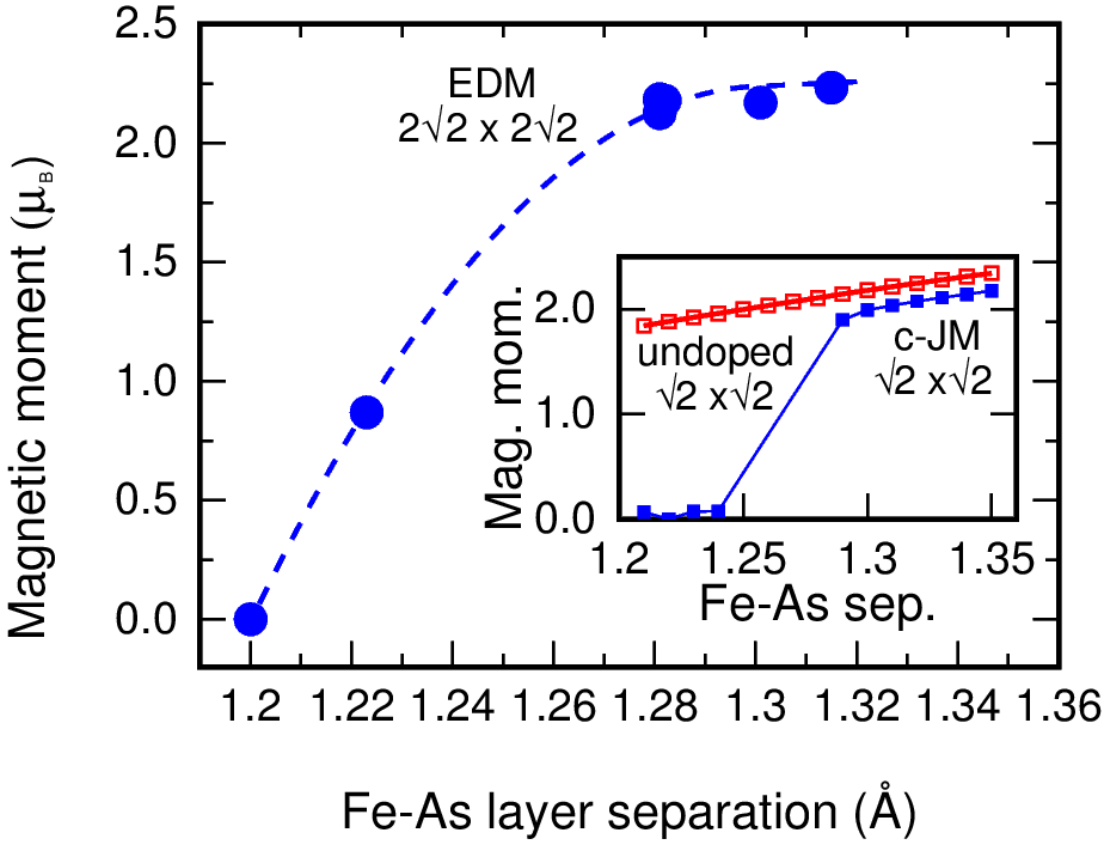


Figure 6.5: Calculated magnetic moment per Fe atom in $LaFeAsO_{1-x}F_x$ vs. average Fe-As layer separation in the optimised ground-state geometry (blue disks), as obtained within the explicit doping model. The dashed line is a guide to the eye. Inset: Calculated magnetic moment per Fe atom vs. Fe-As layer separation for the two cases of undoped LaFeAsO (open red squares) and of LaFeAsO with additional 0.5 electrons per Fe atoms (compressed jellium model of $LaFeAsO_0.5F_0.5$, blue filled squares). The lines are guides to the eye. The calculations in the main panel and in the inset correspond to the $2\sqrt{2}\times 2\sqrt{2}$ and the $\sqrt{2}\times\sqrt{2}$ unit cells, respectively.

6.6 Minimal Model

Calculations using the explicit doping model are computationally intensive, due to the large supercell required. It is therefore desirable to develop the simplest possible model of $LaFeAsO_{1-x}F_x$ which is capable of reproducing the magnetic/nonmagnetic phase transition as obtained within the explicit doping model in Fig. 6.4, but without incorporating the F atoms explicitly. Since the correlation in Fig. 6.5 suggests that the compression of the Fe-As layer is essential to the phase transition, undoped LaFeAsO was used as a starting point. Several modified structures, with the same lattice parameters as pristine LaFeAsO, but with the Fe-As layer separation in the range of 1.20-1.35 Å as in the explicit doping model calculations of Fig. 6.5, were considered. For each As height, two limiting cases were considered: (i) the total number of electrons as in pristine LaFeAsO, and (ii) the electron number the same as in $LaFeAsO_{0.5}F_{0.5}$. The blue filled squares in the inset of Fig. 6.5 show that, when adding electrons to the compressed Fe-As layer within the jellium model, the magnetic moment is quenched at a critical As height of 1.22 Å, in close agreement with our explicit doping model calculations in Fig. 6.5. On the contrary, the magnetic ground state of the modified LaFeAsO structure without the extra electrons is stripe antiferromagnetic for all the As heights considered. This can be seen by the open red squares in the inset of Fig. 6.5. These findings demonstrate that both the compression of the Fe-As layer and the presence of extra electrons crucially contribute to the suppression of the magnetic order. Since this result does not depend on the precise location of the F atoms in the supercell, this model provides an *a posteriori* justification for our explicit doping model approach. It is therefore clear that the simplest model of the magnetic phase transition in F-doped LaFeAsO must include *both* the compression of the Fe-As layer and the presence

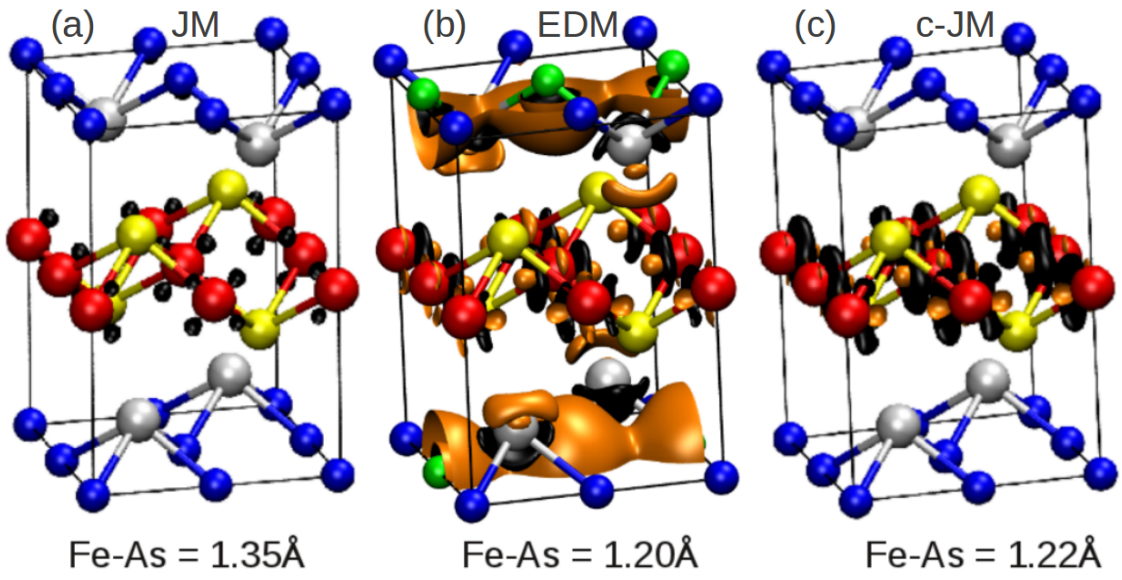


Figure 6.6: Charge density isosurfaces of doped electronic charge in $LaFeAsO_{1-x}F_x$ at x=0.5. Excess (defect) electronic charge is represented in black (orange). The colour code for the ball-and-stick representations is the same as in Fig. 6.1. (a) Jellium model with the structure of pristine LaFeAsO (Fe-As layer separation: 1.35 Å). The doped electrons incorrectly fill Fe-d_{yz} states only. (b) Explicit doping model. In this case the optimised Fe-As layer separation is 1.20 Å. The doped electrons fill the Fe d_{xy} and d_{yz} states, and vacate the $d_{x^2-y^2}$ states. Additional charge rearrangement takes place in the F-doped LaO layer. (c) Simplified jellium model where the Fe-As layer is compressed as in the explicit doping model (separation: 1.22 Å), and extra electrons are added. The charge rearrangement in this case is very similar to the more sophisticated explicit doping model calculation in (b).

of the F electrons within a jellium model. Such a model can be referred to as a "compressed jellium model".

The simple compressed jellium model allows for analysis of the underlying mechanism of the doping-induced phase transition in LaFeAsO, without the additional complication of the randomness introduced by dopants. Figure 6.6 shows the spatial distribution of the doped charge for the limiting case of $x = 0.5$ in three of the models considered here: the explicit doping model, the jellium model, and the compressed jellium model. In both the explicit doping and compressed jellium models, the doped charge exhibits substantial weight on the Fe d_{xy} and d_{yz} orbitals,

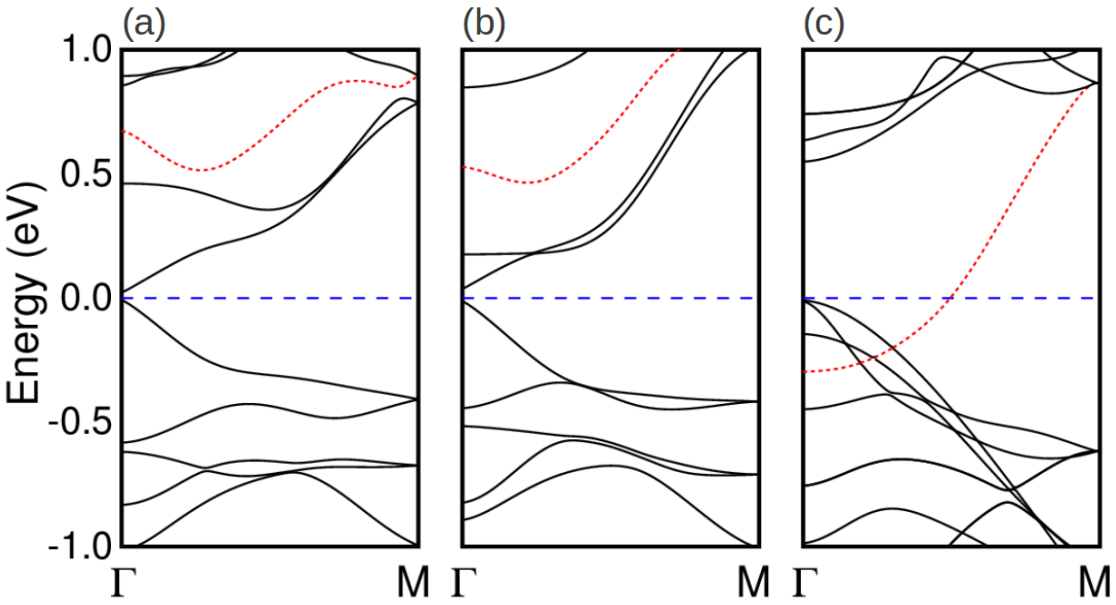


Figure 6.7: Band structures of $LaFeAsO_{1-x}F_x$ within the $\sqrt{2}\times\sqrt{2}$ unit cell. The Fermi level is indicated by the blue dashed line. The unoccupied band of predominant Fe d_{yz} character is highlighted in red (dotted line). (a) Pristine LaFeAsO. (b) Undoped LaFeAsO with compressed Fe-As layer. (c) Compressed jellium model of $LaFeAsO_{1-x}F_x$ at $x = 0.5$. The band dispersing upwards from Γ near the Fermi level in (a) and (b) has also d_{yz} character and merges into the red dotted curve in (c) upon suppression of the magnetic order. This is the only band which is filled upon doping in the standard jellium model, as shown in Fig. 6.6(a).

while the $d_{x^2-y^2}$ orbitals are depleted (the x axis is aligned with the in-plane Fe-Fe direction). On the other hand, in the standard jellium model the extra electrons only occupy the Fe d_{yz} states. These observations suggest that the band structures of the explicit doping and compressed jellium models are in close agreement, while the normal jellium model leads to an incorrect band filling. Similar calculations within the virtual-crystal approximation indicate that the virtual crystal approximation also leads to an incorrect band filling, in the same way as the standard jellium model.

6.7 Electronic Structure

Fig. 6.7 shows the evolution of the band structure from pristine LaFeAsO to LaFeAsO with a compressed FeAs layer, and then to doped LaFeAsO within the compressed jellium model. Upon compression [Fig. 6.7(a) to Fig. 6.7(b)], an unoccupied band of predominant Fe d_{yz} character shifts towards the Fermi level at Γ. When the dopant electrons are added [Fig. 6.7(b) to Fig. 6.7(c)], this band crosses the Fermi level. Since, from $x = 0$ to $x = 0.5$ the d_{yz} band near Γ shifts symmetrically across the Fermi level (Fig. 6.7), the magnetic phase transition that was identified at $x{\sim}0.25$ in the explicit doping model must be closely related to a Fermi level crossing. It is possible that such a Fermi level crossing stabilises the nonmagnetic phase by providing an additional screening channel to the second-nearest neighbour Fe-Fe super-exchange interaction [214]. In the compressed jellium model for $x = 0.5$, it was found that bands with d_{xy} and $d_{x^2-y^2}$ character have moved below and above the Fermi level, respectively. This is fully consistent with the charge redistribution observed in Fig. 6.6(b),(c).

Due to the overestimation of the Fe magnetic moment in pristine LaFeAsO within DFT, the mechanism proposed here only explains qualitatively the magnetic phase transition in this compound. Indeed, the phase transition identified here takes place for a F content which is about an order of magnitude larger than in experiment (calculated onset at $x = 0.25$ vs. $x = 0.04$ in Ref. [219]). This is consistent with the overestimation of the magnetic moment in LaFeAsO by approximately the same amount, and is in line with recent constrained-DFT calculations [224]. In order to reconcile calculations and experiment on pristine LaFeAsO, mechanisms based on spin fluctuations have been proposed in Refs. [216], [229], and [230]. These proposals involve a suppression of the long-range magnetic order

due to the increase of spin fluctuations with doping. It is expected that, by combining our model with such proposals, a quantitative agreement with experiments can finally be achieved.

The mechanism proposed here may also explain the suppression of magnetic order in LaFeAsO upon application of pressure [231]. In LaFeAsO under pressure the c-axis shortens and the As height is reduced, similarly to the F-doped compound considered here [232]. This similarity suggests a common origin for the suppression of magnetism upon F-doping or upon application of pressure, respectively.

6.8 Phonon Density of States

The present findings carry implications for the study of electron-phonon interactions in superconducting $LaFeAsO_{1-x}F_x$. In fact, according to these results, the calculation of the electron-phonon coupling strength should be carried out within a jellium model with the compressed Fe-As layer, not within the structure of pristine LaFeAsO in the non-magnetic LDA structure [45, 227].

In order to investigate this further, the phonon density of states (PDOS), within both the pristine LaFeAsO structure and the compressed jellium model for a doping level of $x = 0.5$, was calculated. The results are shown in Fig. 6.8, and the pristine case agrees well with earlier DFT studies [45, 79].

Fig 6.9 shows the phonon density of states obtained for both pristine and $x = 0.1$ doped $LaFeAsO_{1-x}F_x$ via inelastic neutron scattering methods [233]. It can be seen in Fig. 6.9 that, at room temperature, the pristine and doped phonon density of states are very similar. The position of the peaks in the low energy part of the experimental and calculated PDOS are in good agreement. The intensities of the peaks are not comparable as the calculated peaks have not been weighted by the

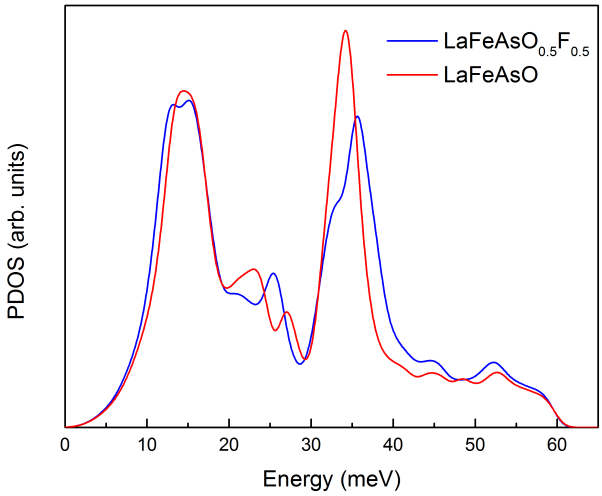


Figure 6.8: The calculated phonon density of states. The red line is for pristine LaFeAsO and the blue line is for $LaFeAsO_{0.5}F_{0.5}$ as modelled in the compressed jellium model. Both phonon density of states have been convolved with a Gaussian in order to enable the comparison to the experimental spectra.

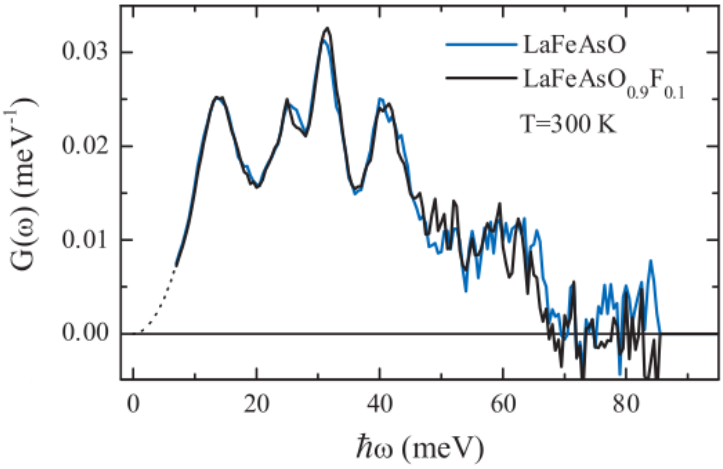


Figure 6.9: The phonon density of states as obtained from inelastic neutron scattering at room temperature for both LaFeAsO (blue line) and $LaFeAsO_{0.9}Fe_{0.1}$ (black line). Adapted from [233].

ratio of the neutron scattering cross section divided by the mass of each atom.

The peaks in the calculated PDOS are also very similar between the pristine and doped compressed jellium model. There are however, a few key differences. While, the peak around 15 meV softens slightly upon doping, the peak near 35 meV stiffens. This is in contrast to calculations of the PDOS of $LaFeAsO_{0.5}F_{0.5}$ using the standard jellium model without compression of the Fe-As layer separation, where the phonon modes around 35 meV soften by almost 5 meV with respect to the pristine case. This large softening can be explained by the unphysically large Fe-As layer separation in this model.

It is known that the phonon modes around 15 meV contribute most to the electron-phonon coupling [45]. As a result, the softening of these modes in the compressed jellium model will likely increase the total electron-phonon coupling compared to the pristine case. The stiffening of the modes around 34 meV will likely result in a larger $\omega_{\log}$ in the doped case. The combined effect of these changes in the lattice dynamics will result in a larger T_c than in the pristine structure used for all previous calculations of the electron-phonon interaction in this material. However, these changes in the phonon frequencies are very small and any such change in T_c is likely to be minute. This further adds to the widely-held view that these iron-based materials are not conventional phonon-mediated superconductors.

6.9 Conclusions

In conclusion, the crucial role of the F atoms in driving the antiferromagnetic to nonmagnetic transition in LaFeAsO has been established. In particular, it has been shown that, in order to reproduce the magnetic/nonmagnetic phase transition in $LaFeAsO_{1-x}F_x$ observed in experiments, neither the standard jellium model, nor

the virtual crystal approximation method of modelling the dopant, is sufficient, and it is crucial to explicitly include F atoms in the calculations. In fact, the F dopants not only introduce extra electrons, but also induce structural distortions which act to reduce the As height and modify the band structure of pristine LaFeAsO, leading to a Fermi-level crossing and a suppression of the magnetic order.

A simple jellium model for $LaFeAsO_{1-x}F_x$ has also been developed. This will enable more advanced calculations, based, for instance on DMFT or *GW* techniques, using small unit cells and yet capturing the essential physics of the doping [234, 235].

Incidentally, these results have highlighted the importance of carrying out very careful global optimisations involving all the lattice degrees of freedom in order to identify the correct magnetic ground state in $LaFeAsO_{1-x}F_x$.

Chapter 7

Conclusion

7.1 Summary

In this thesis, first-principles techniques have been applied to the study of novel superconducting materials. In the case of the conventional superconductor, monolayer MoS_2, the electron-phonon interaction, which leads to the formation of Cooper pairs at low temperatures, has been extensively studied. The electron-phonon interaction is particularly important in monolayer MoS_2 due to its potential for applications in nanoelectronics. The iron-based superconductor $LaFeAsO_{1-x}F_x$ was also studied. By calculating the magnetic moment of the iron atoms as a function of doping, the origin of the magnetic/nonmagnetic transition was investigated.

Background information about superconductivity and the materials considered in this thesis was provided in Chapter 1. The following two chapters outlined the theory of the first-principles methods which were used in this thesis. In particular, Chapter 2 described how density functional theory and density functional perturbation theory can be used to calculate the electronic structure and lattice dynamics of any material. Methods to calculate properties related to the electron-

phonon coupling were explained in Chapter 3, with a focus on how the T_c of a phonon-mediated superconductor can be calculated using the Migdal-Eliashberg theory.

In Chapter 4, first-principles techniques were used to study the electronic structure of both single-layer and bulk MoS_2. Due to the weak nature of the interlayer bonding, it was found that the band structures of these materials were very similar. However, there exists crucial differences at the top of the valence band and bottom of the conduction band. This results in the bulk material having an indirect band gap whereas the monolayer has a direct band gap, which is important for potential optoelectronic applications. The character of the states at the bottom of the conduction band was studied. It was found that the conduction band minimum at K is comprised mainly of Mo d_{z^2} states while a second minimum at slightly higher energy halfway between Γ and K (the Q point) consists of Mo $d_{x^2-y^2}$ and d_{xy} orbitals. The phonon dispersions of both bulk and single-layer MoS_2 were calculated and found to be in good agreement with both experiment and previous DFT calculations.

The main focus of this chapter was to establish the effect of electron doping on the electron-phonon coupling in 1H-MoS_2. In a simple rigid band model, it was found that as additional electrons fill the conduction band, a Fermi surface is formed at K. There are two main scattering mechanisms which contribute to the e-ph coupling in this case: the dominant intrasheet scattering by phonons with $\mathbf{q} \approx 0$, and a smaller contribution between Fermi sheets at the Brillouin zone edge, K, by phonons with $\mathbf{q} \approx K$. As even more electrons are added to the unit cell, the second minimum at Q becomes occupied. This opens up new scattering channels. The most important of these involves the scattering of electrons between the two conduction band valleys by LA phonons with $\mathbf{q} \approx M$. This leads to a strongly

enhanced electron-phonon coupling. A further increase in the doping level results in a larger density of states at the Fermi level, which enhances λ further. Thus, in a rigid band model, increased doping leads to a stronger electron-phonon coupling. It is, however, known that thin flakes of MoS_2 cause a superconducting dome in the carrier concentration versus T_c plot [44]. Therefore, the expected trend for λ is an increase up to a maximum at some doping level, with higher dopings resulting in a smaller value for λ. One possibility for this discrepancy is the that the model used here fails to correctly capture the physics of the situation. The effect of the extra electrons on the electronic structure and lattice dynamics is not taken into account in a rigid band model. In order to capture these effects, a jellium model was used.

The effect of electron doping on the electron-phonon coupling in monolayer MoS_2 was investigated using a jellium model for doping levels with both fixed lattice constants corresponding to the pristine lattice, and optimised geometry. It was found that this choice of lattice parameter had a dramatic effect on the critical lowest energy conduction band. In the case where the lattice was fixed to that of the pristine case, increased doping resulted in the valley at Q lowering in energy compared to the valley at K. With the addition of sufficient extra electrons, it was found that the conduction band minimum switched from K to Q. For the jellium models with a relaxed lattice parameter, increased electron doping had precisely the opposite effect on the valley structure of the lowest conduction band. As extra electrons were added to the unit cell, the Q valley became higher in energy than the K valley by a greater amount. It was found that, for all doping levels considered in the jellium model, the Fermi surface was composed of electron pockets at both K and Q.

As in the rigid band case, the most dominant scattering mechanism was between

two sheets via longitudinal acoustic phonons with wavevectors equal to M. A Kohn anomaly leads to softening in the phonon dispersions of doped monolayer MoS_2 at key modes at the M point. Softening of the E' and A_1' phonon modes near the zone centre was also observed in the calculated phonon dispersion at all doping levels due to intrasheet scattering. It was discovered that, in general, high doping levels lead to a greater electron-phonon coupling constant. The largest values of λ were obtained when the Fermi sheets at K and Q were of similar size. This induced a substantial phonon softening of both the LA and TA modes at K and a lesser softening at Q, in addition to the softening observed for all doping levels at M. Importantly, it was found that it is possible for the λ to decrease with increasing electron doping. This was found in the relaxed cell jellium model, and was thought to be due to weaker nesting as the Fermi surfaces at K and Q altered in size and shape. It is expected that a similar effect may occur in the fixed lattice model but for a different doping concentration.

The effect of electron doping in 1H-MoS_2 on T_c was investigated in Chapter 5. For all three doping levels considered within both the fixed cell and relaxed cell jellium models, the T_c was calculated using the Allen-Dynes formula, the isotropic Eliashberg gap equations, and the anisotropic Eliashberg gap equations. It was found that for calculations via either the Allen-Dynes equation or isotropic Eliashberg theory, a larger λ led to a higher T_c. However, by solving the fully anisotropic Eliashberg gap equations, it was discovered that T_c was greatly enhanced for doping levels with highly anisotropic gaps at the Fermi surface near Q. This meant that some doping levels had a higher calculated T_c than others, even when they displayed a smaller total electron-phonon coupling. Increased anisotropy of the superconducting gap at K did not cause a higher T_c, suggesting that the gap at Q is more important for determining the critical temperature in this material.

The onset of superconductivity at a doping level of ~ 0.06 e/u.c. in experiment was explained. This is the carrier concentration at which the second minimum in the lowest energy conduction band at Q becomes filled. The resulting increase in the number of possible scattering channels causes a much greater electron-phonon coupling, resulting in superconductivity. Although the dome-shaped dependence of the T_c with increasing electron doping was not found in these calculations, a region where the T_c decreased with increasing electron doping was found. It is possible that by calculating the T_c for more doping levels in this range a dome-shaped region may be found.

Due to the small value of μ^* considered, the calculated critical temperatures are more than twice as large as those found experimentally. By studying the T_c as a function of the Coulomb pseudopotential, it was found that for larger values of μ^*, the calculated T_c can be reduced significantly. As electron doping increases the dielectric screening in a material, it would be best to use a doping dependent value for μ^* which is larger for higher doping levels. This may also help explain the dome-shaped superconductive region, as the T_c will decrease for large values of μ^*.

In Chapter 7, the magnetic phase transition which occurs in $LaFeAsO_{1-x}F_x$ upon sufficient F doping was investigated. In experiment, it has been shown that the onset of the superconductive state is accompanied by a suppression in magnetic order. However, calculations using simple doping models cannot reproduce this phase change. Therefore, a model whereby the F atoms are explicitly included in the calculation was developed. There were two main effects of the F dopants. Firstly, the F atoms induced structural distortions which acted to reduce the As height and lowered an unoccupied band of predominant Fe d_{yz} character around the zone centre towards the Fermi level. Secondly, the extra electrons introduced

by F populated this band and further lowered its energy, leading to Fermi-level crossing and a suppression of the magnetic order.

A minimal model was then developed in order to capture these effects in a less computationally intensive manner. This allowed for the calculation of the phonon density of states. It was found that the minimal model was able to accurately reproduce the effects of doping on the PDOS; however, unlike in monolayer MoS_2, the doping didn't have a large effect on the phonon frequencies. It is therefore very likely that the electron-phonon interaction in the doped structure is not large enough to explain the large T_c found in $LaFeAsO_{1-x}F_x$. This is not unexpected, as it is generally agreed that $LaFeAsO_{1-x}F_x$ is not a phonon-mediated superconductor.

7.2 Future Work

In this thesis, it has been demonstrated that the electron-phonon coupling in single-layer MoS_2 is extremely sensitive to the energetics of the lowest energy conduction band. There is particular sensitivity to the energies of the minima at K and Q, which determine the Fermi surface in electron doped 1H-MoS_2. The shape and size of this Fermi surface have profound implications on both transport properties and superconductivity in this material. It is therefore of great importance to obtain the best possible description of this conduction band. To this end, it would be of great interest to use more sophisticated techniques, such as the GW method, in order to calculate the electronic eigenvalues used as inputs for the electron-phonon interaction.

In order to further clarify the dome-shaped region in the T_c versus electron-doping phase diagram, additional doping levels, particularly in the region of $0.1 -$

0.13 should also be investigated. Such calculations could be combined with the *GW* approach for calculating accurate electronic eigenvalues.

Alternatively, rather than focusing on the superconductivity in monolayer MoS_2, the transport properties could be studied. Building on the calculations of the electron-phonon interaction in this thesis, the Boltzmann transport equation could be used to calculate the electrical conductivity [118].

In relation to the study of iron-based superconductors, the compressed jellium model developed in the study of $LaFeAsO_{1-x}F_x$ could be used as a starting point for future first-principles calculations of the superconductive state. By solving the anisotropic Eliashberg gap equations for this model rather than the pristine structure, the contribution to T_c from the electron-phonon coupling could be determined.

Bibliography

[1] H. K. Onnes. Koninklijke Nederlandse Akademie van Wetenschappen Proceedings Series B Physical Sciences **11**, 168 (1908).

[2] H. K. Onnes. Koninklijke Nederlandse Akademie van Wetenschappen Proceedings Series B Physical Sciences **13**, 1910 (1911).

[3] A. Mourachkine. Room-Temperature Superconductivity. Cambridge International Science Publishing (2004).

[4] M. Tinkham. Introduction to Superconductivity. Courier Dover Publications (2012).

[5] J. S. Schilling. Physica C: Superconductivity **460**, 182 (2007).

[6] J. Bardeen, L. N. Cooper, and J. R. Schrieffer. Physical Review **106**, 162 (1957).

[7] L. N. Cooper. Physical Review **104**, 1189 (1956).

[8] H. Fröhlich. Physical Review **79**, 845 (1950).

[9] Z. Fisk and H.-R. Ott. Superconductivity in New Materials. Elsevier (2010).

[10] J. Gavaler. Applied Physics Letters **23**, 480 (1973).

[11] M. Sigrist and K. Ueda. Reviews of Modern Physics **63**, 239 (1991).

[12] T. Geballe, B. Matthias, J. Remeika, A. Clogston, V. Compton, J. Maita, and H. Williams. Physics **2**, 293 (1966).

[13] W. McMillan. Physical Review **167**, 331 (1968).

[14] F. Steglich, J. Aarts, C. Bredl, W. Lieke, D. Meschede, W. Franz, and H. Schäfer. Physical Review Letters **43**, 1892 (1979).

[15] G. Stewart. Reviews of Modern Physics **56**, 755 (1984).

[16] P. W. Anderson and P. Morel. Physical Review **123**, 1911 (1961).

[17] A. J. Leggett. Reviews of Modern Physics **47**, 331 (1975).

[18] R. Balian and N. Werthamer. Physical Review **131**, 1553 (1963).

[19] I. Foulkes and B. Gyorffy. Physical Review B **15**, 1395 (1977).

[20] P. Anderson. Physical Review B **30**, 4000 (1984).

[21] V. Radhakrishnan. Physics Letters **16**, 247 (1965).

[22] N. Berk and J. Schrieffer. Physical Review Letters **17**, 433 (1966).

[23] V. Ginzburg. Physics Letters **13**, 101 (1964).

[24] W. Little. Physical Review **134**, A1416 (1964).

[25] J. G. Bednorz and K. A. Müller. Zeitschrift für Physik B Condensed Matter **64**, 189 (1986).

[26] M.-K. Wu, J. R. Ashburn, C. Torng, P. H. Hor, R. L. Meng, L. Gao, Z. J. Huang, Y. Wang, and C. Chu. Physical Review Letters **58**, 908 (1987).

[27] A. Schilling, M. Cantoni, J. Guo, and H. Ott. Nature **363**, 56 (1993).

[28] L. Gao, Y. Xue, F. Chen, Q. Xiong, R. Meng, D. Ramirez, C. Chu, J. Eggert, and H. Mao. Physical Review B **50**, 4260 (1994).

[29] H. Krakauer, W. E. Pickett, and R. E. Cohen. Journal of Superconductivity **1**, 111 (1988).

[30] H. Krakauer and W. E. Pickett. Physical Review Letters **60**, 1665 (1988).

[31] D. J. Singh. Physical Review B **48**, 3571 (1993).

[32] D. J. Singh and W. E. Pickett. Physical Review Letters **73**, 476 (1994).

[33] D. Hamann and L. Mattheiss. Physical Review B **38**, 5138 (1988).

[34] J. Clem. Superconductor Science and Technology **11**, 909 (1998).

[35] C. Tsuei and J. Kirtley. Reviews of Modern Physics **72**, 969 (2000).

[36] F. Giustino, M. L. Cohen, and S. G. Louie. Nature **452**, 975 (2008).

[37] G. Savini, A. C. Ferrari, and F. Giustino. Physical Review Letters **105**, 037002 (2010).

[38] Y. Kamihara, T. Watanabe, M. Hirano, and H. Hosono. JACS **130**, 3296 (2008).

[39] M. Rotter, M. Tegel, and D. Johrendt. Physical Review Letters **101**, 107006 (2008).

[40] I. Mazin and J. Schmalian. Physica C: Superconductivity (2009).

[41] T. Hanaguri, S. Niitaka, K. Kuroki, and H. Takagi. Science **328**, 474 (2010).

[42] I. I. Mazin. Nature **464**, 183 (2010).

[43] B. Radisavljevic, A. Radenovic, J. Brivio, V. Giacometti, and A. Kis. Nature Nanotechnology **6**, 147 (2011).

[44] J. Ye, Y. Zhang, R. Akashi, M. Bahramy, R. Arita, and Y. Iwasa. Science **338**, 1193 (2012).

[45] L. Boeri, O. Dolgov, and A. Golubov. Physical Review Letters **101**, 026403 (2008).

[46] K. Novoselov, D. Jiang, F. Schedin, T. Booth, V. Khotkevich, S. Morozov, and A. Geim. Proceedings of the National Academy of Sciences of the United States of America **102**, 10451 (2005).

[47] A. Yoffe. Advances in Physics **42**, 173 (1993).

[48] A. Yoffe. Annual Review of Materials Science **3**, 147 (1973).

[49] K. F. Mak, C. Lee, J. Hone, J. Shan, and T. F. Heinz. Physical Review Letters **105**, 136805 (2010).

[50] C. Lee, H. Yan, L. E. Brus, T. F. Heinz, J. Hone, and S. Ryu. ACS Nano **4**, 2695 (2010).

[51] A. Splendiani, L. Sun, Y. Zhang, T. Li, J. Kim, C.-Y. Chim, G. Galli, and F. Wang. Nano Letters **10**, 1271 (2010).

[52] M. Benameur, B. Radisavljevic, J. Heron, S. Sahoo, H. Berger, and A. Kis. Nanotechnology **22**, 125706 (2011).

[53] H. Li, G. Lu, Z. Yin, Q. He, H. Li, Q. Zhang, and H. Zhang. Small **8**, 682 (2012).

[54] Q. H. Wang, K. Kalantar-Zadeh, A. Kis, J. N. Coleman, and M. S. Strano. Nature Nanotechnology **7**, 699 (2012).

[55] J. N. Coleman, M. Lotya, A. ONeill, S. D. Bergin, P. J. King, U. Khan, K. Young, A. Gaucher, S. De, R. J. Smith, *et al.* Science **331**, 568 (2011).

[56] R. J. Smith, P. J. King, M. Lotya, C. Wirtz, U. Khan, S. De, A. O'Neill, G. S. Duesberg, J. C. Grunlan, G. Moriarty, *et al.* Advanced materials **23**, 3944 (2011).

[57] Y.-H. Lee, X.-Q. Zhang, W. Zhang, M.-T. Chang, C.-T. Lin, K.-D. Chang, Y.-C. Yu, J. T.-W. Wang, C.-S. Chang, L.-J. Li, *et al.* Advanced Materials **24**, 2320 (2012).

[58] Y. Zhan, Z. Liu, S. Najmaei, P. M. Ajayan, and J. Lou. Small **8**, 966 (2012).

[59] K.-K. Liu, W. Zhang, Y.-H. Lee, Y.-C. Lin, M.-T. Chang, C.-Y. Su, C.-S. Chang, H. Li, Y. Shi, H. Zhang, *et al.* Nano Letters **12**, 1538 (2012).

[60] A. Kumar and P. Ahluwalia. The European Physical Journal B-Condensed Matter and Complex Systems **85**, 1 (2012).

[61] E. S. Kadantsev and P. Hawrylak. Solid State Communications **152**, 909 (2012).

[62] Y. Zhang, T.-R. Chang, B. Zhou, Y.-T. Cui, H. Yan, Z. Liu, F. Schmitt, J. Lee, R. Moore, Y. Chen, *et al.* Nature Nanotechnologyanotechnology (2013).

[63] A. Kuc, N. Zibouche, and T. Heine. Physical Review B **83**, 245213 (2011).

[64] H. Ramakrishna Matte, A. Gomathi, A. K. Manna, D. J. Late, R. Datta, S. K. Pati, and C. Rao. Angewandte Chemie **122**, 4153 (2010).

[65] B. Hoefflinger. Chips 2020: a guide to the future of nanoelectronics. Springer (2012).

[66] F. Schwierz. Nature Nanotechnology **5**, 487 (2010).

[67] Y. Wu, Y.-m. Lin, A. A. Bol, K. A. Jenkins, F. Xia, D. B. Farmer, Y. Zhu, and P. Avouris. Nature **472**, 74 (2011).

[68] Y.-M. Lin, A. Valdes-Garcia, S.-J. Han, D. B. Farmer, I. Meric, Y. Sun, Y. Wu, C. Dimitrakopoulos, A. Grill, P. Avouris, and K. A. Jenkins. Science **332**, 1294 (2011).

[69] K. Taniguchi, A. Matsumoto, H. Shimotani, and H. Takagi. Applied Physics Letters **101**, 042603 (2012).

[70] K. Ueno, S. Nakamura, H. Shimotani, A. Ohtomo, N. Kimura, T. Nojima, H. Aoki, Y. Iwasa, and M. Kawasaki. Nature materials **7**, 855 (2008).

[71] K. Ueno, S. Nakamura, H. Shimotani, H. Yuan, N. Kimura, T. Nojima, H. Aoki, Y. Iwasa, and M. Kawasaki. Nature nanotechnology **6**, 408 (2011).

[72] A. T. Bollinger, G. Dubuis, J. Yoon, D. Pavuna, J. Misewich, and I. Božović. Nature **472**, 458 (2011).

[73] X. Leng, J. Garcia-Barriocanal, S. Bose, Y. Lee, and A. Goldman. Physical review letters **107**, 027001 (2011).

[74] H. Takahashi, K. Igawa, K. Arii, Y. Kamihara, M. Hirano, and H. Hosono. Nature **453**, 376 (2008).

[75] K. Ishida, Y. Nakai, and H. Hosono. J. Phys. Soc. Jpn. **78**, 062001 (2009).

[76] C. Chu and B. Lorenz. Physica C: Superconductivity **469**, 385 (2009).

[77] C.-H. Lee, A. Iyo, H. Eisaki, H. Kito, M. T. Fernandez-Diaz, T. Ito, K. Kihou, H. Matsuhata, M. Braden, and K. Yamada. J. Phys. Soc. Jpn. **77**, 083704 (2008).

[78] T. Nomura, S. W. Kim, Y. Kamihara, M. Hirano, P. V. Sushko, K. Kato, M. Takata, A. L. Shluger, and H. Hosono. Superconductor Science and Technology **21**, 125028 (2008).

[79] D. J. Singh and M.-H. Du. Phys. Rev. Lett. **100**, 237003 (2008).

[80] K. Nakamura, R. Arita, and M. Imada. J. Phys. Soc. Jpn. **77**, 093711 (2008).

[81] C. Liu, Y. Lee, A. D. Palczewski, J.-Q. Yan, T. Kondo, B. N. Harmon, R. W. McCallum, T. A. Lograsso, and A. Kaminski. Physical Review B **82**, 075135 (2010).

[82] A. Coldea, J. Fletcher, A. Carrington, J. Analytis, A. Bangura, J.-H. Chu, A. Erickson, I. Fisher, N. Hussey, and R. McDonald. Physical review letters **101**, 216402 (2008).

[83] F. Ma and Z.-Y. Lu. Phys. Rev. B **78**, 033111 (2008).

[84] S. Ishibashi, K. Terakura, and H. Hosono. Journal of the Physical Society of Japan **77**, 053709 (2008).

[85] Y. Qiu, M. Kofu, W. Bao, S.-H. Lee, Q. Huang, T. Yildirim, J. Copley, J. Lynn, T. Wu, G. Wu, *et al.* Physical Review B **78**, 052508 (2008).

[86] I. I. Mazin, D. J. Singh, M. D. Johannes, and M. H. Du. Phys. Rev. Lett. **101**, 057003 (2008).

[87] K. Kuroki, S. Onari, R. Arita, H. Usui, Y. Tanaka, H. Kontani, and H. Aoki. Physical Review Letters **101**, 087004 (2008).

[88] R. H. Liu, T. Wu, G. Wu, H. Chen, X. F. Wang, Y. L. Xie, J. J. Ying, Y. J. Yan, Q. J. Li, B. C. Shi, W. S. Chu, Z. Y. Wu, and X. H. Chen. Nature **459**, 64 (2009).

[89] M. L. Kulic and A. A. Haghighirad. EPL (Europhysics Letters) **87**, 17007 (2009).

[90] E. Schrödinger. Annalen der physik **385**, 437 (1926).

[91] W. Kohn. Reviews of Modern Physics **71**, 1253 (1999).

[92] M. Born and R. Oppenheimer. Annalen der Physik **389**, 457 (1927).

[93] D. R. Hartree. Mathematical Proceedings of the Cambridge Philosophical Society **24**, 89 (1928).

[94] F. Giustino. Materials Modelling Using Density Functional Theory: Properties and Predictions. Oxford University Press (2014).

[95] P. Hohenberg and W. Kohn. Phys. Rev. **136**, B864 (1964).

[96] W. Kohn and L. J. Sham. Phys. Rev. **140**, A1133 (1965).

[97] D. M. Ceperley and B. J. Alder. Phys. Rev. Lett. **45**, 566 (1980).

[98] J. P. Perdew and A. Zunger. Phys. Rev. B **23**, 5048 (1981).

[99] J. P. Perdew, K. Burke, and M. Ernzerhof. Phys. Rev. Lett. **77**, 3865 (1996).

[100] J. P. Perdew and Y. Wang. Phys. Rev. B **45**, 13244 (1992).

[101] C. G. Broyden. Mathematics of computation 577–593 (1965).

[102] M. C. Payne, M. P. Teter, D. C. Allan, T. A. Arias, and J. D. Joannopoulos. Rev. Mod. Phys. **64**, 1045 (1992).

[103] H. J. Monkhorst and J. D. Pack. Phys. Rev. B **13**, 5188 (1976).

[104] G. N. Lewis. Journal of the American Chemical Society **38**, 762 (1916).

[105] D. Vanderbilt. Phys. Rev. B **41**, 7892 (1990).

[106] P. E. Blöchl. Phys. Rev. B **50**, 17953 (1994).

[107] H. Hellmann. Zeitschrift für Physik **85**, 180 (1933).

[108] R. P. Feynman. Physical Review **56**, 340 (1939).

[109] J. D. Head and M. C. Zerner. Chemical Physics Letters **122**, 264 (1985).

[110] M. Born and T. Von Karman. Phys. Zeitschr **14**, 15 (1913).

[111] N. W. Ashcroft and D. Mermin. Saunders, Philadelphia (1976).

[112] S. Baroni, S. de Gironcoli, A. Dal Corso, and P. Giannozzi. Reviews of Modern Physics **73**, 515 (2001).

[113] R. Sternheimer. Physical Review **96**, 951 (1954).

[114] S. Baroni, P. Giannozzi, and A. Testa. Physical review letters **58**, 1861 (1987).

[115] W. Press, B. Flannery, S. Teukolsky, W. Vetterling, and B. Flannery. Numerical recipes, the art of scientific computing. Cambridge University Press Cambridge (1989).

[116] W. Kohn. Physical Review Letters **2**, 393 (1959).

[117] G. Grimvall. Physica Scripta **12**, 337 (1975).

[118] G. Grimvall. The electron-phonon interaction in metals. North-Holland Pub. Co.: sole distributors for the USA and Canada, Elsevier North-Holland (1981).

[119] G. D. Mahan. Many-particle physics. Springer (2000).

[120] G. L. Squires. Introduction to the theory of thermal neutron scattering. Cambridge university press (1978).

[121] E. Burkel, J. Peisl, and B. Dorner. EPL (Europhysics Letters) **3**, 957 (1987).

[122] E. Burkel. Reports on Progress in Physics (2000).

[123] W. Bardyszewski and L. Hedin. Physica Scripta **32**, 439 (1985).

[124] A. Migdal. Sov. Phys. JETP **7**, 996 (1958).

[125] F. Giustino, M. Cohen, and S. Louie. Physical Review B **76**, 165108 (2007).

[126] B. McDougall, T. Balasubramanian, and E. Jensen. Physical Review B **51**, 13891 (1995).

[127] P. B. Allen. Physical Review B **6**, 2577 (1972).

[128] P. B. Allen and R. Dynes. Physical Review B **12**, 905 (1975).

[129] F. Giustino, J. Yates, I. Souza, M. Cohen, and S. Louie. Physical review letters **98**, 47005 (2007).

[130] J. Noffsinger, F. Giustino, B. D. Malone, C.-H. Park, S. G. Louie, and M. L. Cohen. Computer Physics Communications **181**, 2140 (2010).

[131] A. A. Mostofi, J. R. Yates, Y.-S. Lee, I. Souza, D. Vanderbilt, and N. Marzari. Computer Physics Communications **178**, 685 (2008).

[132] N. Marzari, A. A. Mostofi, J. R. Yates, I. Souza, and D. Vanderbilt. Reviews of Modern Physics **84**, 1419 (2012).

[133] G. Wannier. Physical Review **52**, 191 (1937).

[134] N. Marzari and D. Vanderbilt. Physical review B **56**, 12847 (1997).

[135] L. Gor'kov. Sov. Phys.-JETP (Engl. Transl.);(United States) **7** (1958).

[136] P. B. Allen and B. Mitrović. Solid State Physics **37**, 1 (1983).

[137] A. A. Abrikosov, L. P. Gorkov, and I. E. Dzialoshinski. Quantum field theoretical methods in statistical physics, volume 4. Pergamon (1965).

[138] J. C. Slater. Physical Review **81**, 385 (1951).

[139] G. Eliashberg. Sov. Phys.-JETP (Engl. Transl.);(United States) **11** (1960).

[140] Y. Nambu. Physical Review **117**, 648 (1960).

[141] J. Bardeen and M. Stephen. Physical Review **136**, A1485 (1964).

[142] J. Carbotte. Reviews of Modern Physics **62**, 1027 (1990).

[143] M. Holcomb. Physical Review B **54**, 6648 (1996).

[144] H. Vidberg and J. Serene. Journal of Low Temperature Physics **29**, 179 (1977).

[145] C. Leavens and D. Ritchie. Solid state communications **53**, 137 (1985).

[146] F. Marsiglio, M. Schossmann, and J. Carbotte. Physical Review B **37**, 4965 (1988).

[147] E. R. Margine and F. Giustino. Physical Review B **87**, 024505 (2013).

[148] W. McMillan and J. Rowell. Treatise on Superconductivity. Marcel Dekker, New York (1969).

[149] K. S. Novoselov, A. K. Geim, S. Morozov, D. Jiang, Y. Zhang, S. Dubonos, I. Grigorieva, and A. Firsov. science **306**, 666 (2004).

[150] C. Berger, Z. Song, T. Li, X. Li, A. Y. Ogbazghi, R. Feng, Z. Dai, A. N. Marchenkov, E. H. Conrad, P. N. First, *et al.* The Journal of Physical Chemistry B **108**, 19912 (2004).

[151] K. Novoselov, A. K. Geim, S. Morozov, D. Jiang, M. K. I. Grigorieva, S. Dubonos, and A. Firsov. nature **438**, 197 (2005).

[152] Y. Zhang, Y.-W. Tan, H. L. Stormer, and P. Kim. Nature **438**, 201 (2005).

[153] X. Du, I. Skachko, F. Duerr, A. Luican, and E. Y. Andrei. Nature **462**, 192 (2009).

[154] K. I. Bolotin, K. Sikes, Z. Jiang, M. Klima, G. Fudenberg, J. Hone, P. Kim, and H. Stormer. Solid State Communications **146**, 351 (2008).

[155] Z. Chen, Y.-M. Lin, M. J. Rooks, and P. Avouris. Physica E: Low-dimensional Systems and Nanostructures **40**, 228 (2007).

[156] A. Cresti, A. Lopez-Bezanilla, P. Ordejo n, and S. Roche. ACS nano **5**, 9271 (2011).

[157] J. B. Oostinga, H. B. Heersche, X. Liu, A. F. Morpurgo, and L. M. Vandersypen. Nature materials **7**, 151 (2007).

[158] G. Giovannetti, P. A. Khomyakov, G. Brocks, P. J. Kelly, and J. van den Brink. Physical Review B **76**, 073103 (2007).

[159] L. Ci, L. Song, C. Jin, D. Jariwala, D. Wu, Y. Li, A. Srivastava, Z. Wang, K. Storr, L. Balicas, *et al.* Nature materials **9**, 430 (2010).

[160] L. Panchakarla, K. Subrahmanyam, S. Saha, A. Govindaraj, H. Krishnamurthy, U. Waghmare, and C. Rao. Advanced Materials **21**, 4726 (2009).

[161] M. Y. Han, B. Özyilmaz, Y. Zhang, and P. Kim. Physical review letters **98**, 206805 (2007).

[162] D. Kim, D. Sun, W. Lu, Z. Cheng, Y. Zhu, D. Le, T. S. Rahman, and L. Bartels. Langmuir **27**, 11650 (2011).

[163] M. Chhowalla, H. S. Shin, G. Eda, L.-J. Li, K. P. Loh, and H. Zhang. Nature chemistry **5**, 263 (2013).

[164] Y. Yoon, K. Ganapathi, and S. Salahuddin. Nano letters **11**, 3768 (2011).

[165] F. K. Perkins, A. L. Friedman, E. Cobas, P. Campbell, G. Jernigan, and B. T. Jonker. Nano letters **13**, 668 (2013).

[166] M. Fontana, T. Deppe, A. K. Boyd, M. Rinzan, A. Y. Liu, M. Paranjape, and P. Barbara. Scientific reports **3** (2013).

[167] B. Chakraborty, A. Bera, D. Muthu, S. Bhowmick, U. Waghmare, and A. Sood. Physical Review B **85**, 161403 (2012).

[168] L. Gomez, I. Aberg, and J. Hoyt. Electron Device Letters, IEEE **28**, 285 (2007).

[169] Y. Zhang, J. Ye, Y. Matsuhashi, and Y. Iwasa. Nano letters **12**, 1136 (2012).

[170] A. Ayari, E. Cobas, O. Ogundadegbe, and M. S. Fuhrer. Journal of applied physics **101**, 014507 (2007).

[171] W. O. Winer. Wear **10**, 422 (1967).

[172] W. Ho, J. C. Yu, J. Lin, J. Yu, and P. Li. Langmuir **20**, 5865 (2004).

[173] D. S. Thakur and B. Delmon. Journal of Catalysis **91**, 308 (1985).

[174] E. Gourmelon, O. Lignier, H. Hadouda, G. Couturier, J. Bernede, J. Tedd, J. Pouzet, and J. Salardenne. Solar energy materials and solar cells **46**, 115 (1997).

[175] R. S. Title and M. Shafer. Physical Review B **8**, 615 (1973).

[176] P. Giannozzi, S. Baroni, N. Bonini, M. Calandra, R. Car, C. Cavazzoni, D. Ceresoli, G. L. Chiarotti, M. Cococcioni, I. Dabo, A. D. Corso, S. de Gironcoli, S. Fabris, G. Fratesi, R. Gebauer, U. Gerstmann, C. Gougoussis, A. Kokalj, M. Lazzeri, L. Martin-Samos, N. Marzari, F. Mauri, R. Mazzarello, S. Paolini, A. Pasquarello, L. Paulatto, C. Sbraccia, S. Scandolo, G. Sclauzero, A. P. Seitsonen, A. Smogunov, P. Umari, and R. M. Wentzcovitch. Journal of Physics: Condensed Matter **21**, 395502 (2009).

[177] M. Fuchs and M. Scheffler. Computer Physics Communications **119**, 67 (1999).

[178] N. Troullier and J. L. Martins. Physical Review B **43**, 1993 (1991).

[179] S. G. Louie, S. Froyen, and M. L. Cohen. Physical Review B **26**, 1738 (1982).

[180] N. Wakabayashi, H. Smith, and R. Nicklow. Physical Review B **12**, 659 (1975).

[181] A. Molina-Sanchez and L. Wirtz. Physical Review B **84**, 155413 (2011).

[182] G. Kresse, J. Furthmüller, and J. Hafner. EPL (Europhysics Letters) **32**, 729 (1995).

[183] G. Kern, G. Kresse, and J. Hafner. Physical Review B **59**, 8551 (1999).

[184] C. Ataca, M. Topsakal, E. Akturk, and S. Ciraci. The Journal of Physical Chemistry C **115**, 16354 (2011).

[185] A. H. Reshak and S. Auluck. Physical Review B **68**, 125101 (2003).

[186] K. Kobayashi and J. Yamauchi. Physical Review B **51**, 17085 (1995).

[187] K. K. Kam and B. A. Parkinson. The Journal of Physical Chemistry **86**, 463 (1982).

[188] R. M. Martin. Electronic structure: basic theory and practical methods. Cambridge university press (2004).

[189] T. Wieting and J. Verble. Physical Review B **3**, 4286 (1971).

[190] J. Chen and C. Wang. Solid State Communications **14**, 857 (1974).

[191] J. D. Fuhr, A. Saúl, and J. O. Sofo. Physical review letters **92**, 026802 (2004).

[192] Y. Li, Z. Zhou, S. Zhang, and Z. Chen. Journal of the American Chemical Society **130**, 16739 (2008).

[193] Y. Cai, J. Lan, G. Zhang, and Y.-W. Zhang. Physical Review B **89**, 035438 (2014).

[194] L. He and D. Vanderbilt. Physical Review Letters **86**, 5341 (2001).

[195] F. Zahid, L. Liu, Y. Zhu, J. Wang, and H. Guo. AIP Advances **3**, 052111 (2013).

[196] E. McCann, K. Kechedzhi, V. I. Falko, H. Suzuura, T. Ando, and B. Altshuler. Physical review letters **97**, 146805 (2006).

[197] R. Saito, G. Dresselhaus, and M. Dresselhaus. Physical Review B **61**, 2981 (2000).

[198] R. Somoano, V. Hadek, A. Rembaum, S. Samson, and J. Woollam. The Journal of Chemical Physics **62**, 1068 (1975).

[199] J. A. Woollam and R. B. Somoano. Physical Review B **13**, 3843 (1976).

[200] H. H. Gürel, V. O. Özçelik, and S. Ciraci. Journal of Physics: Condensed Matter **25**, 305007 (2013).

[201] E. Margine and F. Giustino. Physical Review B **90**, 014518 (2014).

[202] Y. Ge and A. Y. Liu. Physical Review B **87**, 241408 (2013).

[203] Y. Ge, W. Wan, W. Feng, D. Xiao, and Y. Yao. Physical Review B **90**, 035414 (2014).

[204] E. L. Wolf. Principles of electron tunneling spectroscopy, volume 152. Oxford University Press (2012).

[205] M. Rösner, S. Haas, and T. Wehling. arXiv preprint arXiv:1404.4295 (2014).

[206] R. Zhi-An, L. Wei, Y. Jie, Y. Wei, S. Xiao-Li, Zheng-Cai, C. Guang-Can, D. Xiao-Li, S. Li-Ling, Z. Fang, and Z. Zhong-Xian. Chin. Phys. Lett. **25**, 2215 (2008).

[207] M. Rotter, M. Tegel, D. Johrendt, I. Schellenberg, W. Hermes, and R. Pöttgen. Phys. Rev. B **78**, 020503 (2008).

[208] X. Wang, Q. Liu, Y. Lv, W. Gao, L. Yang, R. Yu, F. Li, and C. Jin. Solid State Communications **148**, 538 (2008).

[209] F.-C. Hsu, J.-Y. Luo, K.-W. Yeh, T.-K. Chen, T.-W. Huang, P. M. Wu, Y.-C. Lee, Y.-L. Huang, Y.-Y. Chu, D.-C. Yan, and M.-K. Wu. Proceedings of the National Academy of Sciences **105**, 14262 (2008).

[210] M. Lumsden and A. Christianson. Journal of Physics: Condensed Matter **22**, 203203 (2010).

[211] J. Paglione and R. Greene. Nature Physics **6**, 645 (2010).

[212] C. de la Cruz, Q. Huang, J. W. Lynn, J. Li, W. Ratcliff, II, J. L. Zarestky, H. A. Mook, G. F. Chen, J. L. Luo, N. L. Wang, and P. Dai. Nature **453**, 899 (2008).

[213] I. I. Mazin, M. D. Johannes, L. Boeri, K. Koepernik, and D. J. Singh. Phys. Rev. B **78**, 085104 (2008).

[214] Z. P. Yin, S. Lebègue, M. J. Han, B. P. Neal, S. Y. Savrasov, and W. E. Pickett. Phys. Rev. Lett. **101**, 047001 (2008).

[215] T. Yildirim. Phys. Rev. Lett. **101**, 057010 (2008).

[216] I. Mazin and M. Johannes. Nature Physics **5**, 141 (2008).

[217] S. Lebegue, Z. P. Yin, and W. E. Pickett. New Journal of Physics **11**, 025004 (2009).

[218] G. Giovannetti, S. Kumar, and J. van den Brink. Physica B: Condensed Matter **403**, 3653 (2008).

[219] H. Luetkens, H. H. Klauss, M. Kraken, F. J. Litterst, T. Dellmann, R. Klingeler, C. Hess, R. Khasanov, A. Amato, C. Baines, M. Kosmala, O. J. Schumann, M. Braden, J. Hamann-Borrero, N. Leps, A. Kondrat, G. Behr, J. Werner, and B. Buechner. Nature Materials **8**, 305 (2009).

[220] H. I. Fisher. Ph.D. thesis, University of Oxford (2010).

[221] H.-H. Klauss, H. Luetkens, R. Klingeler, C. Hess, F. J. Litterst, M. Kraken, M. M. Korshunov, I. Eremin, S.-L. Drechsler, R. Khasanov, A. Amato, J. Hamann-Borrero, N. Leps, A. Kondrat, G. Behr, J. Werner, and B. Büchner. Phys. Rev. Lett. **101**, 077005 (2008).

[222] T. Yildirim. Phys. Rev. Lett. **102**, 037003 (2009).

[223] F. Yndurain and J. M. Soler. Phys. Rev. B **79**, 134506 (2009).

[224] G. Giovannetti, C. Ortix, M. Marsman, M. Capone, J. van den Brink, and J. Lorenzana. Nature communications **2**, 398 (2011).

[225] V. García-Suárez, C. Newman, C. Lambert, J. Pruneda, and J. Ferrer. Journal of Physics: Condensed Matter **16**, 5453 (2004).

[226] A. S. Sefat, M. A. McGuire, B. C. Sales, R. Jin, J. Y. Howe, and D. Mandrus. Physical Review B **77**, 174503 (2008).

[227] J. Noffsinger, F. Giustino, S. G. Louie, and M. L. Cohen. Physical review letters **102**, 147003 (2009).

[228] C. de la Cruz, W. Z. Hu, S. Li, Q. Huang, J. W. Lynn, M. A. Green, G. F. Chen, N. L. Wang, H. A. Mook, Q. Si, and P. Dai. Phys. Rev. Lett. **104**, 017204 (2010).

[229] S. Sharma, S. Shallcross, J. Dewhurst, A. Sanna, C. Bersier, S. Massidda, and E. Gross. Physical Review B **80**, 184502 (2009).

[230] M. Johannes, I. Mazin, and D. Parker. Physical Review B **82**, 024527 (2010).

[231] H. Okada, K. Igawa, H. Takahashi, Y. Kamihara, M. Hirano, H. Hosono, K. Matsubayashi, and Y. Uwatoko. Journal of the Physical Society of Japan **77** (2008).

[232] Y. Yang and X. Hu. Journal of Applied Physics **106**, 073910 (2009).

[233] A. D. Christianson, M. D. Lumsden, O. Delaire, M. B. Stone, D. L. Abernathy, M. A. McGuire, A. Sefat, R. Jin, B. C. Sales, D. Mandrus, *et al.* Physical review letters **101**, 157004 (2008).

[234] G. Onida, L. Reining, and A. Rubio. Reviews of Modern Physics **74**, 601 (2002).

[235] G. Kotliar, S. Y. Savrasov, K. Haule, V. S. Oudovenko, O. Parcollet, and C. Marianetti. Reviews of Modern Physics **78**, 865 (2006).

Acknowledgements

First, and foremost I would like to thank my supervisor Feliciano Guistino for his support, guidance, and substantial patience over the last four years.

I also wish to thank everyone in the MML who has made the last few years so enjoyable. In particular those who I have shared an office with over the years - Chris, Keian, Tim, Henry and Marina. I have really enjoyed the stimulating and fun working environment. I would also like to thank Roxana for all the help with the EPW and Eliashberg codes and the many useful skype conversations over the course of this project.

My time at Oxford has been so enjoyable in no small part due to the friends I have made. Bex, Callum, and Tim deserve a special mention, and have been both fantastic housemates and great friends.

Kate - I want to thank you so much for all the great times we have had over the years. In particular, thanks for putting up with me in the final stages of writing this thesis.

Last but not least I would like to thank my family. I'm sure you will have even more fun reading this one than my part II thesis!